ABSTRACT

Title of dissertation: ON THE FLUID DYNAMICS OF VIRTUAL IMPACTION AND THE DESIGN OF A SLIT AEROSOL SAMPLER

Marwan L. Charrouf, Doctor of Philosophy, 2006

Dissertation directed by: Professor Richard V. Calabrese
Department of Chemical & Biomolecular Engineering

It has been long established that Reynolds number effects can lead to flow instabilities and/or transition from laminar to turbulent flow regimes. The nature of free shear jets is well understood and heavily covered in the fluid mechanics literature. On the other hand, the study of confined nozzles presents some challenges and is still a developing area of research. In this work, we focus on quasi-impinging jets, such as the ones feeding into a virtual impactor. Virtual impactors are popular, inexpensive aerosol collection devices capable of separating airborne solid particles. Recently they found increased application in areas that require concentration of dilute aerosols, such as biological-laden flows. In essence, this research is motivated by the need to fundamentally understand the fluid-particle interaction mechanisms entailed during virtual impaction. To this end, we rely on theoretical insight gained by numerical analysis of the classical equations within a one-way coupled Lagrangian framework.

In the first part of this investigation we perform a direct transient simulation of the two-dimensional incompressible Navier-Stokes equations for air as the carrier phase. The momentum and continuity equations are solved by FLUENT. The solutions of three separate computations with jet Reynolds numbers equal to 350, 2100,

and 3500 are analyzed. The 2-D time-mean results established the nature of the jet potential core and clarifications about the role of the Reynolds number were proposed. Transient analysis deciphered the characteristics of the *mirrored Kelvin-Helmholtz* instability, along with particle-eddy interaction mechanisms.

In the second part we perform a large eddy simulation (LES) on a domain of a real-life sampler. The Lagrangian dynamic residual stress model is implemented and validated for two canonical turbulent flows. The newly contrived code is then applied to the study of a prototype device. A three-dimensional growth mechanism is proposed for the jet mixing layers. The Lagrangian dynamic model LES exhibited significant regions of high subgrid turbulent viscosity, compared to the dynamic Lilly-model simulation, and we were able to identify the origin, and learn the dynamics of five key coherent structures dominant during transition. Comparison with preliminary experimental data for the aerosol separation efficiency showed fairly good agreement.

ON THE FLUID DYNAMICS OF VIRTUAL IMPACTION AND THE DESIGN OF A SLIT AEROSOL SAMPLER

by

Marwan L. Charrouf

Dissertation submitted to the Faculty of the Graduate School of the
University of Maryland, College Park in partial fulfillment
of the requirements for the degree of
Doctor of Philosophy
2006

Advisory Committee:

Professor Richard V. Calabrese, Chair
Professor Raymond A. Adomaitis
Professor Mikhail A. Anisimov
Professor Peter S. Bernard
Professor Panagiotis Dimitrakopoulos
Dr. M. B. (Arun) Ranade

ACKNOWLEDGMENTS

Many years, many sleepless nights, forget the tears, it is time to rejoice in the lights. I can not but feel humbled by the influences and assistances of several benevolent people. My advisor and mentor Professor Calabrese for his steady support and patience. It is absolutely true that much of this work would not have been possible without the strong and solid foundation I found in the conducive environment of his research group. My co-advisor Dr. Ranade was instrumental in introducing me to the science of Virtual Impactors. I am grateful to my colleague Karl Kevala for his guidance and willingness to share his fluid mechanics experience with me. I wish to thank our visiting Professor from France, Dr. Simoens for the many conversations we had about turbulence: *Merci beaucoup!*

Much appreciation is due to the members of my dissertation committee; thank you for taking the time to critique my work, and for your service. One resonating feeling of awe will forever accompany the memory of my stay here. I am indebted to the teachings of three magnificent instructors of Mechanical Engineering: Professor Wallace, Professor Bernard, and Professor Piomelli.

My family has always been a source of inspiration and perseverance. I am indefinitely beholden to their encouragement and trust.

Contents

List of Tables

List of Figures

Notation

A	square cylinder spanwise length, m
b	jet half-breadth, m
C_c	slip correction factor
C_s	Smagorinski model coefficient
C_D	drag coefficient
C_L	lift coefficient
D	cylinder diameter, m
D_h	hydraulic diameter of virtual impactor nozzle, m
d_m	geometric mean particle diameter, m
d_p	particle diameter, m
d_s	square cylinder short-edge length, m
g_i	component of gravitational acceleration in the i^{th} direction, m/s^2
$G(\mathbf{x}, \mathbf{y})$	filter function
L_m	length of minor flow duct, m
m_f	mass of fluid displaced by particle, kg
m_p	mass of particle, kg
N_c	number of grid cell neighbors
N_p	total number of particles
N_t	number of time steps used for averaging
P	pressure, Pa
$\overline{P}$	resolved pressure, Pa
Q_m	minor volumetric flow rate, $liter/min$
Q_T	total volumetric flow rate, $liter/min$

R_s	flow separation ratio
r_p	particle radius, m
S	gap between jet and probe, m
$\overline{S}_{ij}$	resolved rate of strain tensor, $1/s$
St	particle Stokes number
$\sqrt{St}_{50}$	dimensionless particle diameter at 50% collection efficiency
St_h	Strouhal number
T	length of throat leading to jet, m
T_s	wake shedding period, s
T^+	dimensionless wall-time unit
T^*	dimensionless time unit
$\mathbf{U}$	fluid velocity vector, m/s
$\overline{\mathbf{U}}$	resolved fluid velocity vector, m/s
U_i	instantaneous fluid velocity in the i^{th} direction, m/s
U_j	average jet streamwise velocity, m/s
U_o	mean jet centerline velocity, m/s
U_{oo}	centerline jet velocity at nozzle exit plane, m/s
U_m	entrance velocity to minor flow duct, m/s
U_{in}	inflow velocity, m/s
U_∞	free stream velocity, m/s
$< U_i >$	time averaged velocity component, m/s
U_i^{rms}	root mean square velocity component, m/s
U_c	outflow convective velocity, m/s
U_τ	friction velocity, m/s
$\mathbf{u}'$	residual fluid velocity vector, m/s
$\mathbf{V}$	particle velocity vector, m/s
V	cell volume, m^3

W	width of virtual impaction jet, m
W_c	width of collection probe, m
$\mathbf{x}_p$	particle position vector
x_i	component of the position vector in the i^{th} direction
$\overline{Y}_T$	dispersion function of all particles, m
$\overline{Y}_c$	dispersion function of minor flow particles, m
ρ	density of fluid, kg/m^3
ρ_p	density of particle, kg/m^3
μ	molecular viscosity of air, $kg/m.s$
ν	kinematic viscosity of air, m^2/s
ν_T	eddy viscosity, m^2/s
τ_f	characteristic flow time scale, s
τ_p	particle relaxation time, s
τ_{vi}	average time for virtual impaction, s
τ_λ	jet instability microscale time, s
τ_{ij}	residual stress tensor, m^2/s^2
τ_w	wall shear stress $\equiv \mu dU/dy\|_w, kg/m.s^2$
δ	jet shear layer thickness, m
δ_h	channel half width, m
δ_{ij}	Kronecker delta
Δ	filter size, m
$\widehat{\Delta}$	test filter size, m
Δt	simulation time step, s
Re	flow Reynolds number
Re_p	particle Reynolds number
Re_δ	Reynolds number based on δ and U_{oo}
Re_τ	Reynolds number based on U_τ and δ_h

σ	geometric standard deviation of aerosol size distribution
σ_a	standard deviation of random variable a
σ^*_{ab}	correlation coefficient between random variables a & b
ω	frequency, Hz
Ω	vorticity vector, $1/s$
K	turbulent kinetic energy, m^2/s^2
Q	second invariant of velocity gradient tensor, $1/s$
$\overline{\Upsilon}_{ij}$	resolved rate of rotation tensor, $1/s$

Chapter 1

Introduction

The systematic analysis of the fluid mechanics of engineering flow systems is unequivocally critical for the successful design and operation of *fluidic* devices. This research is mainly aimed at understanding the hydrodynamics of "virtual impactors" which are widely used for aerosol collection and sampling. The problem lends itself to the special class of multiphase flows where the particulate solid phase is transported or suspended in the carrier gas phase. Naturally, the mechanisms and ideas initiated and applied in this category of flows are closely tied with other similar fluid-particle flows which range from large-scale environmental phenomena to bench-scale chemical processing.

The collection and characterization of chemical or biological aerosols is essential in areas such as toxicology, pollutant monitoring, and homeland security. The particle capturing process is almost exclusively performed by virtual impaction at least in one stage of the sampling experiment. Therefore, virtual impaction devices have witnessed a tremendous evolution in terms of operability and complexity, from the simple geometries constructed in the late seventies [1] to the intricate and bundled incarnations present today [2]. Fortunately, the underlying fluid mechanical principles governing all these systems are still the same, and this work introduces new insight

into the fluid and particle behavior in a prototypical design.

The majority of studies that analyze the flow dynamics within virtual impactors have been experimental where the main concern was to gather collection efficiency information as a function of particle diameter. Such a classical approach ignores or fails to address the fundamental interaction mechanisms that lead to the observed macroscopic properties. To the extent where computer simulations have been used, those investigations were limited in scope and accuracy. The purpose of the research project presented herein is to conduct realistic time- and space-accurate calculations to resolve the unsteady and energy containing fluid motions that inherently influence the fate of the transported particles. In particular, the employment of direct and large eddy simulation techniques allows us to thoroughly interrogate the mechanisms affecting particle concentration and dispersion. Furthermore, Lagrangian computations of particle trajectories and dispersion functions have been made and interpreted to determine the role of the dominant coherent structures.

One aspect of this study has also dealt with the evaluation and performance of a prototype round-slit virtual impactor. Preliminary particle collection experiments were performed in a wind tunnel for aerosol distributions ranging between 0.7 to 3.5 μm in aerodynamic particle diameter. The samples were analyzed with a digital particle-sizer spectrometer and compared to the simulation's predictions. The efficacy of the prototype is thus demonstrated and a new scaling hypothesis is introduced to properly quantify the real particulate penetration.

1.1 Literature Review

1.1.1 Virtual Impactors

The vitality of virtual impactors as effective means for sampling aerosols had been recognized for quite some time. For this reason, many experimental and theoret-

ical studies have been dedicated to evaluating and optimizing their performance. The basic flow mechanism comprises the segregation of the moving aerosol from a nozzle into a relatively stagnant large-particle chamber (minor flow), and a high speed small-particle cross stream (major flow). As depicted in figure 1.2, the converging inlet creates a passage for the particle-laden air to a throat section which forms the acceleration nozzle. The receiving end of the jet or minor flow constitutes a collection probe which is slightly larger in width than the accelerating nozzle. Larger particles, due to their inertia, deflect from the arched fluid streamlines and penetrate into the collection chamber, while smaller particles follow the majority of the fluid as it is forced to exit into the peripheral chambers or major flow. Typically, only a small fraction (10 to 20%) of the inlet flow becomes the minor flow.

In reality, the aerosol characterization process begins when the particles in the minor flow are gathered on a filter, in a liquid solution, or are passed through a cyclone for further separation. Another possibility is to cascade a series of virtual impactors to achieve even higher concentration factors [3, 4]. This methodology became a sound replacement for solid-surface impactors because it eliminates particle bounce and breakup, and allows for better control over the suspended aerosol.

The performance of a virtual impactor is assessed by a particle collection efficiency and wall loss curve as a function of particle size. The efficiency is defined as the fraction of particles with a given diameter that accumulate in the minor flow. For an ideal separator, the efficiency versus diameter is a sharp step function. It is established, however, that due to the inevitable contamination of the collected aerosol with the relatively smaller particles, the curve takes on an "*S*-shape" [5]. Figure 1.1, for example, reveals the 50% cutpoint diameter which indicates that half the particles whose size is equal to the cutpoint are collected, while the other half is forsaken to the major flow. Wall losses are generally undesirable in virtual impactors, and are mostly observed on the inner surfaces of the collection probe.

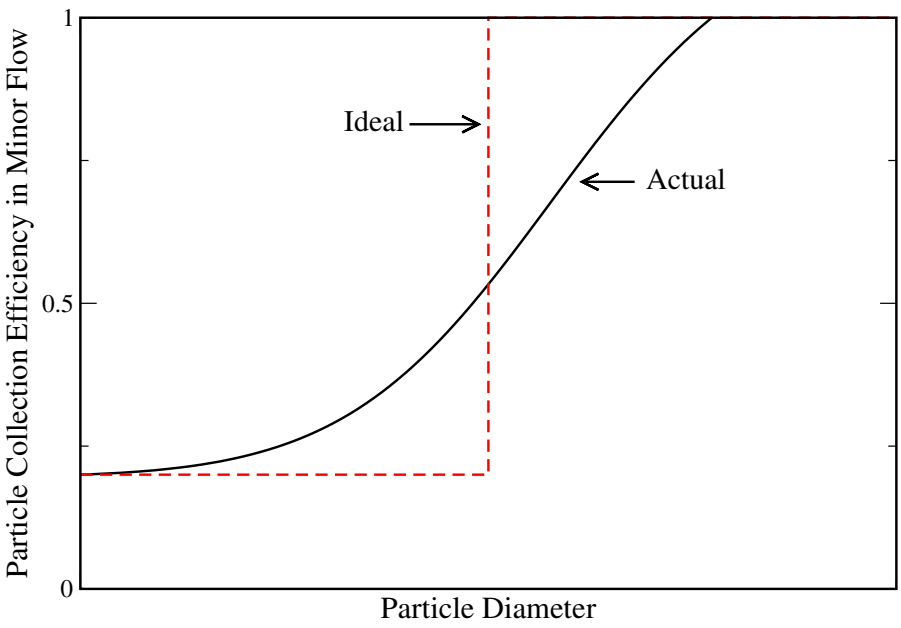

Figure 1.1: Ideal vs. actual efficiency for a virtual impactor

Experimental parametric studies that dealt with the impact of geometrical and flow configurations played a major role in steering the directions towards more efficient virtual impactor designs. Before we review some of those contributions, it is helpful to define the dimensionless groups pertaining to the problem. The Reynolds number is defined as:

$$Re = \frac{U_j D_h}{\nu}. \tag{1.1}$$

When rectangular slot nozzles are considered in a two-dimensional sense, then $D_h \equiv W$. The Stokes number quantifies the ratio of the particle relaxation time to a characteristic time scale in the flow. Hence,

$$St = \frac{\tau_p}{\tau_f}, \tag{1.2}$$

is a measure of how responsive the particle is to changes in the fluid's velocity field.

As mentioned earlier, the flow separation ratio, $R_s = Q_m/Q_T$, is also a factor that determines the low-end asymptotic behavior of the collection efficiency function. In the work of Chen *et al.* [6] on axis-symmetric jet nozzles, the authors found that effects of the Reynolds number are manifested as a shift in the efficiency curve towards lower cutpoints. This is naturally an outcome of the increased jet velocity causing an increased particle stopping distance. An interesting finding, nonetheless, was the collapse of all collection efficiency data onto a single chart when plotted against $\sqrt{St}$. Conclusions were made that for geometrically and dynamically similar virtual impactors, prediction of the 50% $\sqrt{St}$ is possible given an Re value in the 1000 to 8000 range. The same result was later confirmed by Ding and Koutrakis [7] for a rectangular slit nozzle, where the $\sqrt{St}_{50}$ remained in a narrow range of 0.68-0.71. The effect of the minor-to-total flow ratio, on the other hand, has severe consequences on the cutpoint as well as on the wall losses. As R_s is increased $\sqrt{St}_{50}$ is decreased. This can be explained by the fact that higher ratios allow more fine particles to pass through to the collection probe. Moreover, since the efficiency curve is asymptotic to R_s at the low end, its slope will accordingly be affected. The interpretation of wall loss behavior, however, is not as palpable. For instance, Ding and Koutrakis [7] distinguish between a "fine mode" ($d_p < 2.5\mu m$) and a "coarse mode" ($d_p > 2.5\mu m$) behavior. For particles in the fine mode, losses were low when Re remained below 5000, but grew considerably for higher Reynolds numbers. The increase in particle loss at high Re values was attributed to "flow instability" and "turbulence". The situation becomes even more difficult to comprehend for coarse particles. In this mode, the same study revealed that low Re values ($\sim$ 1500) yielded extremely high losses ($\sim$ 70%) which diminish drastically as the Reynolds number is pushed beyond 10,000. The influence of nozzle dimensions (W, W_c, S) was reported in a number of studies [6, 7, 10]. The consensus is that a ratio $W_c/W \sim 1.5$ is ideal for improved collection and minimum lossses, whereas, the void gap ratio, S/W, when tested with

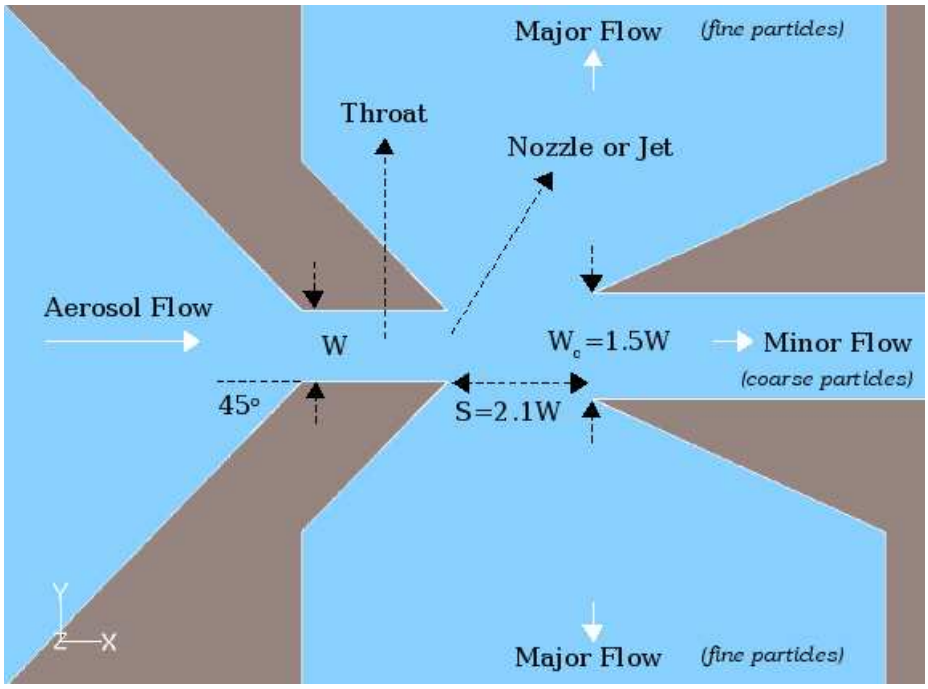

Figure 1.2: Schematic of virtual impactor nozzle. $W = 0.7\ mm$

values between 0.5 and 1.5 gave very negligible differences. Finally, Kim *et al.* [11] assessed the performace of flat or square-shaped nozzles versus cut-out protrusions, such as the one depicted in figure 1.2, and showed that the latter design is more beneficial in terms of higher collection and lower losses.

Parallel to the experimental studies, a significant body of work focused on theoretical aspects. Marple and Chien [5] obtained solutions of the Navier-Stokes equations in terms of vorticity and stream function using a finite difference method. Solid particles were then traced by solving the particle equation of motion governed by Stokes drag. The authors analyzed the influence of flow and geometrical considerations on the particle trajectory, collection, and loss. The numerical grid, however, was too coarse by today's standards to deliver accurate predictions. The approach was later revised in a subsequent paper by Rader and Marple [8] where they applied the technique to study solid surface impactors. The refinement focused on two main areas, the discretization gird, and the use of a non-linear drag coefficient. In a more recent

study, Asgharian and Godo [9] employed a commercial finite-element fluid dynamics code to obtain the flow velocity in a two-dimensional "improved" virtual impactor. An improved virtual impactor is one with a clean air core in the center of the inlet to the impaction zone. The authors solved for the incompressible steady-state flow field at a Reynolds number of 4000 using the standard $k - \epsilon$ turbulence model. The computational mesh consisted of approximately 14,000 nodes. When compared to experimental data, their calculations predicted a much steeper slope for the efficiency curve, and failed to match the asymptotic behavior for small particles. Hari [12] utilized a computational fluid dynamics package to optimize the operation of a virtual impactor in the laminar regime. Only one-half of the real geometry was constructed in two-dimensional space, with symmetry boundary conditions along the centerline of the computational domain. Charrouf [13] simulated the turbulent flow inside a three-dimensional device for which basic experimental data exists. The methodology relied on modeling the steady-state Reynolds average Navier-Stokes equations for incompressible and compressible flow fields. The particle tracking results compared well with experiment for the collection efficiency but not for wall losses.

One of the least covered topics in virtual impactors is the nature of the flow instability and turbulence. The roles that such important physical phenomena play in transporting or, for that matter, inhibiting the accumulation of particles is not well understood. It is safe to say that a detailed presentation of the fluid mechanical structures present during virtual impaction is not currently in existence, nevertheless, some visualization experiments have confirmed the appearance of such structures. As early as the 1980's, Forney *et al.* [10], while trying to understand the effect of the Reynolds number of the flow on the collection properties of their virtual impactor, observed "jet-core instabilities" through the use of dye in a water experiment. The authors spoke of "total breakdown of the fluid flow field", and of "intermittent fluid loss to the void". The study conceded that an acceptable range of operation exists

only between $700 < \mathrm{Re} < 1600$. Subsequently, Han and Moss [14] visualized the streamlines also in a water model, but with a clean-core inflow. They described the appearance of a counter-rotating vortex pair at $\mathrm{Re} \sim 3000$. In addition, they observed a breakdown of the dye in the major flow for $\mathrm{Re} > 4000$. Gotoh and Masuda [15] performed laser-sheet visualizations in a rectangular jet virtual impactor at $\mathrm{Re} = 2000$. They focused on eliminating the reversed flow from the collection nozzle, and intentionally avoided higher Reynolds number values so as not to "disturb the flow structure" which would then "mask" the effect of their proposed new nozzle.

1.1.2 Hydrodynamic Stability of Jets

The study of the stability characteristics of "free boundary layers", such as those present in laminar and turbulent jets, has been an active area of research for many fluid dynamicists and theoreticians alike. From the early 1960's, Sato and Sakao [16] demonstrated the occurrence of periodic velocity fluctuations in their hot-wire anemometer experiments with a two-dimensional laminar jet for $10 < \mathrm{Re} < 50$. Such fluctuations "die out" as they travel downstream, however, for higher Reynolds numbers, they observed that the periodic fluctuations developed into irregular, turbulent signals. Michalke and Freymuth [17] discussed the idea of a "separated flow" downstream of a nozzle issuing into a fluid at rest. Further downstream the jet boundary layer becomes unstable and local concentrations of vorticity become conspicuous. One interesting avenue of inquiry was the ability to artificially excite the naturally occurring unstable disturbances in the free boundary layer by sound from a loudspeaker (see also [18]). A continuation of such work, was carried out by Browand [19] to investigate the non-linear mechanisms associated with transition to turbulence. The main conclusion reached emphasized the growth of secondary instabilities in the separated shear layer, as well as random spanwise structure before turbulence is attained. During the 1970's, the concept of orderly structure in turbulent flows began to gain

acceptance. Crowe and Champagne [20] manipulated the frequency of large-scale pattern formation in a round jet at Re $\sim 10^5$ by external acoustic excitation. They recorded their measurements at a point just four diameters away from the jet exit plane. Later on, Petersen and Samet [21] conducted the same experiment to demonstrate that the only instability is a shear layer one that is dependent on the streamwise distance from the nozzle, and in turn, on the local shear layer thickness. Browand and Laufer [22] visualized the flow in a circular water jet for $5000 < \text{Re} < 15000$. Their analysis distinguished between three regions. First, an initial shear layer instability zone, second, a vortex-rings interaction zone, and third, a zone prone to turbulence generation, thus order distortion. Davies and Yule [23] reviewed the contributions made in deciphering the nature of large-scale coherent structures reported in a wide range of shear flow turbulence, such as wakes, boundary & mixing layers, and jets. An overwhelming basic commonality was educed based on the evident repetitive features of those structures, albeit some unique characteristics that are only relevant to each particular flow.

The essence of coherent structures in turbulent shear flows is indeed intriguing, and far from being fully understood. Another interesting and related phenomenon is the induction of self-sustained oscillations. We shall particularly review such processes of impinging shear layers given their relevance to the study of virtual impaction. Rockwell and Naudascher [24] summarized the multitude of configurations where flow induced oscillations can come into play. The geometries range from jets impinging on flat or sharp edges, to mixing layers over cavities or curved surfaces. The underlying belief is that such flows exhibit an astounding set of common features namely, a high degree of disturbance organization, a distinct frequency of oscillation, and amenability to resonance. Ho and Nosseir [25] extensively analyzed the "feedback loop" in a subsonic air jet impinging on a flat plate. Their experimental results suggest a mechanism by which the surface pressure fluctuations, caused by the convected coherent

structures landing on the plate, produce *upstream* propagating waves which are phase locked with the separated shear layers from the nozzle. In a recent two-dimensional numerical study of the unsteady effects that an impinging slot jet flow has on the heat transfer diagnostics of the receiving plate, Chiriac and Ortega [26] identified the critical Reynolds number, that marks the onset of unsteadiness, to be ≈ 600. Their calculation revealed an advantage in heat transfer coefficient at the wall compared to the steady flow. Similarly, Akiyama *et al.* [27] performed a large eddy simulation on a domain involving two planar impinging jets at $\mathrm{Re} = 500$, with periodic boundary conditions in the spanwise direction. The jet was periodically forced in time in order to stimulate the emergence of coherent large-scale vortices from the nozzle shear layers. They also reported on structures with spanwise vorticity in the developing jet near the impingement wall.

One final arena of exploration related to the topic of coherent structures in jet flows, which also possesses common elements with virtual impaction, is the study of jets in cross flow. The formidable nature of this flow lies in the complex three-dimensional interaction between the main jet and the cross-stream which is generally of a lower velocity. A number of researchers visualized and explained the structural properties of this flow at high Reynolds numbers [28, 29, 30], but what is most interesting to us is the instability processes and organized motions at relatively low Reynolds numbers. Camussi *et al.* [31] obtained particle image velocimetry measurements in a transverse jet at $\mathrm{Re} \approx 100$, along with visualizations by laser induced fluorescence. They interpreted the change in the structural dynamics of the flow based on the effect of the jet-to-crossflow velocity ratio, and concluded that the instability mechanisms are different from those attributed to free uninhibited jets. Ironically, Megerian and Karagozian [32] who conducted experimental recordings in a similar configuration for a range of Reynolds number, $1500 < \mathrm{Re} < 7000$, identified from their spectra plots, a shear layer mode instability at a moderate Reynolds number (~ 2700) that is similar

in nature to that of a free jet. Evidently, the characterization of the true instability traits and the role of the Reynolds number is quite a controversial and non-trivial matter.

1.1.3 Particles in Turbulence

Truly, one of the most captivating issues in engineering is the understanding of fluid-particle interaction. Sadly, the most accurate numerical techniques for tackling this problem are still very prohibitive because direct numerical simulations attempt to resolve the full range of scales including the "wakes" behind each of the finite-size particles [33]. Fortunately, the physics is quite manageable when the particle diameter is much smaller than the smallest turbulent scale, i.e. the Kolmogorov length scale. Furthermore, for dilute particulate systems, it is safe to assume that the only transfer of momentum is from the fluid phase to the dispersed phase. Hence, a Lagrangian *one-way* coupled equation of particle motion that accounts for hydrodynamic forces on the particles is widely accepted [34]. Reviews for numerical methods that are suitable for computing particulate flows are numerous [35, 36, 37, 38]; we shall simply focus on the more recent work involving large eddy simulation (LES). The merits of large eddy simulation for complex engineering flows are very commendable. LES is an intermediate approach between expensive but accurate direct numerical simulation (DNS) and the Reynolds ensemble-averaged approach, or Reynolds average Navier-Stokes (RANS). Historically, the latter overture dealt with providing turbulence closure models for the Reynolds stresses appearing in the RANS equations, in order to solve for the mean properties of the fluid. Additional stochastic modeling, is in fact needed to simulate the effects of turbulent particle dispersion. Such techniques were highly prone to empirical arguments that frequently violated basic physical principles [39]. The prize of LES, on the other hand, lies in its ability to resolve the time dependent large scale fluid motions, while parameterizing the effect of the sub-grid

scale (SGS) turbulent stresses. A strong justification for this framework lies in the fact that SGS fluctuations are believed to be universal in character, and independent of the specific boundary conditions imposed on the flow. This methodology is especially useful for particle flows since the particle motion is intimately tied to the large-scale fluid structures, and it eliminates any of the guess work needed to prescribe instantaneous velocities, as is the case for RANS methods. Wang and Squires [40] reported on a large eddy simulation of a fully developed turbulent channel flow. They computed solid particle trajectories and accumulated statistics for three distinct particle sizes. It was shown that the particles experience an increase in mean velocity relative to the fluid with increasing Stokes number. Moreover, the root mean square fluctuation levels where higher for particles near the wall in the streamwise direction, but lower in the wall-normal and spanwise direction when compared to fluid profiles. The authors also quantify and demonstrate the "preferential concentration" behavior, in other words, the biased arrangement of particles by streaky turbulence structures. Good agreement with experiment was achieved, especially at moderate Reynolds number. Uijttewaal and Oliemans [41] performed an LES on a vertical pipe flow to study the processes of particle dispersion and deposition. Their calculations attest that small particles whose time scales are comparable to the turbulence integral scale are dispersed in a manner similar to fluid particles, if not slightly more, while larger particles exhibit much less dispersion by turbulence. Armenio *et al.* [42] assessed the contribution of small-scale velocity fluctuations on tracer and finite-inertia particle motions. With the help of reference DNS data of a turbulent channel flow, these workers discovered very limited effects on the statistics of particles with or without the incorporation of the sub-grid velocity field into the particle equation of motion, granted that a "careful" LES is performed, with regard to grid resolution and sub-grid scale model. Some alternative and equally cogent schemes for LES are also in existence. Derksen [43], for example, simulated the turbulent flow inside a stirred tank by large-eddy simulation

using the Lattice-Boltzmann method. Solid particle dynamics were then studied by considering particle-particle, and particle-impeller collisions. The analysis confirmed prior findings about the minor influence of the sub-grid scales. Lastly, Bernard *et al.* [44], using vortex methods, performed "grid-free" turbulent flow simulations of the spatially developing mixing layer in order to study the mixing posture of inertial particles relative to the organized roller structures.

1.1.4 Thesis Synopsis

Thus far, a general picture of virtual impaction flows has been portrayed, along with a summary of the diverse relevant experimental and theoretical studies pertaining to the problem. The remainder topics covered in this dissertation are outlined below:

- In Chapter 2 we will present the fundamental equations of fluid and particle motion along with the numerical schemes employed in their solution. The results of the two-dimensional geometry at different flow conditions will be compared and discussed, and a number of questions pertaining to the three-dimensional problem will be raised.

- Chapter 3 deals with the details of large eddy simulation. It covers the basic filtered equations and the closure models used for the determination of sub-grid scale turbulent stresses. An implementation of an advanced model is nominated along with its results from two validation cases.

- In Chapter 4, first we analyze the LES results of the round slit virtual impactor from a statistical standpoint, and then attempt to reconstruct the flow dynamics in conjunction with analyzing the particle tracking results. Mechanisms for particle transport and loss are discussed.

- Chapter 5 concludes with a summary of the main findings from each study. Recommendations for future research are made in this chapter.

Chapter 2

Two-dimensional Theoretical Study

It is well known that the cost of conducting a direct numerical simulation of the Navier-Stokes equations requires a number of grid points proportional to $Re^{3/4}$ in each Cartesian direction, based on the adopted Kolmogorov theory for turbulent flows [45]. Therefore, the computational expense for a transient three-dimensional calculation at a relatively mild Reynolds number (~ 2000), and in the presence of solid boundaries, becomes quite intolerable connoting the scaling relationship of $O(Re^3)$. For our particular case, given that such a scenario is prevailing, and the fact that we are interested in learning about the fundamental mechanisms of virtual impaction jets, we elect to conduct a two-dimensional *direct* simulation. In fact, two-dimensional flow approximations can provide considerable insight to the analysis of the problem, and the 2-D assumption is not very crude if the third dimension (spanwise) length scale is significantly larger than the representative length scale of the flow, for example the jet width. In the following sections, the governing theoretical equations are outlined, and the numerical tools employed in their solution are presented. The remaining part of the chapter deals with the analysis of both the fluid and discrete phase results.

2.1 Equations of Fluid Motion

The treatment of the physics of fluid motion is justifiably perceived via the continuum hypothesis, in other words, the world-size length and time scales important to the study of most engineering flows exceed those of the molecular scales [46]. We shall limit this examination to Newtonian fluids with constant density in an Eulerian frame of reference. Therefore, we write the mass-conservation, known also as the continuity equation:

$$\frac{\partial \rho}{\partial t} + \frac{\partial (\rho U_i)}{\partial x_i} = 0. \tag{2.1}$$

The condition that ρ is independent of both $\mathbf{x}$ and t, reduces the continuity equation to its solenoidal form:

$$\frac{\partial U_i}{\partial x_i} = 0. \tag{2.2}$$

The momentum equation which is derived in a manner similar to Newton's second law of motion, is essentially a balance between the rate of change of momentum per unit volume on one hand, and the pressure, viscous, and body forces on the other. The differential form of the equation is given by:

$$\frac{\partial U_i}{\partial t} + U_j \frac{\partial U_i}{\partial x_j} = -\frac{1}{\rho}\frac{\partial P}{\partial x_i} + \nu \frac{\partial}{\partial x_j}(\frac{\partial U_i}{\partial x_j}) + g_i. \tag{2.3}$$

By convention, equations (2.3) in combination with equation (2.2) are referred to as the Navier-Stokes equations.

2.2 Equation of Particle Motion

Before we discuss the form of the equation of particle motion, it is important to establish the assumptions under which such an equation holds. There are two

crucial elements related to the derivation of the Maxey and Riley theory. First, the particle size is taken to be much smaller than a characteristic length scale of the fluid velocity field, and second, the Reynolds number based on the sphere's diameter is small compared to unity. In nature, a suspension of dilute aerosols (low volume fraction) is believed to be insensitive to inter-particle collisions [47]. Hence, when viewed from this perspective, it becomes reasonable to derive an equation for the particle motion based on the unsteady disturbed Stokes flow around the sphere:

$$m_p \frac{d\mathbf{V}}{dt} = 6\pi r_p \mu(\mathbf{U}-\mathbf{V}) + \frac{1}{2} m_f \frac{d(\mathbf{U}-\mathbf{V})}{dt} + m_f \frac{D\mathbf{U}}{dt} \tag{2.4}$$
$$+ 6r_p^2(\pi\mu\rho)^{\frac{1}{2}} \int_0^t \frac{d(\mathbf{U}-\mathbf{V})/d\tau}{(t-\tau)^{\frac{1}{2}}}\, d\tau + (m_p - m_f)\mathbf{g},$$

where D/Dt is the substantial derivative. The terms in the above equation represent a balance between the inertia force due to the particle acceleration on the left hand side, with the Stokes drag, inertia of virtual mass, fluid pressure gradient and viscous stresses, the Basset memory term (unsteady form of viscous drag), and gravity-buoyancy on the right hand side, respectively. A number of studies ascertained the contribution of each of the individual terms in order to map their relative importance [48, 49]. A major simplification occurs for aerosols due to their high particle density compared to that of the fluid ($\rho_p/\rho \approx 10^3$), and it was found that the steady state drag is the primary force. Thus, dividing both sides of equation (2.4) by m_p and discarding the negligible terms, we obtain:

$$\frac{d\mathbf{V}}{dt} = \frac{18\mu(\mathbf{U}-\mathbf{V})}{\rho_p d_p^2} + \mathbf{g}, \tag{2.5}$$

which has been empirically modified to incorporate non-creeping flow deviations of the drag force from the steady Stokes solution. Therefore:

$$\frac{d\mathbf{V}}{dt} = \frac{C_D Re_p}{24}\frac{(\mathbf{U}-\mathbf{V})}{\tau_p} + \mathbf{g}, \tag{2.6}$$

where $\tau_p = \rho_p d_p^2/18\mu$, and $Re_p = d_p|\mathbf{U}-\mathbf{V}|/\nu$. The choice of the drag coefficient, as we found in a separate investigation [13], is utterly consequential especially during virtual impaction. It was shown that minute changes in the magnitude of the drag force on the particle during its "turn-negotiation", or virtual impinging, makes the difference between whether the particle will jump into the minor flow, or escape to the major flow. For this reason, a best practice approach was devised to allow for adaptive drag models that can respond to rather abrupt changes in the relative velocity $(\mathbf{U}-\mathbf{V})$. Hence, the following criteria are used to prescribe the drag coefficient:

$$\begin{aligned} C_D &= \frac{24}{Re_p}; && Re_p \leq 0.1 \\ &= \frac{24}{Re_p}(1+3/16Re_p); && 0.1 < Re_p \leq 5 \\ &= \frac{24}{Re_p}(1+0.15Re_p^{0.687}); && Re_p \geq 5 \end{aligned} \tag{2.7}$$

The above relations are commonly known as the Stokes, Oseen, and non-linear (experimental fit) drag model, respectively [50]. It should be noted that the Stokes flow analysis relies on the presumption that the velocity of the gas right at the surface of the moving sphere is zero. Aerosol particles, however, when their size becomes comparable to the mean free path of the gas, experience what is commonly referred to as "slip" [51]. Effectively, this implies a reduction in the Stokes drag force for micron-size particles or less, which can be quantified by the Cunningham correction factor

$$C_c = 1 + \frac{2}{Pd_p}\left[6.32 + 2.01e^{-0.1095Pd_p}\right], \tag{2.8}$$

which enters the denominator of the leading coefficient in equation (2.6). Note that the pressure dependence of the previous relation is dynamically taken into account

based on the particle's surrounding fluid pressure.

2.3 Numerical Setup

2.3.1 Geometry & Flow Conditions

The computational domain utilized for the two-dimensional study is shown in figure 2.1. The nozzle width is $W = 0.7\ mm$. The inlet cone converges at a 45^o angle into a throat section approximately twice the length of the jet opening ($T \sim 2.1W$). The gap distance to the collection probe is also $S \sim 2.1W$. The probe width is $W_c = 1.5W$. Such critical dimensions follow the literature recommendations, and are also the outcome of our own preliminary "test runs" that looked at their effect on the jet expansion characteristics. The axes in the insert of figure 2.1 are made dimensionless to facilitate the discussion of the results:

$$\begin{aligned} x^* &= \frac{x - x_{nozzle}}{S} \\ y^* &= \frac{y}{W}. \end{aligned} \tag{2.9}$$

An inflow boundary condition is specified at the cone inlet, which simply designates a uniform velocity across that plane. Three sets of simulations were performed each with a different inflow velocity U_{in}, and thus a different jet Reynolds number ($Re \equiv WU_j/\nu$). The simulations' parameters are summarized in Table 2.1. The Reynolds number $Re_\delta = \delta U_{oo}/\nu$, is defined based on the jet initial shear layer thickness which is taken to be the distance from the wall to the point where the streamwise velocity is 99% of its centerline value U_{oo}. The average time for virtual impaction τ_{vi} is the ratio S/U_j. The last two columns of Table 2.1 point to the time step, and number of grid cells used in the computations.

U_{in} (m/s)	U_j (m/s)	Re	Re_δ	τ_{vi} (s)	Δt	Total Grid Cells
0.3	7.4	356	218	$1.99e^{-4}$	$\tau_{vi}/20$	135×10^3
1.9	44.6	2136	579	$3.32e^{-5}$	$\tau_{vi}/33$	663×10^3
3.3	74.3	3561	723	$1.99e^{-5}$	$\tau_{vi}/20$	663×10^3

Table 2.1: Summary of simulation conditions

A sample numerical mesh is shown in figure 2.2 for the low Reynolds number case. More explicitly, in the area $W \times S$, 60×148 non-uniform grid points were distributed. Similarly, 120×296 for the higher Re cases. Needless to say, care was taken to cluster enough nodes near the walls and high shear regions. Grid independence was established for the medium Reynolds number case by comparing the results from a coarser mesh. In all cases, the first cell near any given wall in the domain lied within the viscous sublayer. For the outflow boundary conditions, a specified mass flow weighting is used in order to *force* the flow to undergo a $10 - 90\%$ throughput expansion to the minor and major flow, respectively. In addition, a convective treatment is imposed on the outflow cell velocities in order to allow any flow disturbances to smoothly exit the domain [52]. Details about the implementation and its validation can be found in the Appendix. If the location of the outflow boundary condition (OBC) is too close to the jet, then it can be detrimental to the accuracy of the simulation. For this reason, we extended the lateral position of the outflow planes to $y^* \approx 27W$, after examining the results of a test calculation with OBC at $y^* \approx 13W$.

2.3.2 FLUENT Code

FLUENT's finite volume code is used to numerically solve the Navier-Stokes equations. A brief description of the numerical algorithm will be outlined in this section. A "segregated" methodology is undertaken to solve the mathematically coupled nonlinear transport equations. This implies that each of the unknown variables is

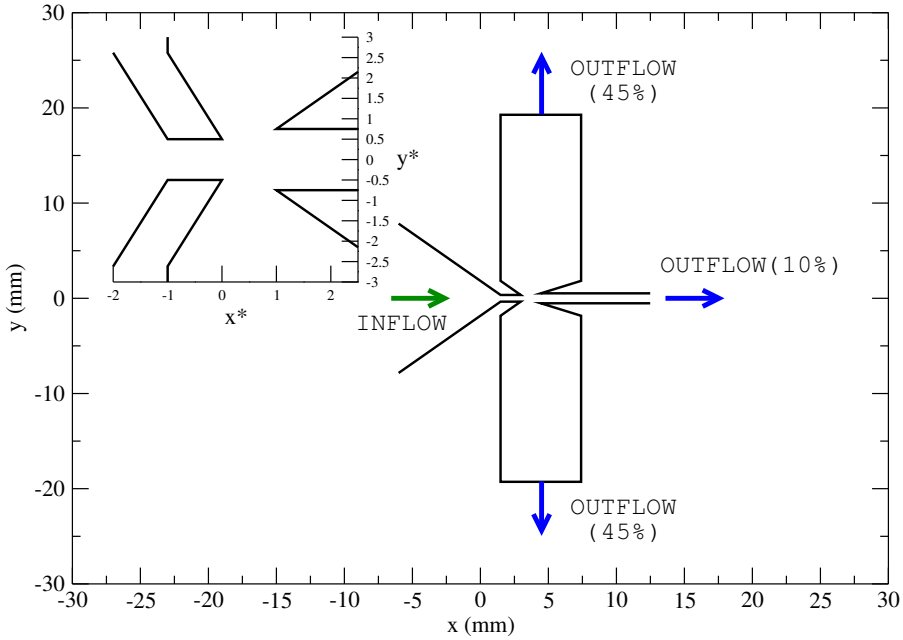

Figure 2.1: Domain used for 2-D Navier-Stokes simulations drawn to scale in World coordinates. Insert shows nozzle section with dimensionless axes

solved for sequentially starting with the momentum equation, and using the continuity equation to enforce mass conservation implicitly on each control volume. Using the divergence theorem, the conservation laws are transformed into integrals of flux over the surfaces (F) of each computational cell of volume V. Integrating the velocity divergence, for instance, becomes:

$$\iiint_V \nabla\cdot\mathbf{U}\ dV = \iint_S \mathbf{U}\cdot\mathbf{n}\ dF, \tag{2.10}$$

where $\mathbf{n}$ is the unit vector normal to each face. The discretization of the continuity equation (2.2) then yields:

$$\sum_f^{N_f} \mathbf{U}_f\cdot\mathbf{A}_f = 0, \tag{2.11}$$

where $\mathbf{A}_f$ & N_f are the area and number of faces (4 in 2-D, 6 in 3-D) associated with

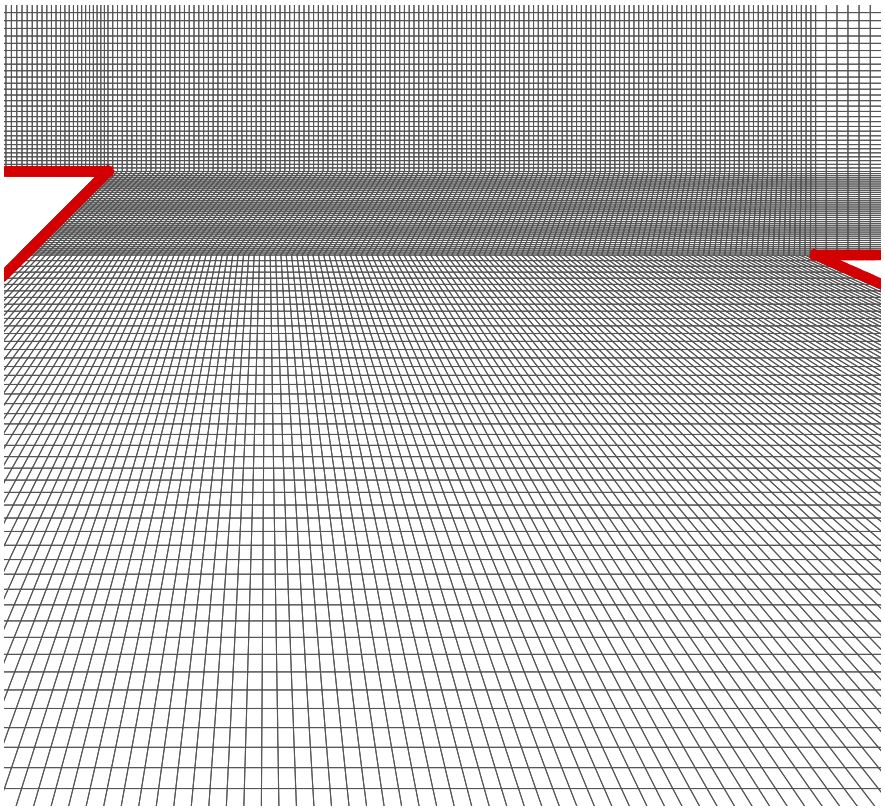

Figure 2.2: Low Re case numerical mesh - upper boundary marks jet centerline

each control volume, respectively. The same procedure is applied to the conservation of momentum, which when written for the entire lattice of grid cells in the domain yields a set of algebraic equations with a sparse coefficient matrix. Consequently, an iterative tool (Gauss-Seidel) is used to converge the equations on a global basis. Further details on the intermediate steps of the solver can be found in the reference manual [53]. It should be noted that proper measures and reliably proven algorithms [54] were chosen in order to insure the accuracy of the results. The main concerns, for example, relate to the residual numerics $O(10^{-5})$, the discretization, and pressure-velocity coupling schemes, which are summarized in Table 2.2 for both the 2-D Navier-Stokes and Large Eddy simulation.

	Time (backward)	Pressure	Momentum	P-V Coupling
2-D NS	2^{nd} *order*	2^{nd} *order*	QUICK*	SIMPLEC
LES	2^{nd} *order*	2^{nd} *order*	Central	SIMPLEC

Table 2.2: Summary of discretization schemes. *hybrid upwind-central

2.3.3 Particle Tracking Code

In order to obtain Lagrangian particle statistics, equation (2.6) is integrated twice to arrive at the particle position vector $\mathbf{x}_p$. For numerical analysis purposes, we re-write the particle system of equations as:

$$\frac{d\mathbf{x}_p}{dt} = \mathbf{V} \tag{2.12}$$

$$\frac{d\mathbf{V}}{dt} = \beta(\mathbf{U} - \mathbf{V}) + \mathbf{g} \tag{2.13}$$

where $\beta = C_D Re_p/(24\tau_p C_c)$. An in-house developed code reads in the fluid velocity field at each time step, and employs the second order Adams-Bashforth marching

scheme to advance the particles. The above equations are then explicitly progressed forward in time as such:

$$\mathbf{x}_p^{n+1} = \mathbf{x}_p^n + \Delta t \left[(1+\alpha)\mathbf{V}^n - \alpha \mathbf{V}^{n-1}\right] \quad (2.14)$$

$$\mathbf{V}^{n+1} = \mathbf{V}^n + \Delta t \left[(1+\alpha)\beta^n(\mathbf{U}^n - \mathbf{V}^n) - \alpha\beta^{n-1}(\mathbf{U}^{n-1} - \mathbf{V}^{n-1}) + \mathbf{g}\right] \quad (2.15)$$

The parameter $\alpha = 0.5$ corresponds to time steps proceeding the initial step (t_0), for which $\alpha = 0$ due to the absence of the $(n-1)^{th}$ velocity (i.e. Euler scheme). The stability of explicit integration schemes is dependent on the finite size of Δt, however, for sufficiently small time steps ($\Delta t \ll \tau_p$) the fidelity of the computation can be ensured. Another more significant source of numerical error stems from interpolating the fluid velocity at the meshpoints to the instantaneous particle position. A number of techniques have been proposed and evaluated over the years (see for example [55]), and it was found that this error can be alleviated with high order interpolation schemes and fine grids. A versatile and accurate (2^{nd} order in space) approach based on weighted inverse-distance interpolation [56, 57] is used to allow effortless extension of the code to unstructured grids. A thorough description and assessment of this method can be found in a previous work [13].

2.4 Results

The discussion of the simulations' results obtained for the three cases summarized in Table 2.1 is undertaken in the following sections. The analysis is initiated from two points of view. First, the mean or long-time averaged flow fields are inspected and compared. Second, the transient mechanistic properties of the flow are accentuated and explained.

2.4.1 Time Averaged Flow

For an unsteady problem, the mean flow is a mathematical artifact, but it serves as an analytical tool for the base flow over which we may envision the transport of rudimentary vortex structures. In addition, it facilitates the comparison of different case data and other published results. For the sake of this study, namely the existence of three flow conditions of interest, and the historical tradition of utilizing the base mean flow as a sustainable measure of the performance of a virtual impactor, the time-averaged results will be addressed. With reference to the virtual impaction time unit τ_{vi}, a large number of flow realizations from each flow condition is recorded, as listed in Table 2.3. First and second order statistics are then computed as such:

$$U_i^{avg} = \frac{1}{N_t} \sum_{j=1}^{N_t} U_i(t_j), \tag{2.16}$$

$$U_i^{rms} = \left[\frac{1}{N_t} \sum_{j=1}^{N_t} (U_i(t_j) - U_i^{avg})^2 \right]^{1/2}. \tag{2.17}$$

For the moment, case I, based on its low Reynolds number, can be safely considered to be in the laminar regime, whereas case II and III, may be loosely referred to as transition and turbulent, respectively. Such designated categories will become more justified when we examine the unsteady flow.

Case #	U_j (m/s)	Re	N_t	$N_t \Delta t / \tau_{vi}$
I	7.4	356	2000	100
II	44.6	2136	2311	70
III	74.3	3561	1380	70

Table 2.3: Flow realizations saved in each simulation

The flow in free (unbounded) jets is normally distinguished based on streamwise distance from the issuing nozzle [58]. First, close to the nozzle, a "potential core" region extends in the axial direction with an undiminished mean velocity equal to U_o.

Surrounding this unweakened region, above and below, lies the mixing layers. Further enough downstream, the strength of the core region is diffused, and the mixing layers migrate to the centerline to mark the beginning of the "fully developed region", which conveniently has been shown to be self-preserving, that is, the cross-stream variation of mean velocity takes on identical shapes at each subsequent axial location. This behavior, of course, is not observed in a virtual impactor jet. First, the flow in the immediate proximity of the nozzle is bounded. Second, hydrodynamic pressure gradients are acting to decelerate the flow in the axial direction, and induce curvature in the transverse direction. All of this is happening in an extremely short distance, and fast time scales. For the sake of realizing the jet character, we plot the variation of streamwise mean velocity at several x stations, marked in figure 2.3, in the virtual impaction gap. The velocity profiles are normalized by the centerline velocity at the corresponding x location. Figures 2.4, 2.5, and 2.6 show the U_x^{avg} velocity profiles for the three cases, respectively. In the laminar case, it is clear that a pseudo-parabolic profile is predominant at all stages of the jet expansion. Moreover, the degree of self-similarity is minimal, in other words, there is no fully developed region. Cases II & III, exhibit quite similar behavior for the streamwise velocity during virtual impaction. Most pronounced is the flat profile at the first two sampling stations compared to the parabolic profile of case I. Slightly before the jet half point to collection, there is strong distortion of this flatness, which results in a relative faster "leakage" above and below the centerline. In figures 2.5, and 2.6, the appearance of local maxima corresponds to the transverse location of the nozzle boundaries at $y^* \approx \pm\ 0.5$, and continues for several distances downstream. This implies, that the shear layers are, on average, traveling faster than the centerline. Furthermore, it should be pointed out that as the fluid approaches the minor flow entrance, the mean velocity quickly adjusts to accommodate the re-laminarization process, as witnessed by the change in shape of the streamwise velocity profile.

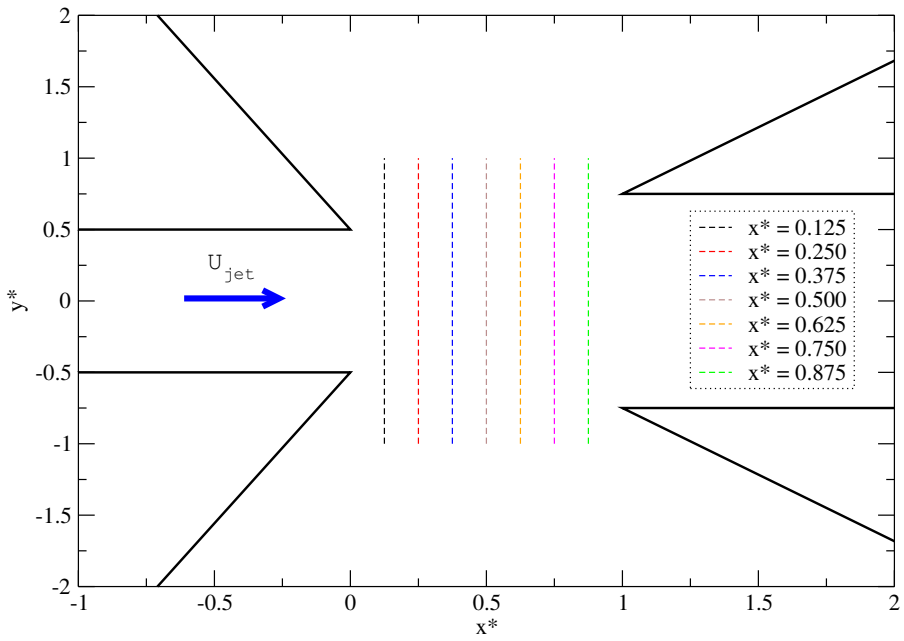

Figure 2.3: Virtual impaction jet 'x stations'

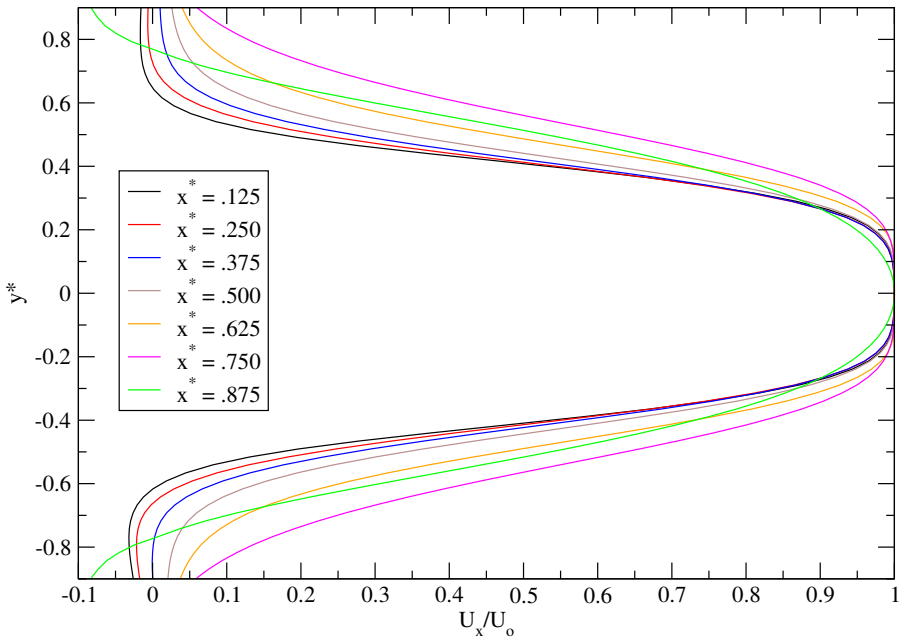

Figure 2.4: Virtual impaction jet time averaged streamwise velocity - Case I

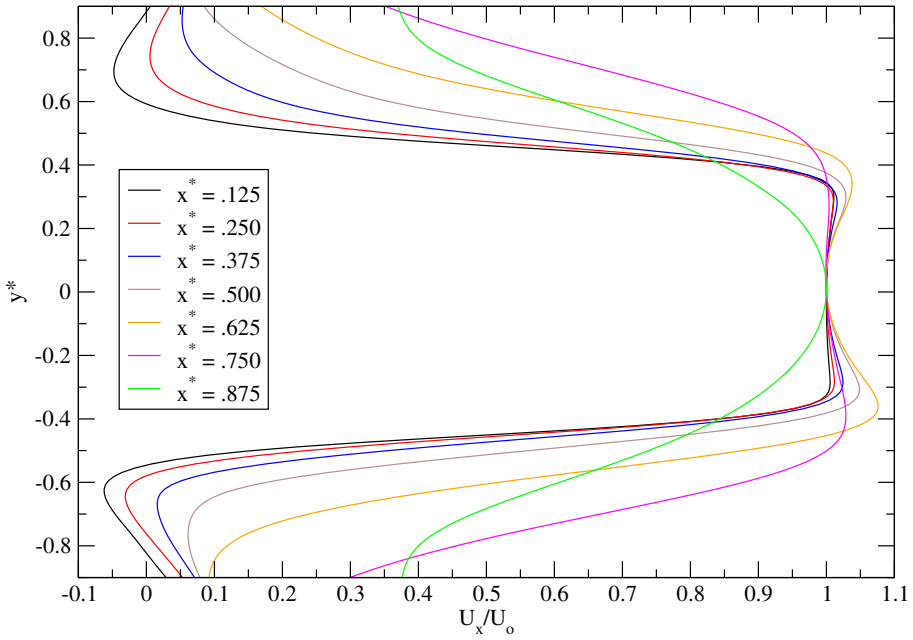

Figure 2.5: Virtual impaction jet time averaged streamwise velocity - Case II

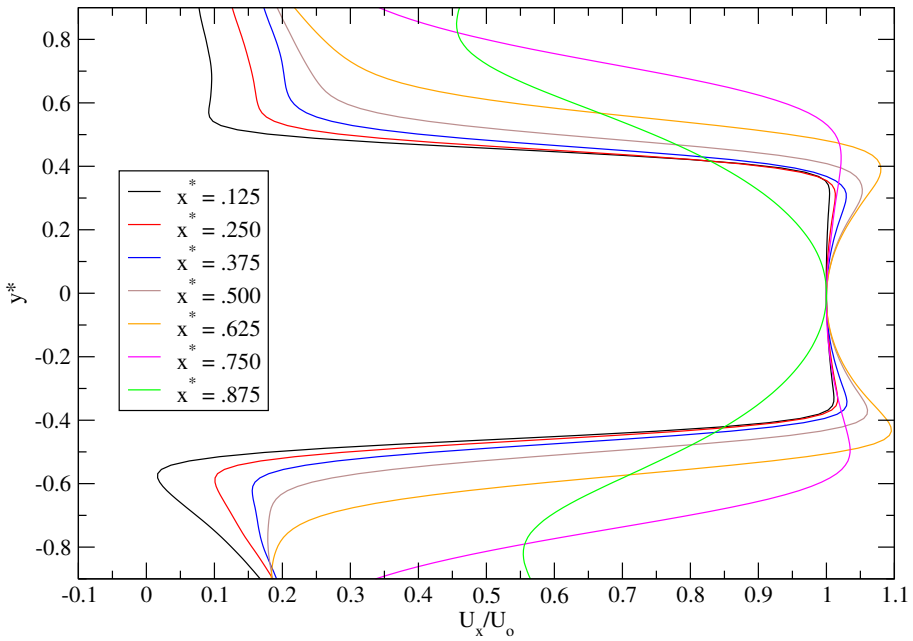

Figure 2.6: Virtual impaction jet time averaged streamwise velocity - Case III

The expansion characteristics of the jet can also be quantified by the half-breadth measure (b), which is equal to the lateral distance from the jet axis to the point where the streamwise velocity is one-half the centerline velocity. Figure 2.7 shows the variation of b with dimensionless downstream distance, $x^* = (x - x_{nozzle})/S$, for all three cases. It is shown that the initial development of breadth is constant up to $x^* \approx 0.5$, but with a higher magnitude for case II & III. The final stages of breadth development show a dramatic increase more so for the higher velocity cases. This is naturally an outcome of the re-laminarization and widening of the velocity profile near the entrance of the probe.

To investigate the existence of a potential core, we monitor the behavior of the jet mean centerline velocity. Figure 2.8 shows the streamwise velocity at $y = 0$ for all three cases, normalized by U_{oo}, as a function of dimensionless axial distance. Evidently, the centerline velocity behavior for case II & III is identical, namely a swift decadence of the potential core region in comparison to the laminar case which exhibits an increased penetration with downstream distance. The dashed lines on the figure indicate the location of the inflection points of the graphs. In all cases, however, there seems to be an agreement on the overall reduction in centerline velocity by the time the flow reaches the probe which is roughly 90% of the initial nozzle speed. An overall picture of the jet penetration and deflection of its streamlines is depicted in figures 2.9, and 2.10 for case I and III, respectively. It is shown, that despite the higher nozzle velocity of case III, the penetration length is relatively shorter than case I. Furthermore, the deflection or curvature profile of the two cases is achieved at different angles of inclination with respect to the axial flow.

To further analyze this phenomenon, we plot the cross-stream time averaged velocity at several y-stations within the virtual impaction gap, as drawn in figure 2.11. The magnitude of the cross-stream velocity U_y^{avg}, is minuscule in the early development of the jet near the issuing nozzle, but begins to gradually increase to

reach a local maximum just before the entrance of the receiving nozzle. The graphs in figure 2.12 are representative of this behavior, which is shown only for case I, and normalized by the corresponding maximum velocity at each y-station. The remaining two cases, not shown here, exhibit similar trends but obviously with a higher velocity magnitude.

In order to obtain a comparative insight to the deflection mechanism of the mean flow, we plot in figure 2.13 the locus of the (x, y) points where the maximum cross-stream velocity is found for all three cases. The outcome plot is astonishingly indicative of the role that the Reynolds number plays in steering the jet curvature. It is seen that in the laminar case, in addition to the deeper axial jet penetration revealed in figure 2.8, there is also an affinity to delay the growth of the lateral jet until roughly 83% of the virtual impaction gap length, as shown in figure 2.13. Contrary to common perception, the higher Reynolds number cases, despite their more vigorous nozzle conditions are prone to start the deflection process earlier than the laminar case, $\sim 79\%$ & 77%, for case II and III, respectively. Moreover, the maximum cross-stream velocity locus for the latter two cases remains narrowly banded, compared to the laminar case which shows a preference to spread over a wider axial scale. The natural bifurcation of a free jet into a cross flow is depicted in figure 2.14 for three increasing ratios of the jet-to-cross flow velocity, and it can be easily discerned that for stronger jets, the locus penetration is copious.

One important aspect of the mean flow in a virtual impactor is the pressure drop (ΔP) incurred in "pushing", or "pulling" the fluid across the nozzle. From a preservation point of view, the pressure conditions may become critical to the survival of some bioaerosols. From a practical standpoint, as well, the pressure drop is directly proportional to the power consumption of the device in Watts. Hence, figure 2.15 shows the gauge pressure variation along the jet axis for all three cases. The corresponding total adverse pressure gradients between jet and collection planes,

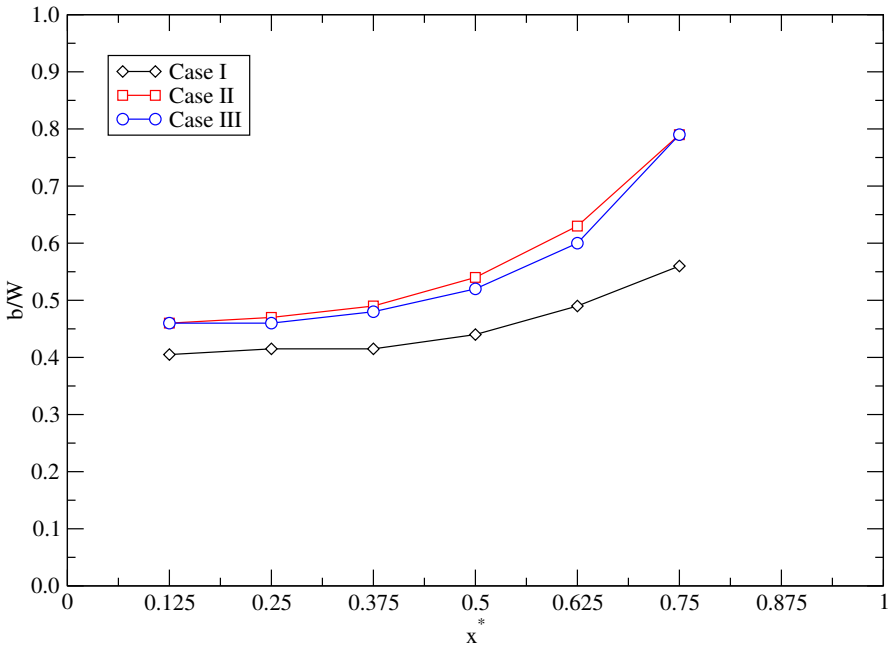

Figure 2.7: Half breadth of virtual impaction jets

reported in inches of water, are: 0.2, 6.1, and 16.2 for case I, II, and III, respectively.

The knowledge of the behavior of the mean velocity components is crucial in the design of efficient and versatile virtual impactor jets, and indeed, there is a degree of ambiguity among designers and builders of such systems, as to the role of the Reynolds number on the mean characteristics of the jet. We have shown that once we diverge from laminar conditions, the jet potential core is diminished, and at the same time its cross-stream strength is invigorated which can lead to the counter effect of less minor flow penetration. The fluid mechanical reasons why such behavior occurs can be recognized by learning about the instability characteristics of the jet, which we shall discuss in the unsteady flow section.

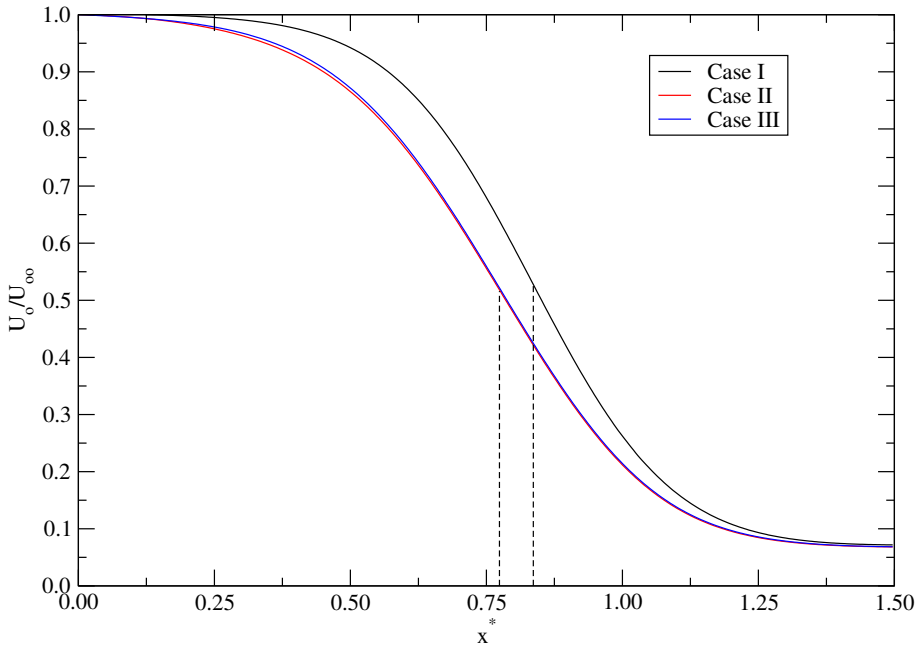

Figure 2.8: Variation of virtual impaction jets centerline velocity

2.4.2 Aerosol Collection & Loss

Having established some of the most influential properties of the carrier phase mean flow in the virtual impactor for the three distinct flow conditions, we shift our attention now to study the aerosol particle motion, and the consequences that the flow conditions impose on the discrete phase transport properties. In choosing the aerosol particle sizes two approaches are followed. First, we carry the trajectory calculations with mono-dispersed injections in order to evaluate the collection efficiency and losses. Second, a poly-disperse size distribution is assigned and sampled at different stages within the virtual impactor in order to assess the aerosol enrichment. In both cases, a large number of particles (close to $100,000$) is used for each injection. Trial runs with 1 million particles showed unnoticeable differences. The starting positions are randomly chosen within the inlet cone section of the device, and the particles are assigned the same initial velocity as the surrounding fluid. Clearly, since the particle

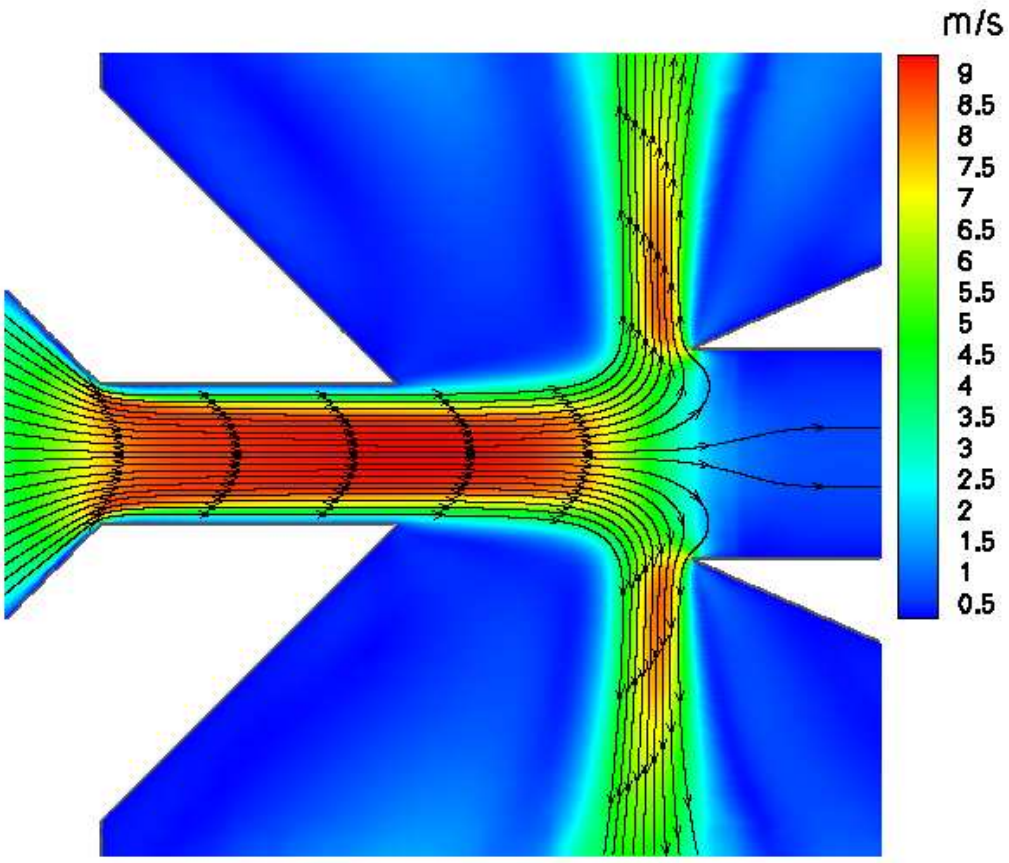

Figure 2.9: Mean velocity contours and virtual impaction streamlines - Case I

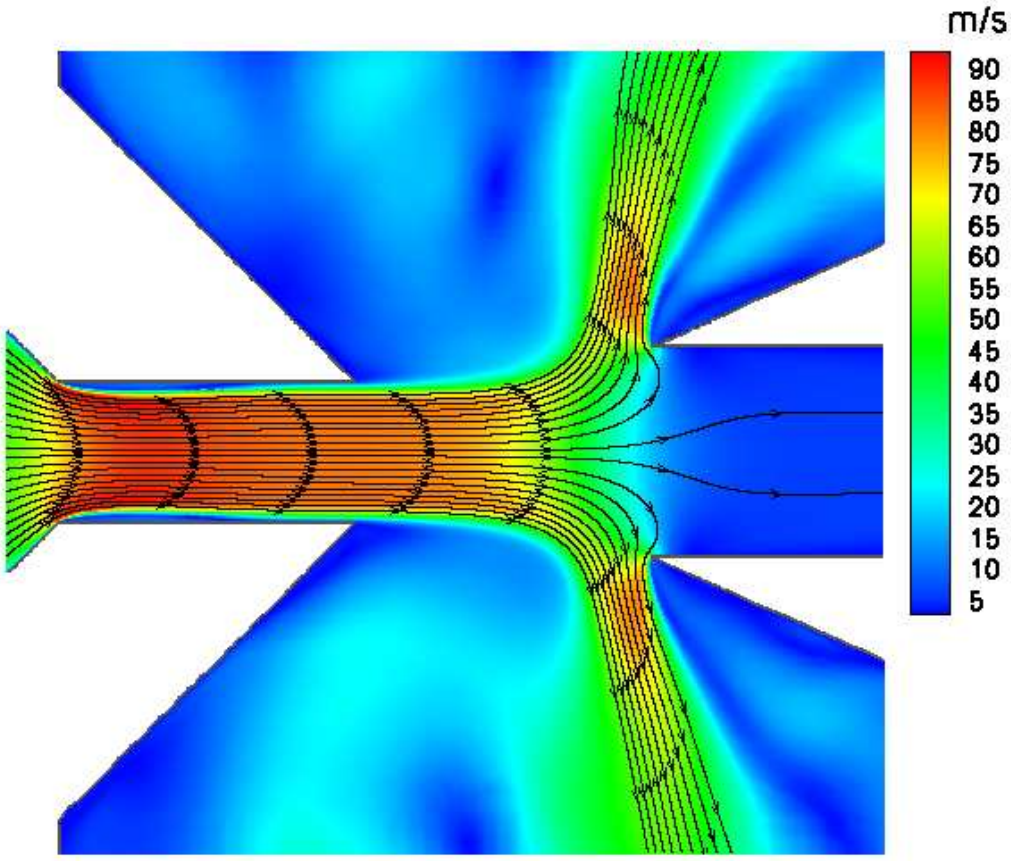

Figure 2.10: Mean velocity contours and virtual impaction streamlines - Case III

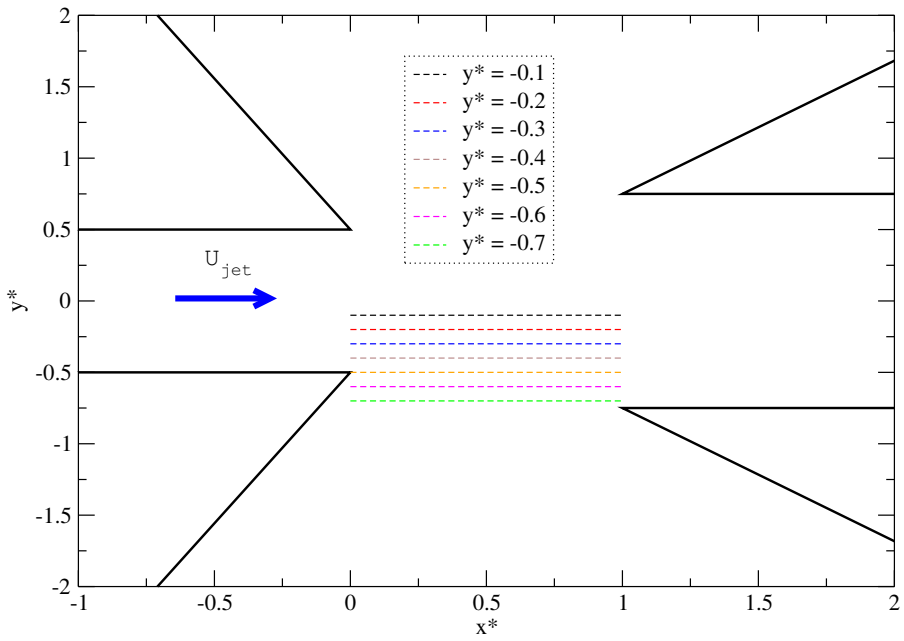

Figure 2.11: Virtual impaction jet 'y stations'

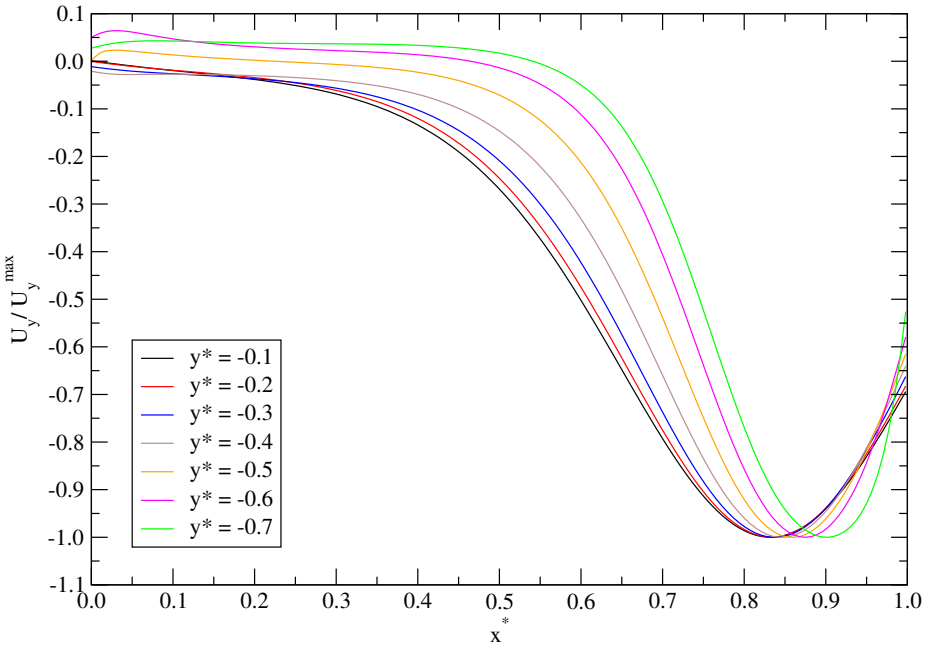

Figure 2.12: Cross stream jet velocity during virtual impaction - Case I

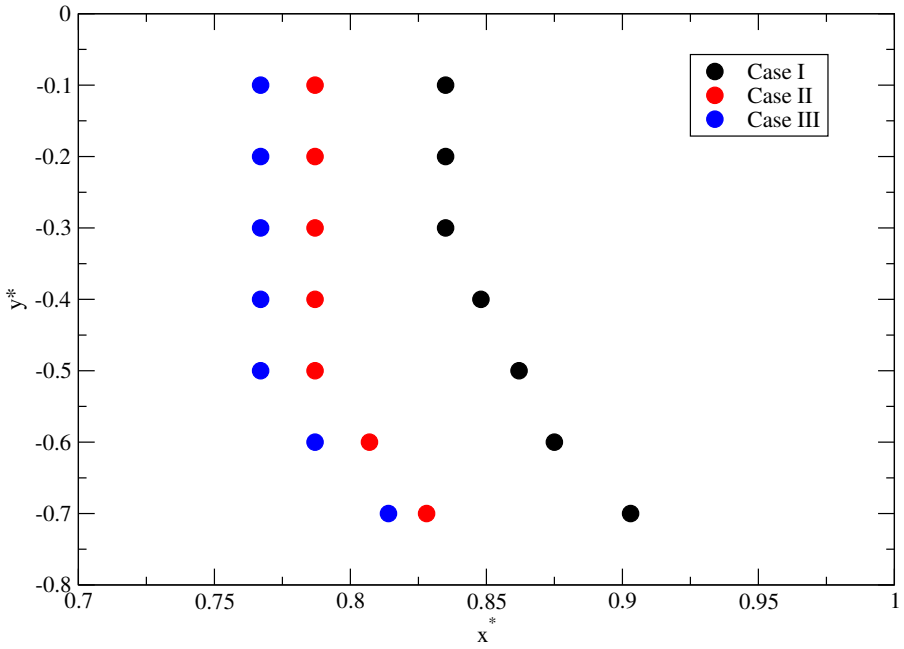

Figure 2.13: Loci of maximum cross-stream velocity during virtual impaction

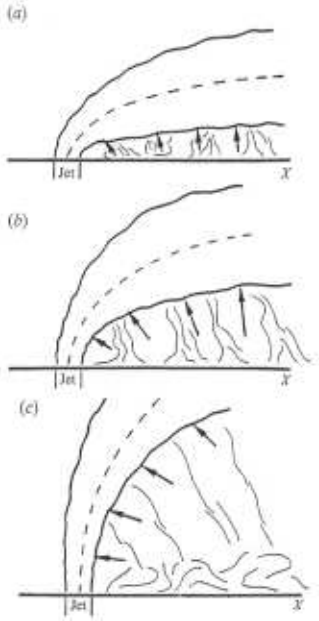

Figure 2.14: Free jet issuing into a cross stream flow. Effect of jet-to-crossflow velocity ratio from [28]. (a) *lowest* to (c) *highest*

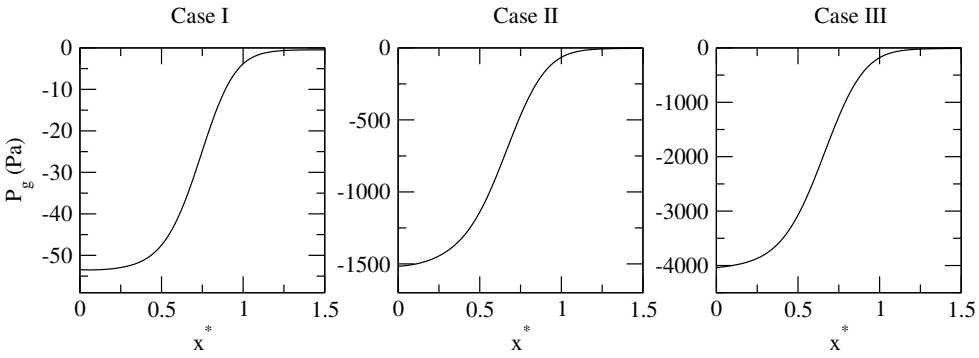

Figure 2.15: Pressure variation on virtual impaction jet axis

inertia at the virtual impactor nozzle is the determining factor for classification, the aerodynamic diameter range must be chosen differently for each flow rate (i.e. jet velocity), so that we observe similar separation characteristics by each flow field. Table 2.4 categorizes the diameters used for the particulate injections in each flow simulation. The slip correction factor of equation (2.8), and particle Reynolds number are also listed. The former tabulated values are computed based on ambient pressure in the inlet. Naturally, the instantaneous C_c is bound to change along the particle path as it experiences different pressure conditions, but it is shown to illustrate the degree of drag reduction we can expect. The Re_p tabulated values are estimated based on 1% relative velocity magnitude, and are shown to merely portray an exemplary range. The solid density of the spheres is $\rho_p = 1047 kg/m^3$. As can be seen, all three cases share a common set of Stokes numbers, defined in equation 1.2.

The particle separation efficiency, which is a measure of the effectiveness of the virtual impactor to separate particles, is calculated at the end of each Lagrangian tracking simulation, and is defined as:

	Case I			Case II			Case III		
St	d_p	C_c	Re_p	d_p	C_c	Re_p	d_p	C_c	Re_p
0.05	1.75	1.095	1.02	0.72	1.233	0.42	0.55	1.301	0.32
0.10	2.48	1.067	1.45	1.01	1.164	0.59	0.78	1.212	0.46
0.15	3.03	1.055	1.77	1.24	1.134	0.72	0.96	1.173	0.56
0.20	3.50	1.047	2.05	1.43	1.116	0.84	1.11	1.150	0.65
0.25	3.92	1.042	2.29	1.60	1.104	0.94	1.24	1.134	0.72
0.50	5.54	1.030	3.24	2.26	1.074	1.32	1.75	1.095	1.02
0.75	6.78	1.025	3.97	2.77	1.060	1.62	2.14	1.078	1.26
1.00	7.83	1.021	4.58	3.20	1.052	1.87	2.48	1.067	1.45

Table 2.4: Particle diameters in μm used in each flow simulation

$$\text{Eff} = \frac{\text{\# minor flow particles}}{\text{\# of minor + major flow particles}}, \tag{2.18}$$

whereas the losses due to particle deposition on the probe walls are simply accounted for by the following ratio:

$$\text{Loss} = \frac{\text{\# of deposited particles}}{\text{total \# of particles}}. \tag{2.19}$$

Figure 2.16 is a comprehensive plot of the collection efficiency as a function of particle diameter for each flow simulation. Also shown are experimental data by Ding & Koutrakis [7] from a geometrically similar virtual impactor under different velocity conditions. Evidently, the overwhelming trend is the shift of the efficiency curve towards lower cutpoints with increasing Reynolds number. The theoretical curves exhibit the desirable properties of steep slopes, and sharp separation between fine and coarser particles. The experimental data, obtained with larger nozzle dimensions ($W_{exp} \simeq 4.35W$), serve to demonstrate that the simulation predictions do indeed resemble the correct shape and structure. Such plots also reveal that the Reynolds number is not a universal dimensionless group for design, since the theoretical systems consistently capture smaller particles even at lower Re values than the experiment.

On the other hand, a more beneficial plot for design is figure 2.17, which plots the same theoretical collection results as a function of the Stokes number. In addition, the degree of particle losses on the virtual impactor walls is depicted. As can be seen, the numerical data collapses onto a common curve. Despite the slight deviations for the results of case I, namely the gradual rather than sudden increase in wall loss prior to the peak which is due to the nature of the underlying laminar flow, the graphs elucidate that the most active or sensitive orbit for classification occurs within the $0.10-0.25$ range of Stokes numbers. Moreover, the 50% cutpoint is around $St_{50} \approx 0.15$ ($\sqrt{St}_{50} \approx 0.39$). The wall loss peak is etched at $St = 0.20$, with a maximum of $\sim 10\%$ which is well below the acceptable norm for most virtual impactors.

The information gained from figures 2.16 and 2.17 has been the classical quest for the majority of virtual impactor investigations. Undoubtedly, it is relatively facile to conduct experiments or computations with mono-dispersed samples of particles, and the analysis of such data is consequently easier. However, it is essential to deal with complex conditions, in order to realistically assess the performance of a prototypical design. To this end, we propound to study poly-disperse aerosol distributions. First, the suspended particles in the inlet-cone are assumed to have diameters distributed in a log-normal fashion, using the following probability density function:

$$f(d_p; d_m, \sigma) = \frac{1}{d_p \sigma \sqrt{2\pi}} e^{-\ln^2(d_p/d_m)/2\sigma^2} \tag{2.20}$$

where d_m and σ are the mean and standard deviation, respectively. The resultant *discrete* number density of the particles is shown in figure 2.18 for four different values of σ. Lagrangian computations are then performed with each individual group using the mean velocity vector field of case II, and the aerosol size-distribution is queried at three vertical cross-sections: before, at, and after virtual impaction. Those sampling stations are hereinafter referred to as 'nozzle', 'collector', and 'minor flow'. Figure 2.19 presents the variation of the initial arrangements. First, we notice that the particle

size-distribution is unaltered by the time it reaches the nozzle, which is expected since no significant deposition occurs in the throat. Surprisingly, figure 2.19-a with the narrow distribution centered around $2\mu m$ experiences very little separation of size at the intermediate collection stage (i.e. probe entrance), and maintains its shape at the minor flow exit. There is, however, a small reduction of number density for particles with diameters less than $1.5\mu m$, which is attributed to major flow evacuation. Interestingly, this behavior is embellished in figures (b), (c), and (d), namely since the size distribution is preferentially deviated towards smaller diameters. What is so insightful in those particular plots is the unpredictable behavior of the sample at the collection stage. Precisely, the particles smaller than $1.5\mu m$ and larger than $\sim 1\mu m$ are experiencing "backflow" from the probe to the major flow. It is shown that a temporary increase in number density is achieved at the collection probe, which eventually is lost as indicated by the lower final number density at the minor flow outlet. A small band of those backward flowing particles are caused to collide with the probe walls (recall the wall loss peak of figure 2.17 which occurs for $d_p \sim 1.45\mu m$), while the smaller particles are able to escape back to the major flow. On the other end, particles larger than $2\mu m$ are not affected by the flow separation, and their distribution remains intact. To further analyze such newly discovered properties of the aerosol transport mechanism, we construct another narrow size-distribution but with a smaller mean diameter, shown in figure 2.20-a. The intermediate and final distributions are shown in figure 2.20-b, and it is distinctly visible that the backflow phenomenon associated with the temporary increase in number density at the probe is restricted to particles around $d_p \simeq 1.25\mu m$. In addition, it is observed that the final shape of the size-distribution is not altered significantly, compared to the minor flow distributions in figure 2.19-b-c-d.

The poly-disperse analysis initiated for this study, does not only help us understand the number density variation during virtual impaction and its influence on the

particle size separation, but can also be exploited to yield information about minor flow enrichment, which is relevant in studies aiming at concentrating dilute aerosols. Figure 2.21, shows the *scaled* number density, defined as the ratio of number of particles with a given size to the total number of particles in the distribution, as obtained from Lagrangian simulations on flow fields of case II, and III. The same initial size distribution is used in both calculations, as shown from the overlapping nozzle data points.

With respect to the reference nozzle sample, the role of the flow separation is seen to have two revolving effects on the minor flow enrichment, around a critical diameter equal to $1.2\mu m$. Depending on whether the particle is smaller or larger than this critical size, the virtual impaction foot print will either reduce or increase its density enrichment in the minor flow, respectively. Interpreting the intermediate samples at the probe is not as straightforward, since the data is more disorganized. Nonetheless, we can distinguish the particle sizes that are prone to experience back-flow, and loss as discussed earlier. Another important observation that can be learned from contrasting the distributions of case II and III, is that the higher jet velocity does not necessarily provide better enrichment across the board. For instance, as a result of the sharp enrichment of the critical diameter in case III, the final distribution becomes narrower for the relatively larger particles, and the particles whose size is greater than $\sim 1.4\mu m$ are more enriched in case II. Apparently, the imprint of the change in Reynolds number is closely tied to a narrow band of particles whose time scales are small enough to cope with the increasing velocity magnitude. The consequence, as demonstrated, is a more focused concentration. Lastly, the trailing part of the minor flow distribution warrants an explanation. Opposite to the trend below the critical diameter, where the collector enrichment is higher than that of the minor flow, due to the transitory overshoot of smaller particles, the final enrichment well beyond the critical diameter is not only higher than that at the nozzle, but also that

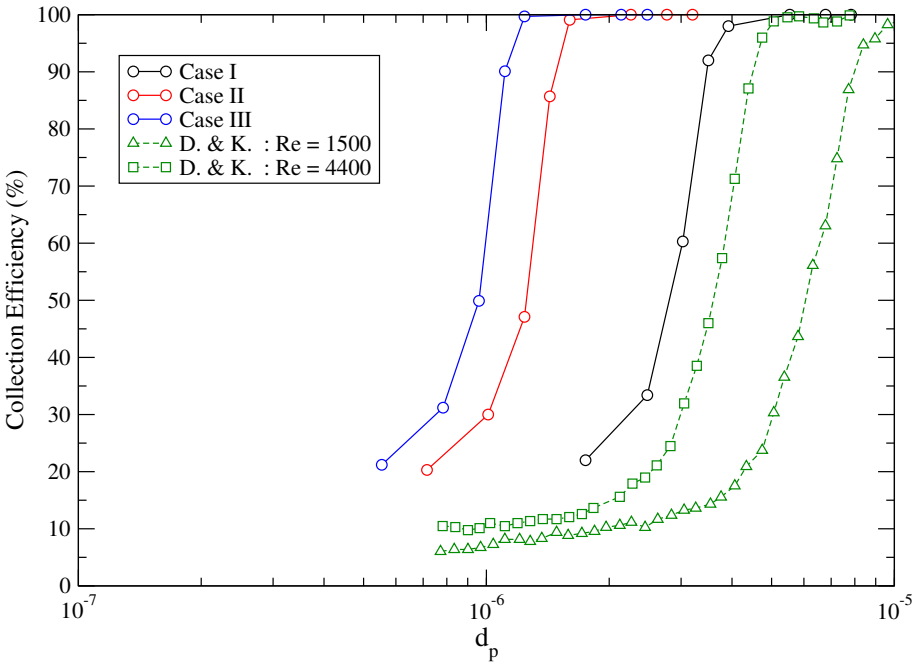

Figure 2.16: Mean separation efficiency as a function of particle diameter. Experimental data from [7]

at the collector. This behavior is indicative of the particle-removal effect at the probe walls. In the next section, after examining the transient fluid mechanical properties of the flow, the unsteady particle tracking results will be presented, and the aerosol size distribution will be revisited and discussed in light of its interplay with the coherent fluid structures.

2.4.3 Unsteady Flow

The advantage of a time dependent solution lies in the ability to monitor and study the evolution of unsteady flow phenomena. Historically, the most astounding insight into the nature of turbulent flows came from the analysis of key sequential events that dominate a particular flow. To the extent where this is applicable for the virtual impaction regimes under study, we present some time-variable results in order to gain an improved understanding of the role of the Reynolds number in this

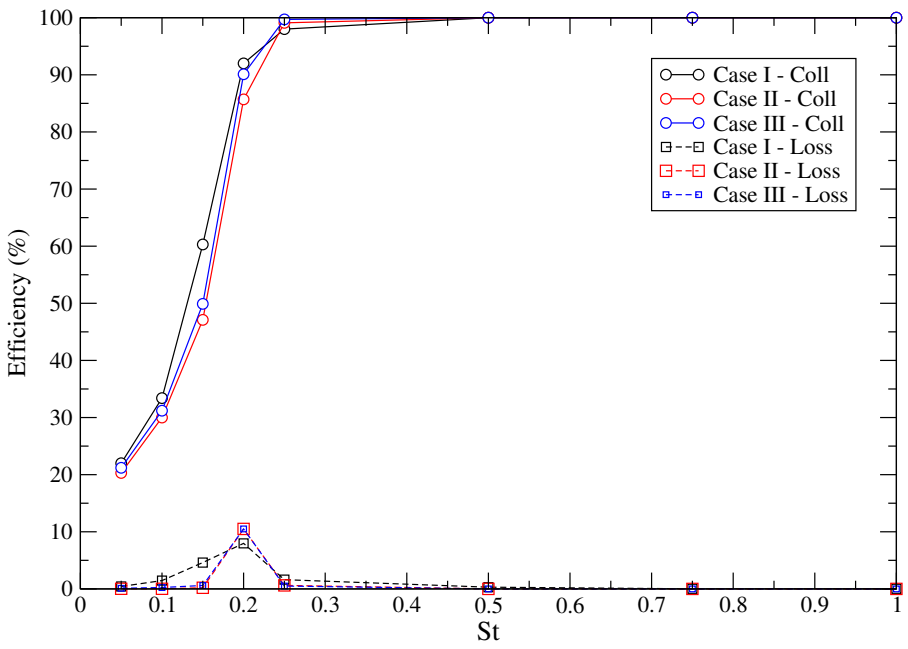

Figure 2.17: Mean separation efficiency and particle loss as a function of Stokes number

type of flow, and to decipher its underlying transport mechanics. A revealing piece of evidence concerning the transient nature of virtual impaction flows, which to the knowledge of the author has been undetected in prior investigations, is the record of the lift force exerted by the fluid on the *minor flow* walls. Recall that the minor flow duct constitutes the receiving end of the jet, thus it is predisposed to "feel" any disturbances generated during virtual impinging. Physically, this corresponds to inherent vibrations, and may explain the source of puzzling noises or "ringing" tones encountered in previous experiments [59]. Figures 2.22, 2.23, and 2.24 show the history of the dimensionless lift force or lift coefficient C_L defined as:

$$C_L = \frac{\text{lift force}}{\frac{1}{2}\rho(L_m \times 1)U_m^2} \tag{2.21}$$

where $L_m \equiv 8.04\ mm$ is the duct length, and U_m is a characteristic duct-entrance

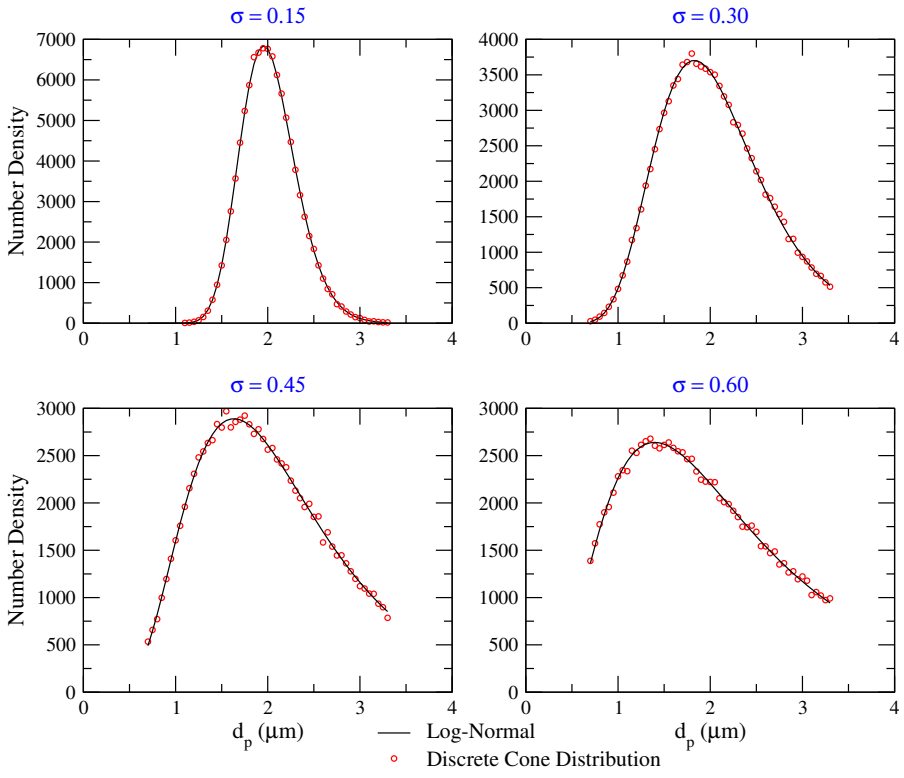

Figure 2.18: Initial poly-disperse aerosol distributions. 'Number Density' indicates the number of particles present in a given aerosol sample

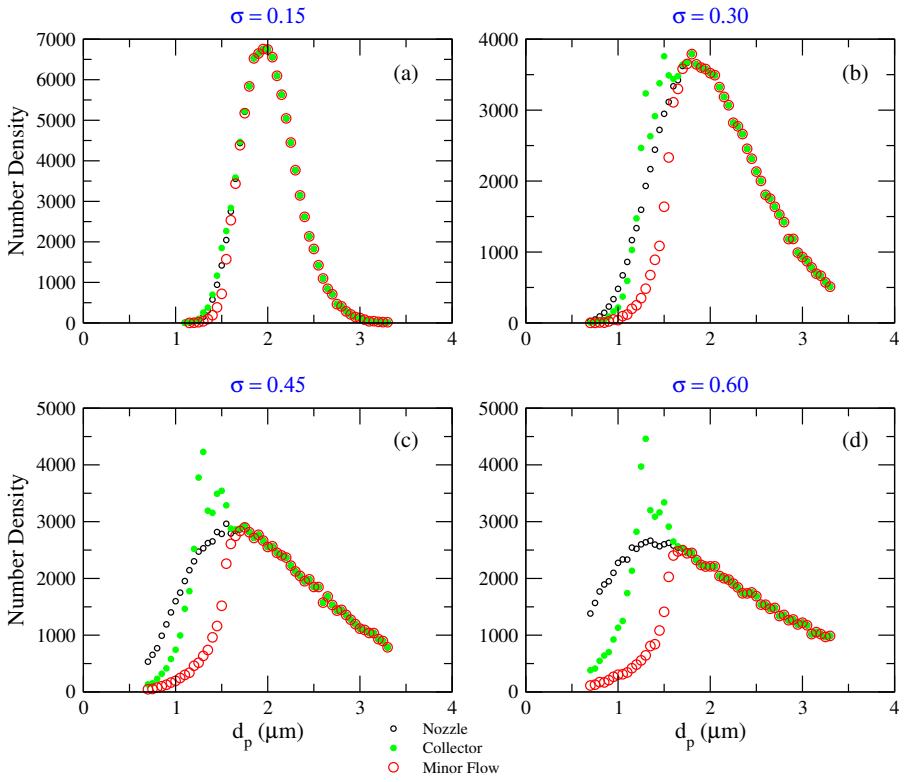

Figure 2.19: Sampled poly-disperse aerosol distributions - Case II

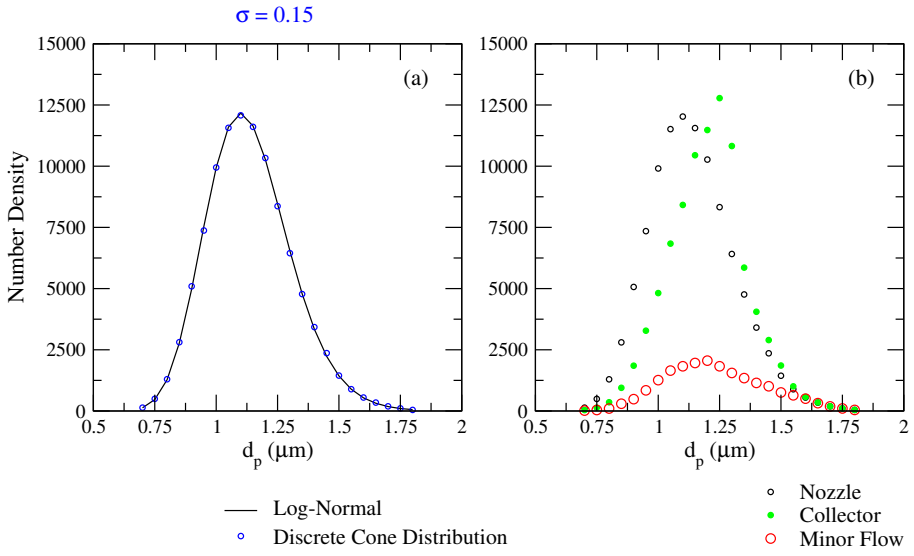

Figure 2.20: Initial & sampled poly-disperse aerosol distributions for $\sigma = 0.15$, and $d_m = 1.125\mu m$ - Case II

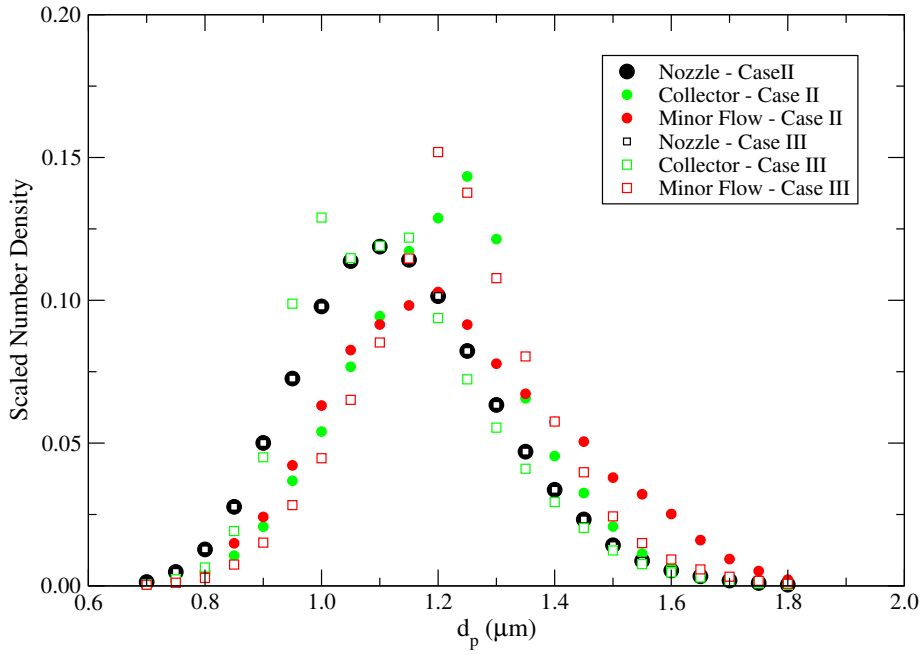

Figure 2.21: Enrichment of poly-disperse aerosol distributions - Cases II & III

velocity. The lift force is taken as the sum of the pressure and normal viscous stresses along the entire length L_m. The inserts in each figure indicate the window of statistics sampling outlined in Table 2.3. It is clear that in case I, the lift signal undergoes a smooth periodic cycle whereas the latter higher Re cases exhibit an immensely fluctuating signal. In all cases, however, we notice that during the startup time the signal is zero. It is well known that vorticity plays a major role in shaping the structure of a free jet. Its influence in each of the virtual impactor flow cases can be appreciated from figure 2.25 which shows the vorticity modulus, $|\Omega| \equiv |\nabla \times \mathbf{U}|$, averaged in time and scaled by $\Omega_o = U_j/0.5W$. The plots signify the extent of vorticity accumulation in the jet shear layers extended from the nozzle boundaries. We observe that the vorticity peaks at the first x-station downstream of the nozzle, and maintains the overall thickness of the shear layer all the way into the mid-gap location. The thickness, of course, diminishes as the Reynolds number is increased, thus, jeopardizing the stabil-

ity of the free-boundary layers. The unsteady evolution of such layers is monitored in figures 2.26 & 2.27 for case I and III, respectively. The time-series snapshots for the laminar case are taken after a significant amount of passage from startup (i.e. $t_1 >> t_0$). As can be seen, the structure of the shear layers extending from the jet walls into the virtual impaction zone does not change considerably, and the ability of the mixing layers to entrain surrounding fluid is deferred well into the major flow chamber, where a weak but large circulation region is formed. Similarly, the concentrated vorticity regions generated by the tearing action of the sharp collector-nozzle walls are convected to the major flow to form a mixing layer parallel to the original jet shear layer. The two layers then become synchronized in their motion as they undergo a meandering swing. This periodic oscillation, as we shall demonstrate later, is the cause of the quasi-periodic lift signal.

A completely different picture is drawn from the higher Reynolds number cases. Figure 2.27 shows a series of snapshots from the **early** development of the jet. The same behavior, not shown here, is also observed for case II. Unlike case I, the character of the virtual impaction region does not remain the same with the passage of time, and in order to understand the subsequent instantaneous stages of the flow field, we must first look at its origin. The vorticity dense layer migrates from the jet walls to form circumferentially coherent concentrations. The rapid growth and entrainment of the early vortices is coupled by a relatively mirrored process on the sharp edge side of the nozzle. Eventually, the shear layers stretch and detach from the newly formed vortices, and the cycle is repeated to produce a streak of alternating vortex shedding reminiscent of the Kelvin-Helmholtz instability [60]. The question that arises then is: what causes the lift signal to become profoundly disturbed or if possible turbulent? To answer this question we will prove that the behavior of the lift signal is correlated with the instability processes in the virtual impaction zone, which in their own right are worthy of understanding. Our diagnosis suggests that there is a nonlinear interaction

mechanism between two types of instabilities, namely a **jet-axis** mode and a **shear-layer** mode. The former is associated with jet "flapping" or "buckling", in other words, the sporadic swinging of the bulk jet column, which incidentally has also been reported for a transitional slot jet [26]. The latter mode is connected to the vortex activity described earlier. We shall attempt to clarify these statements with the help of some analytical tools.

The product of fluctuating signals at two separate points in the flow, also called "correlations", can lead to genuine insight about the interaction mechanisms of the flow. Before we perform this type of analysis, it pays to make some definitions. First, the instantaneous velocity signal, for example, is decomposed into a time average and a fluctuating component. The same is done for pressure and lift:

$$\begin{aligned} U_x = U_x^{avg} + u \;\; ; \;\; U_y = U_y^{avg} + v \\ P = P^{avg} + p \;\; ; \;\; C_L = C_L^{avg} + l \end{aligned} \tag{2.22}$$

The aim is to compute the two-point correlation between the primitive fluctuating variables (u, v, p) at several points in the flow and the reference lift signal, in order to infer the nature of the agitating flow events. The correlation coefficient is defined by [61]:

$$\sigma_{ab}^{*} = \frac{\frac{1}{N_t}\sum_{j=1}^{N_t}(a_j - a^{avg})(b_j - b^{avg})}{\sigma_a \sigma_b} \tag{2.23}$$

where (a,b) are the two random variables being correlated, and (σ_a,σ_b) are the corresponding standard deviations. We shall limit the discussion to the data of case III, given its perceived turbulent conditions. Notwithstanding, the same analysis when applied to case II data yielded very similar results. We begin by sampling the flow

field from $x^* = 0$ (jet nozzle) to $x^* = 1$ (collector nozzle). The two meaningful y-positions are the jet axis ($y^* = 0$), and shear layer axis ($y^* = -0.5$). An example of the fluctuating velocity and pressure signals at the centerline in the middle of the collector nozzle ($x^* = 1, y^* = 0$) is shown in figure 2.28. The two-point correlation function is depicted in figure 2.29 for the two distinguished instability modes. First, It appears that the role of the velocity oscillations surpasses that of the pressure given the higher contribution that the velocity components produce in the correlation. Furthermore, the change in the functional form of the correlation between the jet axis and the shear layer is suggestive of a different evolutionary mechanism that resonates its impact on the walls of the collection probe, specifically, the affinity for uni-modal versus bi-modal distribution. The latter (see figure 2.29-b), we believe, is a consequence of the dissociation of the boundary layers to form roller-type vortices. The fact that the *ul* and *vl* correlations in the shear layer produce a bimodal function that passes through the zero axis, can be understood as the passage of intermittent coherent structures that are detected at two locations along the shear layer axis, namely at the minimum ($x^* \approx 0.39$) and maximum ($x^* \approx 0.63$) of the *ul* correlation.

The correlations are best interpreted with a physical picture in mind. In figure 2.30-a we show a frozen snapshot of the vorticity field, after a sufficient passage of time, that establishes the creation of a shear layer eddy on the lower nozzle side. Figure 2.30-b depicts the velocity magnitude at the same instant of time. As can be seen, the size of the eddy roughly spans the same x^* range where the correlation peaks are conspicuous. The earlier peak position, therefore, must mark the onset of separation associated with slowly moving fluid (negative *ul* correlation), while the proceeding one reflects the faster edge of the eddy undergoing strong deformation and acceleration (positive correlation). By the same token, the *vl* correlation peaks, which approximately appear at the same x^* locations as the *ul* correlation but with an *opposite* sign, indicate that as the eddy is being detached from the shear layer

it is lifted laterally, thus causing an increase in the cross-stream velocity (positive vl correlation), whereas at the opposite end downstream, the eddy is experiencing deflection and strain. A closer examination of the transverse velocity contours of figure 2.30-c at that same moment reveals the presence of a thin film of null y-velocity separating the ejecting jet on the right hand side of the eddy, and the upward traveling fluid on the left hand side, which gives rise to a maximum negative vl correlation. On the other hand, the jet-axis instability (see figure 2.29-a) produces its biggest contribution at the end of the potential core ($x^* \approx 0.5$) judging by the appearance of a local minimum in the ul correlation, which marks the instances where the jet penetration is challenged causing a deceleration in the streamwise direction relative to the mean flow. The bimodal vl correlation on the jet axis can be viewed as a consequence of the sinusoidal form of the instantaneous y-velocity due to the alternating motion of the jet column. It is important to note that such nonlinear interactions are not smoothed out by time-averaging.

To further understand the dynamics of the instabilities and to quantify their effects, we shall examine the spectral content of the time signals. The Fourier transform of a function $f(t)$ is defined as:

$$g(\omega) = \frac{1}{2\pi} \int_{-\infty}^{\infty} f(t) e^{-iwt} dt, \tag{2.24}$$

where $g(\omega)$ is the transform function in the frequency domain (ω). Clearly, due to the finite amount of time-data available, a discrete analogue of the above integral is computed. The frequency characteristics of the v signal are first examined. Figure 2.31 is a comparison of the Fourier transform of the lateral velocity sampled on the jet, as well as shear layer axis, in the virtual impaction gap for case II and III. Evidently, the spectral distribution on the jet axis is limited in the number of spikes, with a fundamental frequency $f_d \approx 13$ & 9 KHz for case II and III, respectively. The shear layer axis instability, in turn, shows remnants of flapping frequencies with

higher amplitudes, and also other secondary frequencies which can not but belong to a broad set of physical interactions rather than one repetitive event. It is interesting to note, that the lower Re case undergoing 'transition' exhibits a rather distinct gross amplitude shear layer event corresponding to a frequency of $\sim$ 24 KHz at which a complementary smaller spike exists in the jet axis signal. The growth of multiple harmonics in the frequency domain substantiates the outlook that the livelihood of the free shear-layer instability in the virtual impactor is not completely due to the origination of vortex shedding, or detachment of concentrated vorticity filaments. The geometrical considerations, in fact, institute a medium favorable for feedback propagation and other more complex interactions. Support for this argument can be drawn from the identification of a string of events that nurture upstream feedback. One such driver relates to the impinging shear layers on the major flow boundaries which interact with the vorticity rich layers near the walls in order to breed new incarnations of eddies that are able to stream with the large-scale circulations in the major flow chambers, and find their way back to the impaction gap. Other phenomena such as vortex coalescence and re-orientation engage to distort the basic structure of the free boundary layers.

The Fourier transform analysis can also be invoked to study the one-dimensional energy spectrum $E_{11}(\omega)$, which is obtained from the transform of the time autocorrelation coefficient, defined as [45]:

$$R_E(\tau) = \frac{\overline{u(t)u(t+\tau)}}{\overline{u^2}(t)}. \tag{2.25}$$

An indicative behavior of $R_E(\tau)$ for the free shear layer in the virtual impaction gap $(x^* = 0.5, y^* = -0.5)$ is given by figure 2.32. The autocorrelation coefficient is computed for the fluctuating vorticity, as well as the two components of velocity. The time axis is normalized by the relevant virtual impaction time τ_{vi}. It is interesting to observe that within one throughput time unit, the transverse velocity autocorrela-

tion with its quasi-periodic features decays at a faster rate than the longitudinal one suggesting a more active role for the u-velocity component. Moreover, the fact that the vorticity and longitudinal velocity autocorrelations remain positive suggests that within the relatively steady correlation value, the sustainability of the shear layer is maintained. At longer time scales (not shown in the plot), however, the autocorrelation coefficient becomes zero and begins to exhibit periodic oscillations due to the reorganization of the elongated shear layer into coherent eddies. As far as the spectrum is concerned, it is computed at the shear layer position referred to earlier, as well as the mid-jet-axis location. Hence, the two instability modes are vindicated by figure 2.33 which clearly establishes the spectral content of u-velocity fluctuations on the jet, and shear layer axis. The frequency domain is non-dimensionalized by the Strouhal number $St_h \equiv \omega\delta/U_{oo}$. It is shown that there is indeed a cascade of energy from long to short wavelengths. In addition, we can deduce that the higher spectral content of the shear layer instability must be associated with higher frequency harmonics, as alluded to in figure 2.31.

One remaining analytical tool that can enhance the comprehension of the turbulence activity during virtual impaction and its shear layer dynamics is the "quadrant analysis" technique first used by Wallace *et al.* [62] for the study of wall region events in a turbulent channel flow. Recall that the Reynolds shear stress is $-\rho\overline{uv}$, and understanding its behavior is key to realizing the role of the fluctuating velocity field in transferring momentum. The categorizing process consists of classifying and averaging the instantaneous product signal uv based on the sign of the individual components. Table 2.5 below identifies the four constitutive groups of interest:
The u and v time signals are sampled from several y-stations spanning the *lower* nozzle free-shear layer at the mid gap location ($x^* = 0.5$), and then processed to detect the instances where the velocity components contribute to each quadrant. The classified signals, designated by $\overline{uv}_c$, are then averaged and normalized by the

Quadrant	u	v	flow event
Q1	+	+	'fast upward'
Q2	-	+	'slow upward'
Q3	-	-	'slow downward'
Q4	+	-	'fast downward'

Table 2.5: Types of classified Reynolds stresses

net stress $\overline{uv}$, and plotted in figure 2.34. Note that the sum of data points from all quadrants at each y-station amounts to unity. The results of figure 2.34 indicate that the highest activity causing the production of Reynolds stress occurs in the naturally perturbed free-boundary layer beyond the jet bottom plate, i.e. $y^* < -0.5$. There is however a significant level of $Q2$ contribution within the jet itself ($y^* = -0.4$), which is most likely an outcome of the separation events associated with the formation of coherent eddies that experience clock-wise roll-up from the shear layer into the jet column. As we move deeper or downwards into the shear layer, $Q1$ and $Q4$ types of events dominate, with the latter taking the lead. $Q4$ mechanics suggest that the eddies are composed of fluid traveling faster than the mean in both the axial and transverse direction. This is reasonable since we have confirmed from transient flow visualizations that the angle of vortex shedding is in fact inclined with respect to the horizontal axis.

As for the two negative contributors, $Q1$ & $Q3$, they appear to play equal roles slightly above and below the jet outer boundary, pointing towards one mechanism at the mixing layer interface, where the interactions are coupled between the accelerated regions on the jet side and the decelerated regions on the chamber side. Further below the sheared interface, $Q1$ mechanisms take over which represents interactions of high speed fluid being pushed upwards towards the nozzle. One possible physical explanation for this property stems from the ability of the deformed eddies to fling the fluid around its fast peripheral entity. Undoubtedly, it is perceivable that all of these events are occurring simultaneously so that this analysis can only reconstruct

some of the simplified dynamics based on one-point statistics. Nonetheless, from this insight we are capable of exposing the balance of the different forces coming into play, thus allowing us to ascertain the dominant inter-relationships of this complex flow.

With that in mind, we move now to contrast some of that physics with the results of case I and II. The level of streamwise fluctuations, as we have seen, is crucial in dictating the dynamics of the free shear layers. Figures 2.35 and 2.36 depict the root mean square velocity U_x^{rms} at the representative y-stations for the flow fields of case I and II, respectively. The results of case III are similar to that of case II, so the following comparison will discuss the differences between the laminar and non-laminar regimes. First, to give a proper relative perspective as to the intensity of the fluctuations, the r.m.s. velocity is scaled by the jet centerline velocity U_{oo}. As shown, the intensity of the perturbations in the laminar case is $\approx 4\%$ of the mean velocity, which is accumulated exclusively near the jet exit plane. Because of the stability of the jet shear layers the oscillations are weak in nature, and their effect is localized to the immediate region outside the nozzle, where they begin to gradually grow as the layers expand laterally. A completely discrepant image is observed for the non-laminar cases. First, the intensity of fluctuations reaches a staggering 20% value relative to the mean velocity, and this increased strength is more or less sustained across the width of the shear layer. At the final two y-stations, there exists a dip or saddle point near the mid gap location, which is indicative of the intermittent nature of the flow within the eddy formation region. It is interesting to note that the main activity is centered around $x^* = 0.5$ which is where most of the previous analysis was conducted. As we move further downstream into the collection probe, the fluctuation levels decay at an equivalent rate regardless of the y-location which supports the argument concerning the re-laminarization of the flow. Lastly, in figure 2.37 we present the overall shear stress $\overline{uv}$ computed using the flow fields of case II. The normalized shear stress is plotted at consecutive x-stations within the virtual impaction gap. As evidenced in

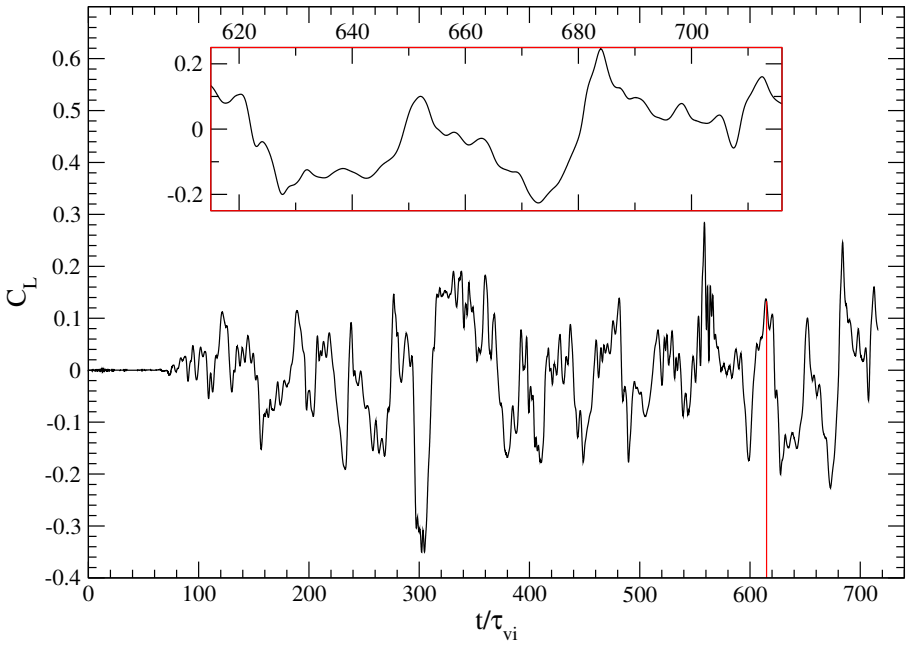

Figure 2.22: Lift coefficient on minor flow walls - Case I. Insert window shows zoomed view from red line to end time

the graph, the transfer of momentum by the fluctuating field is concentrated in the jet mixing layer, and is augmented with axial distance. The peak again occurs at the midpoint and begins to shift laterally away from the nozzle walls due to the deflection and extraction of the impinging vorticity layers. This plot, in fact, complements the discussion pertaining to the results of figure 2.34 since it provides an overall picture of the total Reynolds shear stress behavior.

2.4.4 Particle-Eddy Interaction

In the previous section we examined the unsteady features of the flow in the virtual impactor jet and characterized the nature of the two-dimensional coherent structures originating from the jet mixing layers. The next logical endeavor, of course, is to investigate the influence of such transient and chaotic phenomena on the transport of aerosol particles. We shall utilize the transient flow fields of case II, since

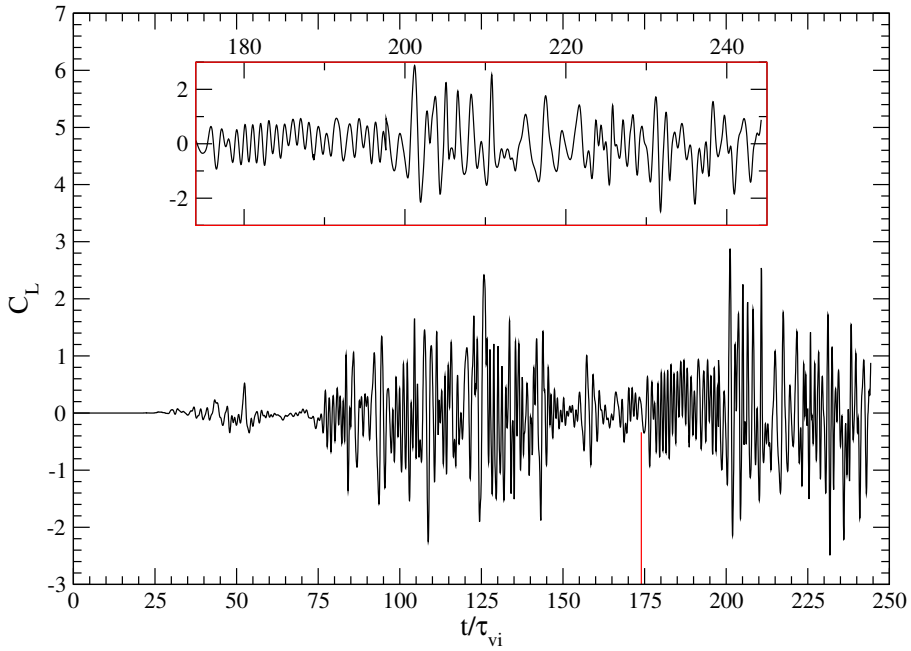

Figure 2.23: Lift coefficient on minor flow walls - Case II. Insert window shows zoomed view from red line to end time

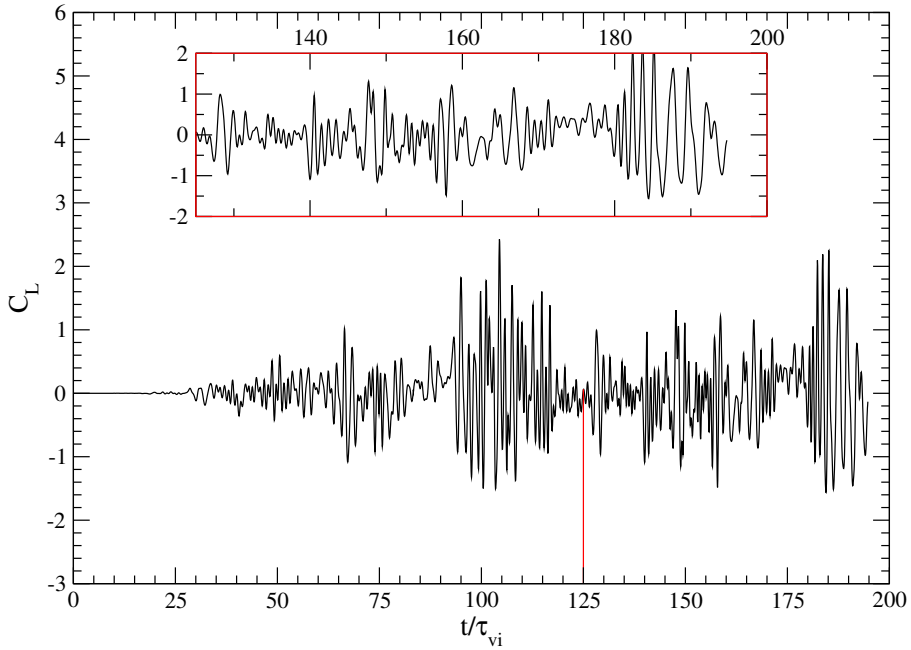

Figure 2.24: Lift coefficient on minor flow walls - Case III. Insert window shows zoomed view from red line to end time

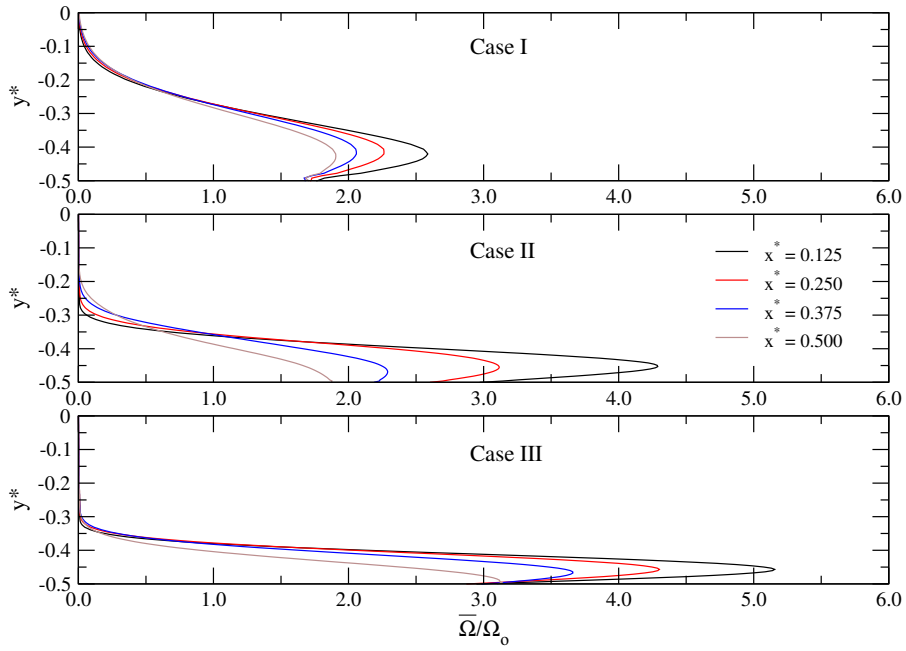

Figure 2.25: Jet shear layer mean vorticity (bottom nozzle side)

it possesses the unsteady flow structures of a high Reynolds number flow, and it forms the basis for the three-dimensional study. The solid particle diameters, for this particular analysis, are chosen such that they cover three Stokes number values. In addition, the time scale of the jet and shear layer fluctuations, τ_λ, was used to calculate another scaling parameter similar to the Stokes number. The flow microscale τ_λ is marked by the point on the time axis of figure 2.38 where the *jet axis* cross-stream autocorrelation coefficient first intersects the zero-axis. It was also found, that the period during which the *shear layer* cross-stream autocorrelation coefficient changes sign also corresponds to τ_λ. In essence, we wish to examine the ability of the particles to respond to flow events attuned to this axiomatic time unit. It turns out, the two dimensionless time units are not very different as shown in Table 2.6.

A definitive insight is gained from figure 2.39 which shows a contrast between the behavior of massless fluid particles and the $1.01\mu m$ massed particles. The particles

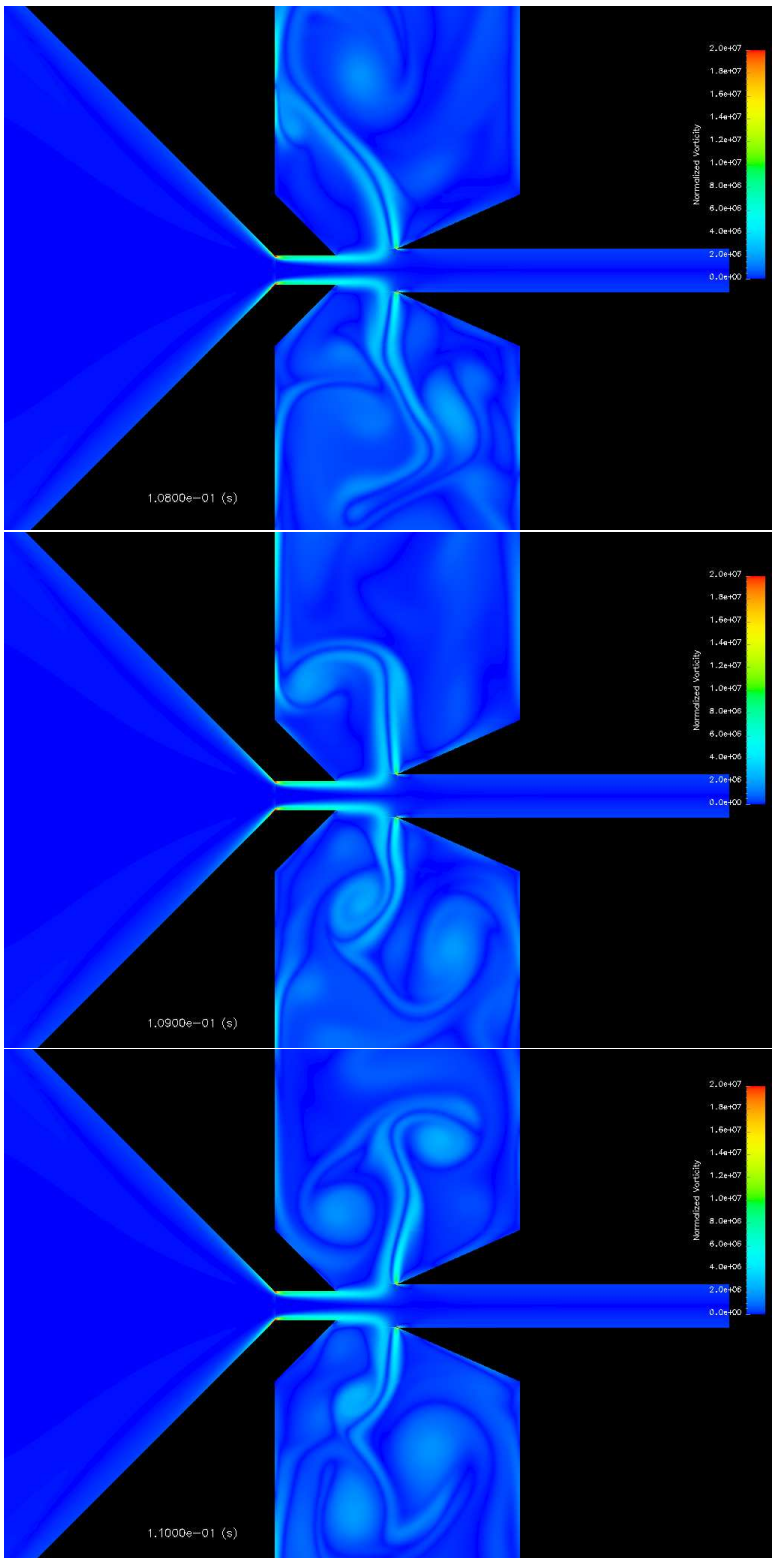

Figure 2.26: Evolution of concentrated vorticity layers in the virtual impactor at $t = t_1$, $t_1 + 100\Delta t$, & $t_1 + 200\Delta t$ - Case I

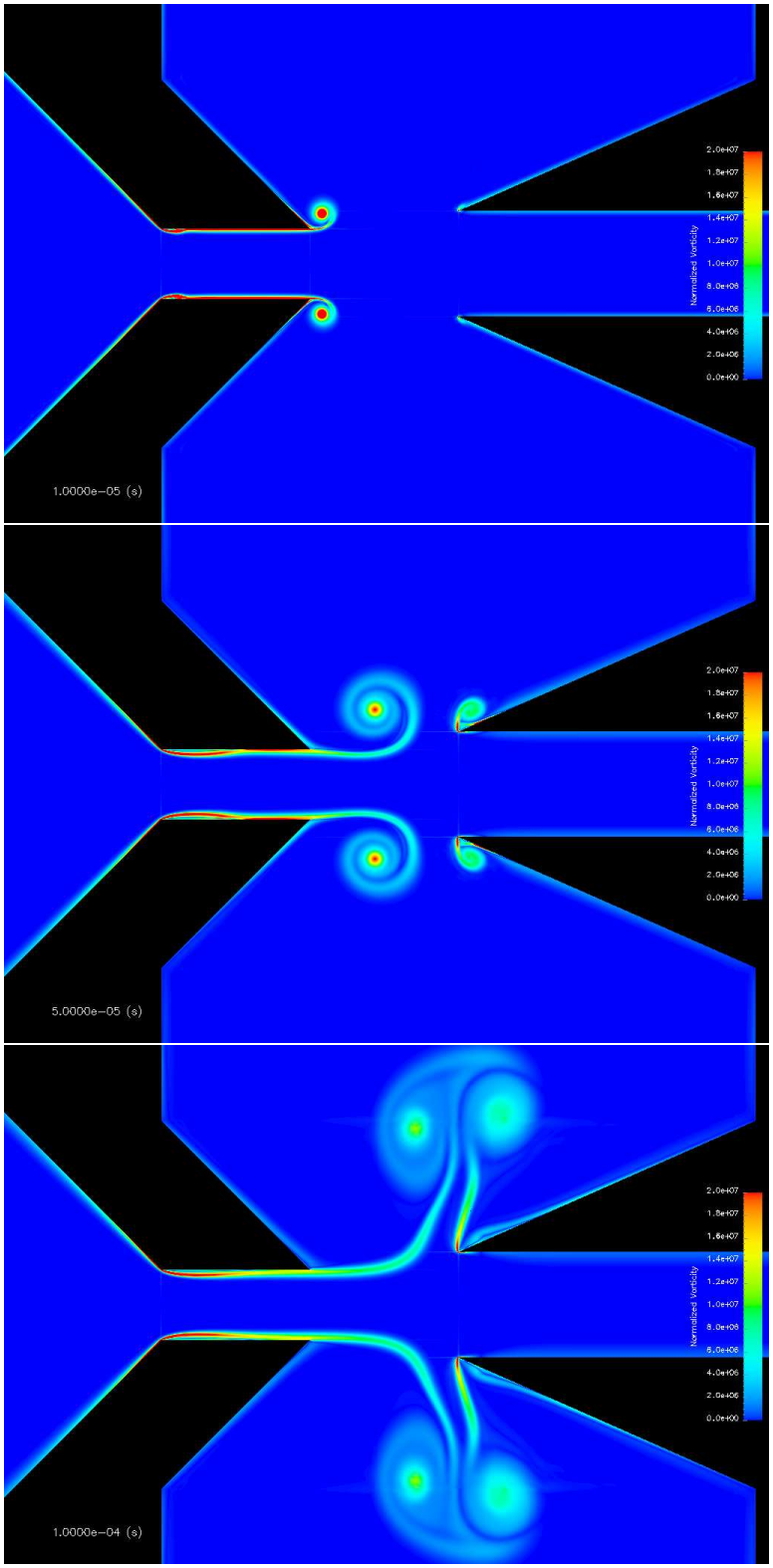

Figure 2.27: Evolution **from rest** of concentrated vorticity layers in the virtual impactor at $t = t_0 + 10\Delta t$, $t_0 + 50\Delta t$, & $t_0 + 100\Delta t$ - Case III, showing creation of coherent eddies

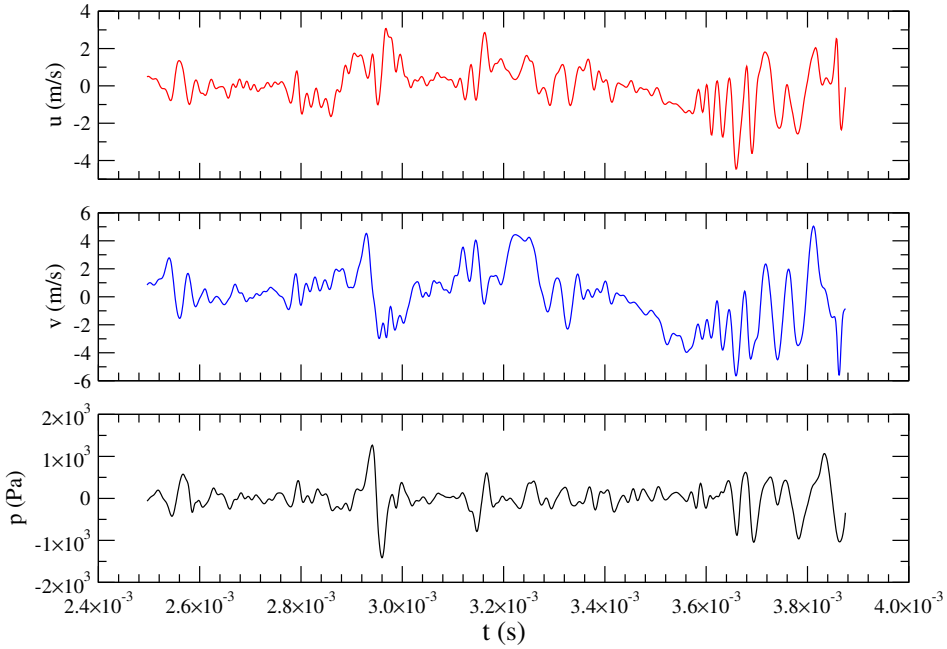

Figure 2.28: Fluctuating signals for velocity and pressure at collector center point $(x^* = 1, y^* = 0)$ - Case III

$d_p\ (\mu m)$	$\rho_p\ (kg/m^3)$	$\tau_p\ (s)$	$St \equiv \tau_p/\tau_{vi}$	τ_p/τ_λ
1.01	1047	$3.3e^{-06}$	0.10	0.19
1.60	1047	$8.3e^{-06}$	0.25	0.46
3.20	1047	$3.3e^{-05}$	1.00	1.85

Table 2.6: Dimensionless time scales for solid particles released in the jet boundary layer of Case II

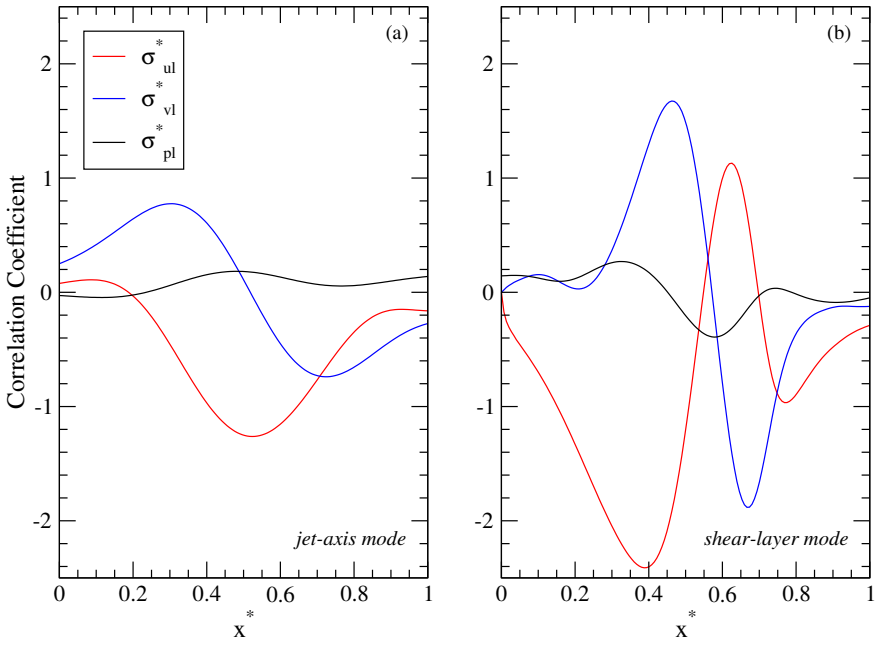

Figure 2.29: Two-point correlation between the primitive variables and the lift signal - Case III

are released in the throat boundary layer and color coded based on vertical distance from the wall. Three "tagged" layers are emphasized due to their distinct physical behavior in the virtual impactor. The first innermost layer extends $\approx 0.2W$ above the throat surface, whereas the middle and outermost rows are each $\approx 0.15W$ thick. The fluid elements, as shown in 2.39-a, are undergoing a severe deformation, mixing, and rotary arranging in a manner consistent with the Kelvin-Helmholtz instability. Figure 2.39-b shows the disposition of the finite-size particles at the same moment in order to elucidate the interaction mechanism with the aforementioned fluid structures. It is clear that the role of the free boundary layers has now changed. The aerosols traveling within the innermost layer will tend to cluster in the regions of low vorticity, specifically in the thin regions separating the roller vortices. Some of the dense finite-inertia particles, it appears, are capable of maneuvering away from the curved streamlines with very limited circulation around the well defined roller units, while

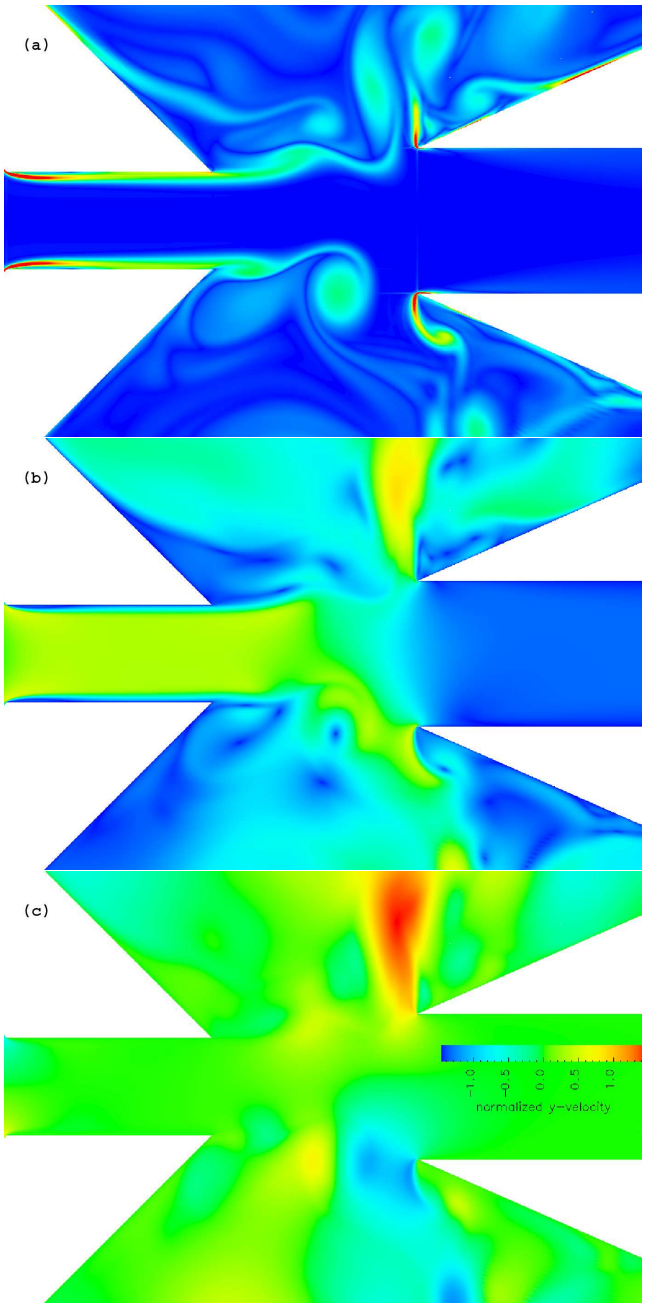

Figure 2.30: (a) frozen snapshot of vorticity field, (b) frozen snapshot of velocity field, showing eddy detachment, (c) thin film interface from y-velocity contours: Case II - all at the same instant of time

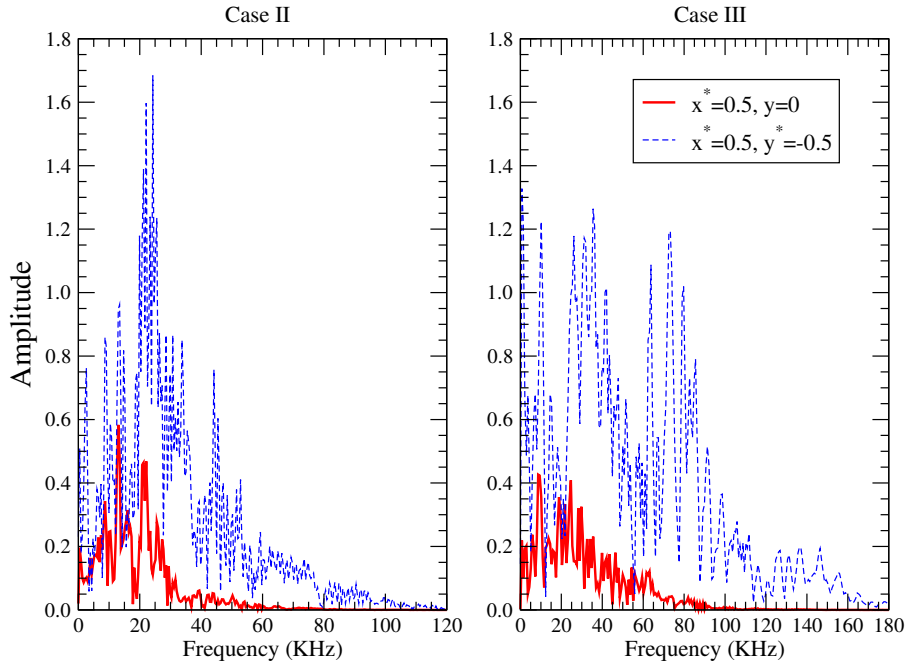

Figure 2.31: Fourier transform of cross-stream velocity signal

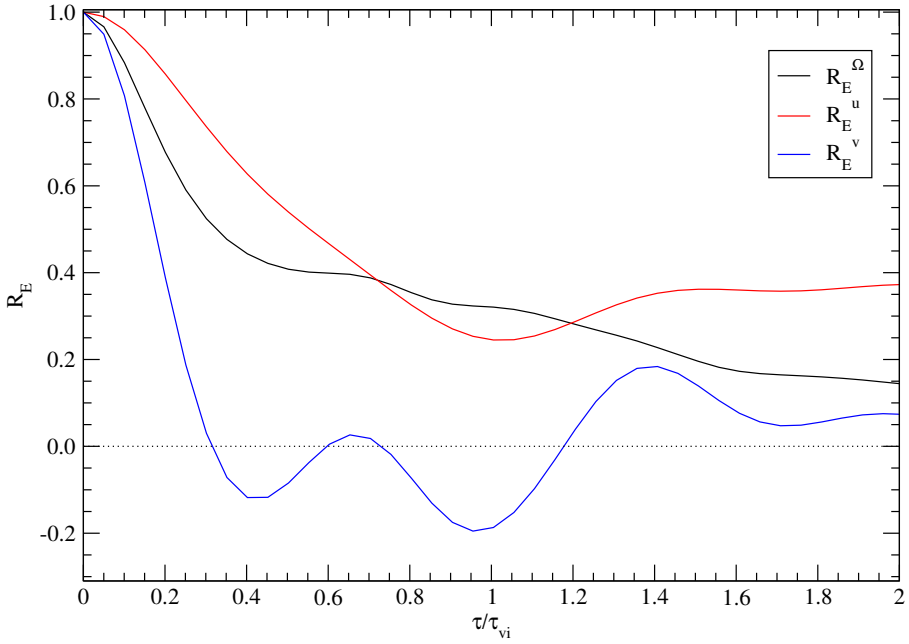

Figure 2.32: Auto-Correlation of vorticity, streamwise, and cross-stream fluctuations in the jet shear layer - Case III

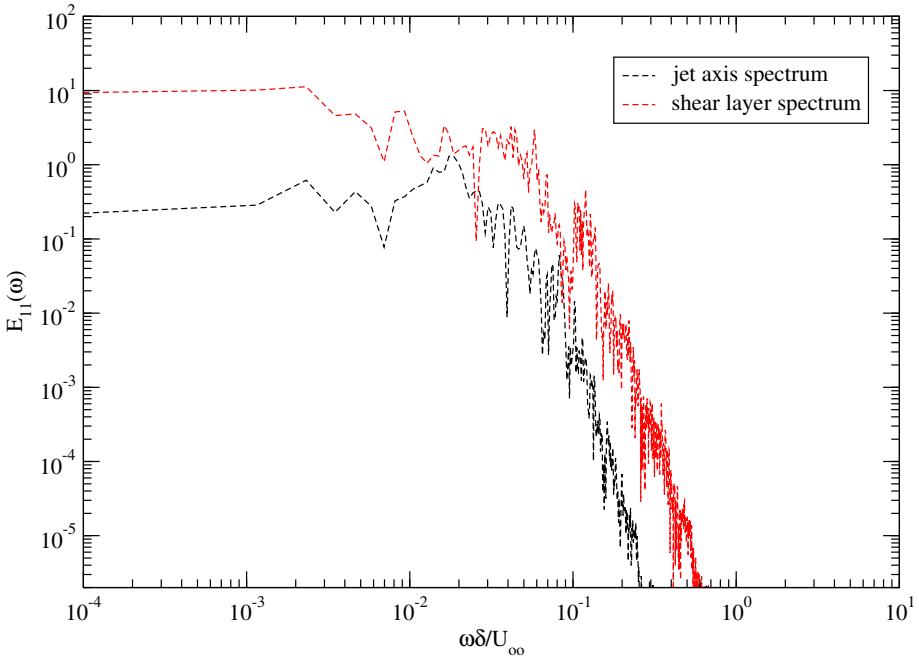

Figure 2.33: Fourier transform of streamwise velocity autocovariance - Case III

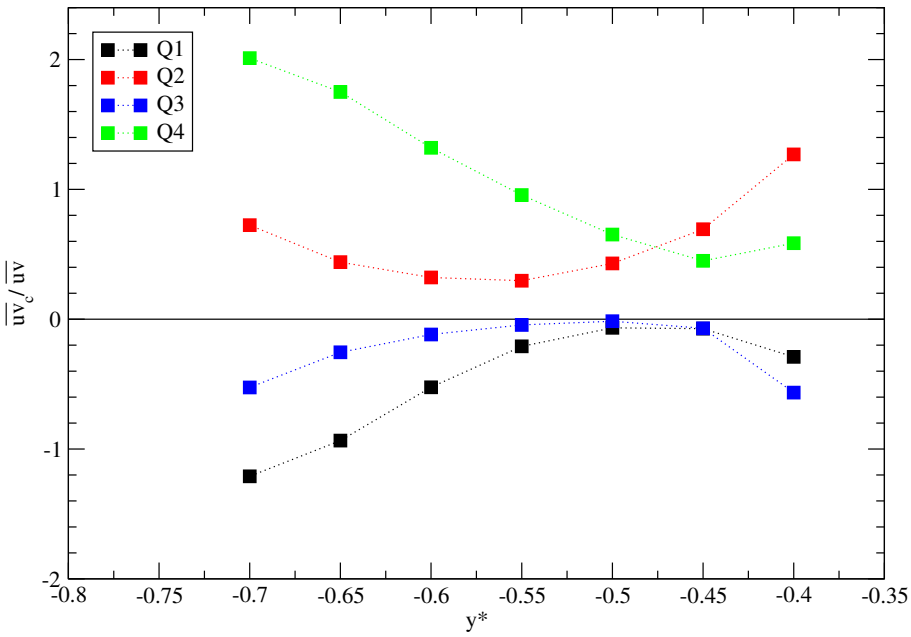

Figure 2.34: Classified Reynolds stresses in virtual impaction jet - Case III

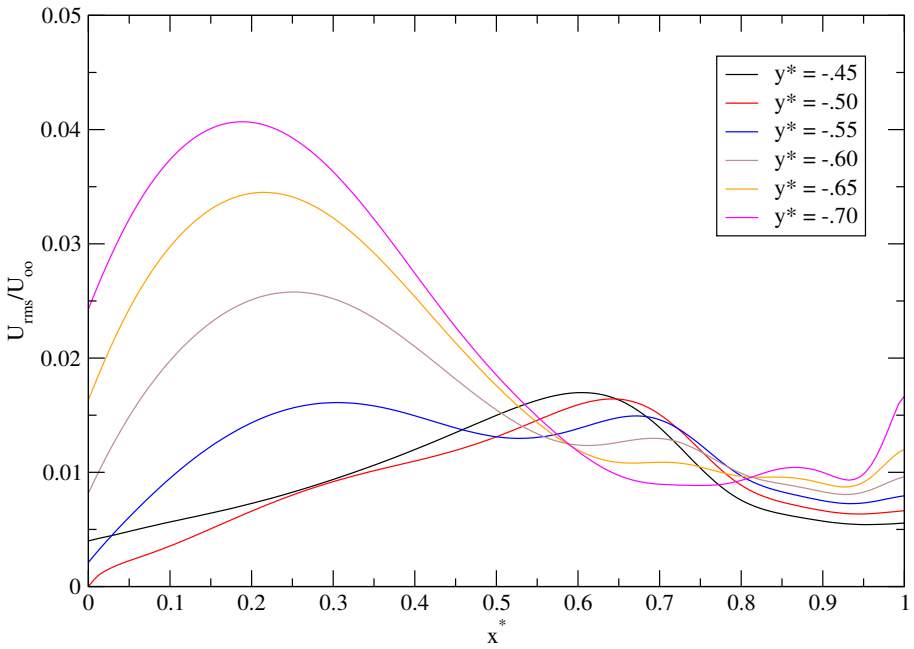

Figure 2.35: Jet shear layer root mean square axial velocity - Case I

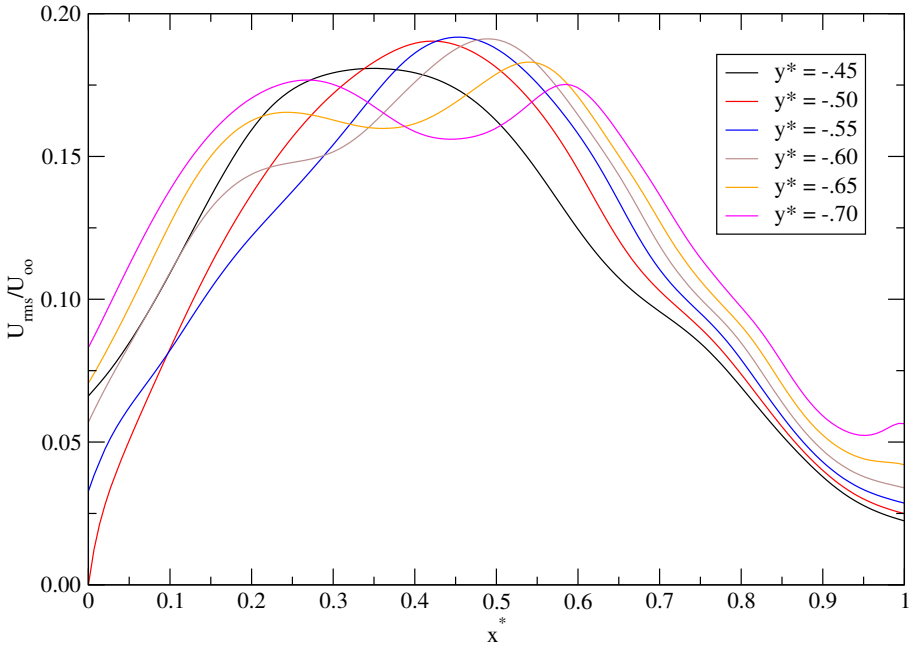

Figure 2.36: Jet shear layer root mean square axial velocity - Case II

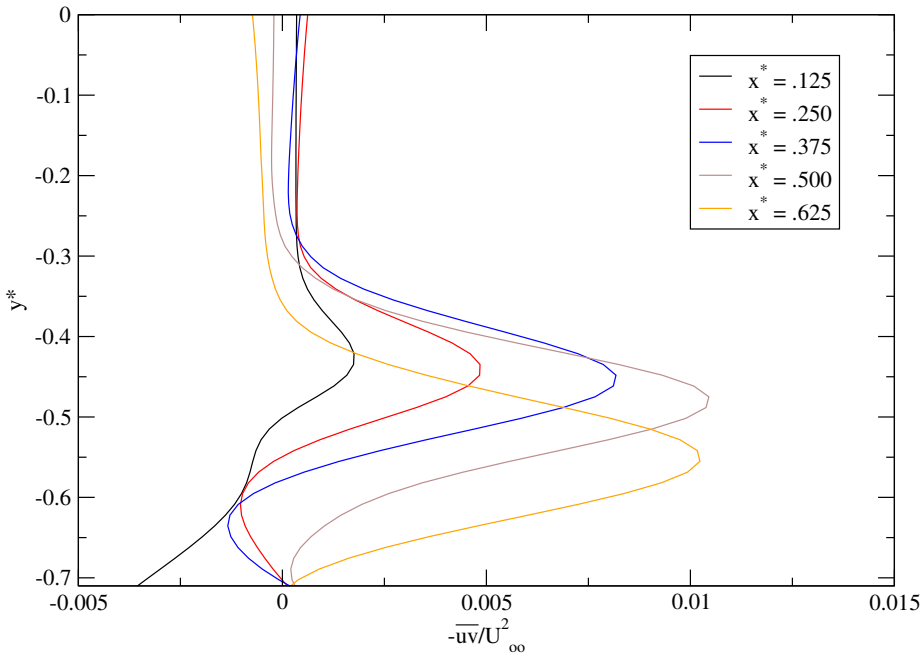

Figure 2.37: Virtual impaction jet shear stress - Case II

others are flung away from the vortex cores. Such phenomenon is also true for the slightly larger particles ($d_p = 1.60\mu m$) that are encountered in the major flow (see figure 2.40). The median throat outer layer, whose fluid points showed an incapacity to penetrate into the minor flow, is now beginning to reach the collection probe, however, some of its particles are escaping in the form of a leakage flow. The motion of particles whose Stokes number is of the order of unity, is shown in figure 2.41-b. Note that figure 2.39 is extracted from the first time window, while figures 2.40 and 2.41 are taken from the second time window.

As can be seen, the particles are too heavy to interact with the curved jet, whose local rollup behavior is shown in the same figure at the same instant. As a result, the boundary layer $St \equiv 1$ particles are deposited on the side walls of the probe, while the bulk particles are aggregated in the minor flow. Another fundamental aspect relates to the level of dispersion of the particles traveling along the jet core. Qualitatively,

the particles that cross into the minor flow channel are indeed expanding in a peculiar fashion. This "selective clustering" behavior is enhanced for particles with a slightly larger diameter than the one micron particles, as shown in figure 2.40-a. The wave-front-like particle clusters being formed in the minor flow duct are an outcome of the oscillatory response to the jet swinging motion. Their time scale τ_p/τ_λ is ≈ 0.5. Similar behavior is also found for the biggest particles ($d_p = 3.20\mu m$). To quantify the dispersion characteristics, we compute the dispersion function defined as:

$$\overline{Y}_T = \left(\frac{1}{N_p} \sum_{i=1}^{N_p} (Y_i(t) - Y_m(t))^2 \right)^{1/2} \tag{2.26}$$

where $Y_i(t)$ designates the lateral displacement of each particle from the jet center-line, and $Y_m(t)$ is the corresponding mean at time t. A similar *conditioned* function $\overline{Y}_c$ is computed on the fraction of the total number of particles that are accumulated in the **minor flow** duct in order to quantify their dispersion as well. Figure 2.42 shows the dispersion functions with respect to time for the particles summarized in Table 2.6. We conduct the calculations over $9\tau_{vi}$ units within two non-overlapping time windows. Our aim is to demonstrate that the virtual impaction jet as it goes through cycles of "bursting" events alters the dispersion properties of the particles. It can also affect the number concentration as shown in figure 2.43. Particularly, when we examine the unsteadiness of the virtual impaction vortex shedding cycle during the first time frame, we notice that it is *relatively* quiescent with very little feedback interaction. On the other hand, the results sampled during the second time window exhibit disrupting events, manifested as upstream traveling shear layers depicted in figure 2.40-b, that cause a startling change in the dispersion and concentration of minor flow particles (compare figures 2.42:c-d & 2.43:a-b). It can be seen, for instance, that those exasperated moments lead to a temporary but tremendous increase in the number concentration (i.e. percentage of probed particles) in the minor flow, which for longer times begin to settle to a constant value. Again, this is particularly true for

the particles with small Stokes numbers (i.e. $St < 1.0$). The overall functions of figures 2.42:a-b, indicate that the small particles ($St = 0.1$) in the **major flow** disperse in a manner similar to the massless fluid elements, if not more. The particles whose Stokes number is somewhat intermediate, $St = 0.25$, are capable of playing a dual role. In addition to accumulating in the minor flow duct, and undergoing "patterned" dispersion, they can also propagate to the major flow chambers and cluster between the roller vortices as shown in figure 2.40-a, and as confirmed by the rise of the corresponding dispersion function $\overline{Y}_T$. Finally, we utilize the time windowing calculations to compute a statistical particle propagation to the minor flow, and compare such results with the previous approach of mean flow particle tracking. The plots shown in figure 2.44 depict the comparison among the aforementioned approaches. As can be seen, the two methods give very similar outcomes for smaller particles ($St < 0.20$). The scattering activity described earlier for medium to large Stokes number particles, it seems, prevent the particles whose St lies between 0.20 and 1.00 to accumulate as high as predicted by the mean tracking calculations.

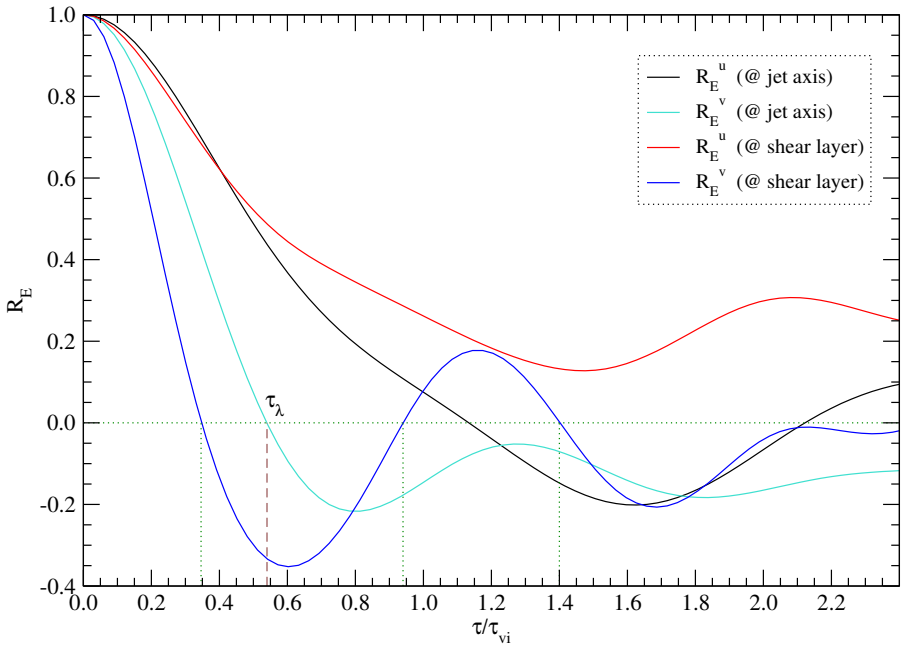

Figure 2.38: Auto-Correlation of u & v velocity signals on the jet axis and shear layer - Case II

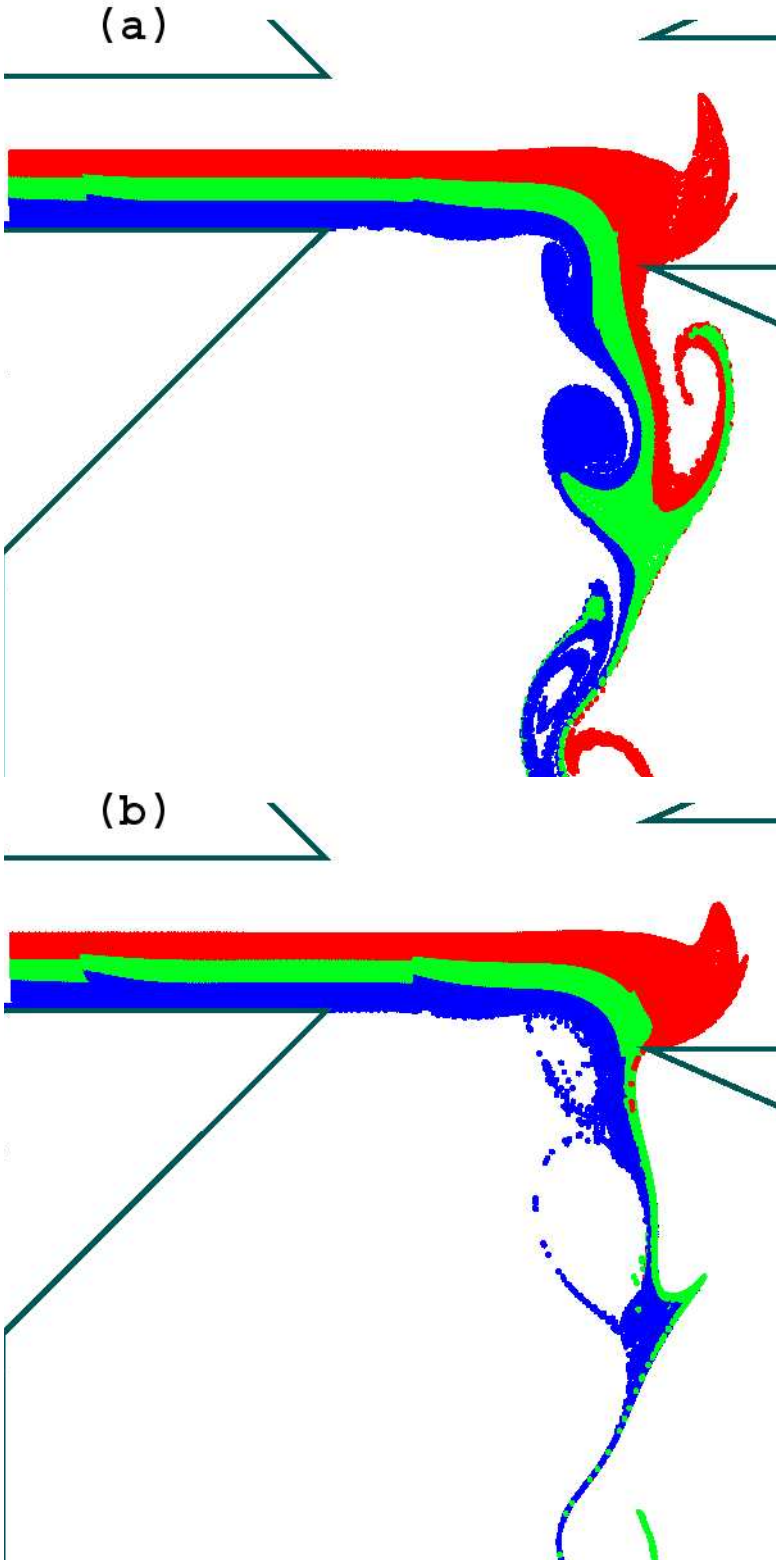

Figure 2.39: (a) massless particles, (b) solid particles with $d_p = 1.01\mu m$ ($St = 0.10$): Case II instantaneous still no. 1

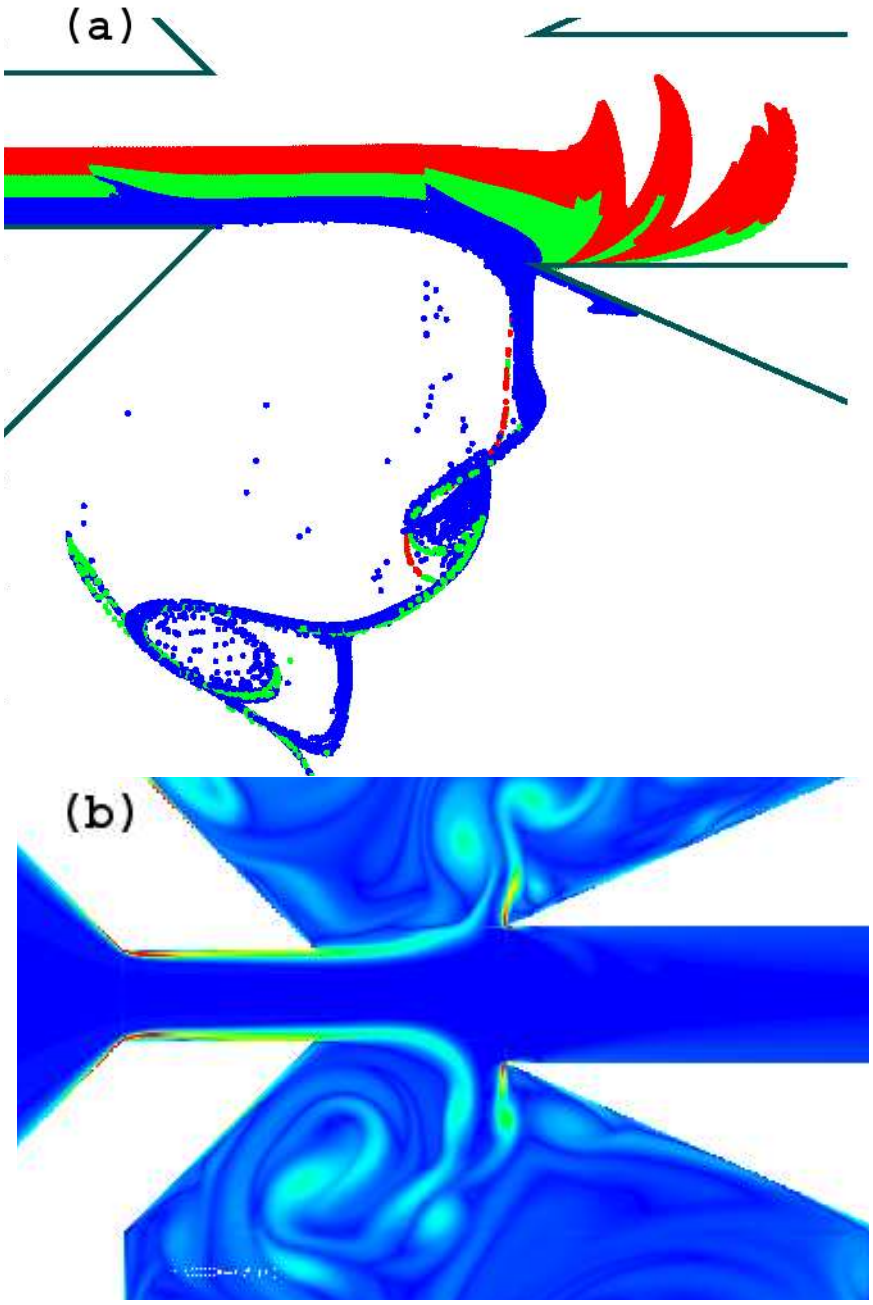

Figure 2.40: (a) solid particles with $d_p = 1.60\mu m$ ($St = 0.25$), (b) vorticity contours: Case II instantaneous still no. 2

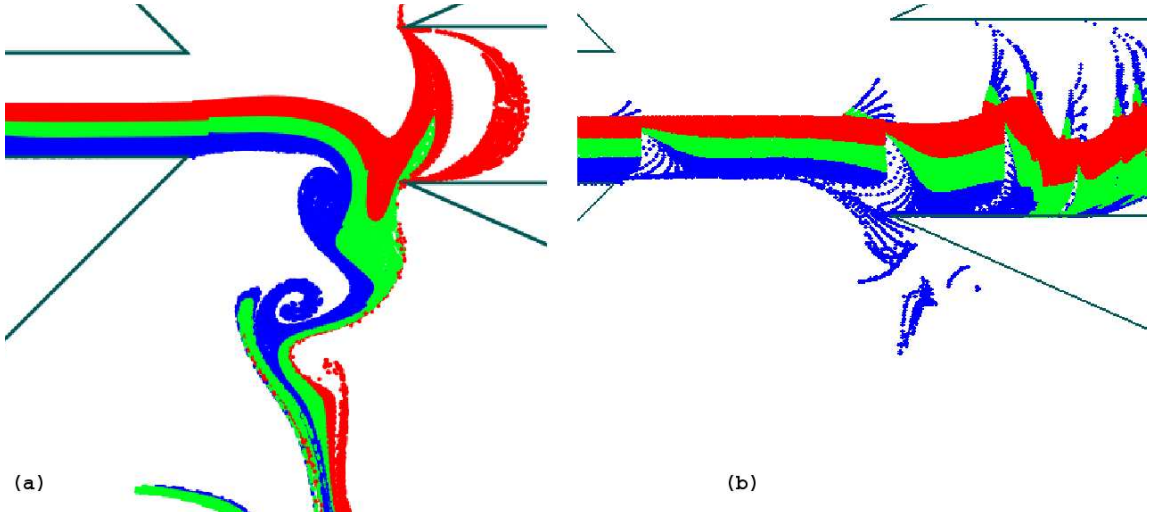

Figure 2.41: (a) massless particles, (b) solid particles with $d_p = 3.20\mu m$ ($St = 1.00$): Case II instantaneous still no. 3

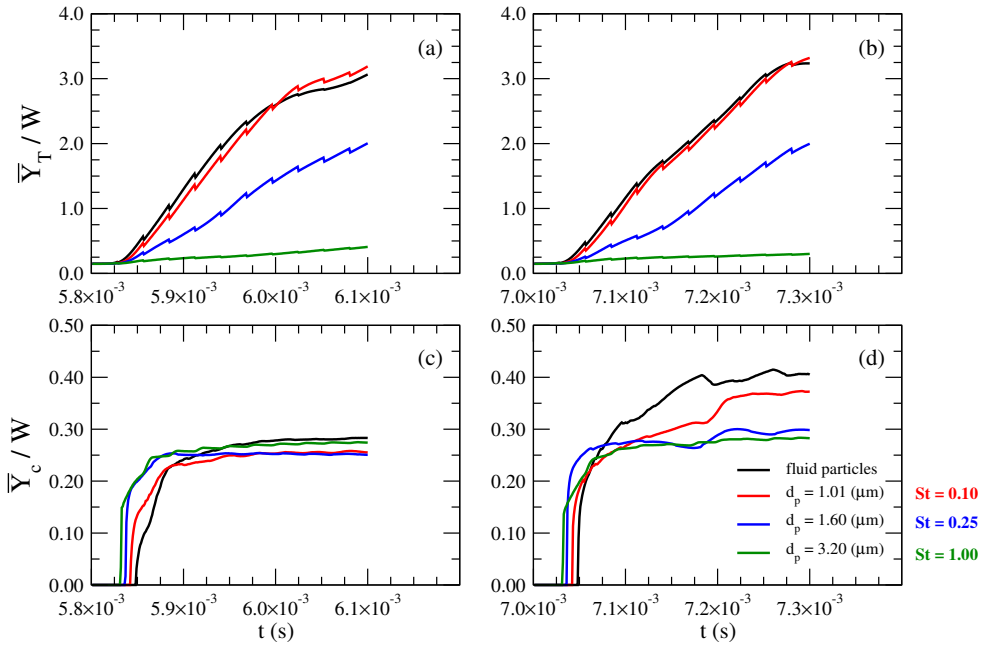

Figure 2.42: Dispersion functions vs. time computed using different time windows. $\overline{Y}_T : a - b$, $\overline{Y}_c : c - d$

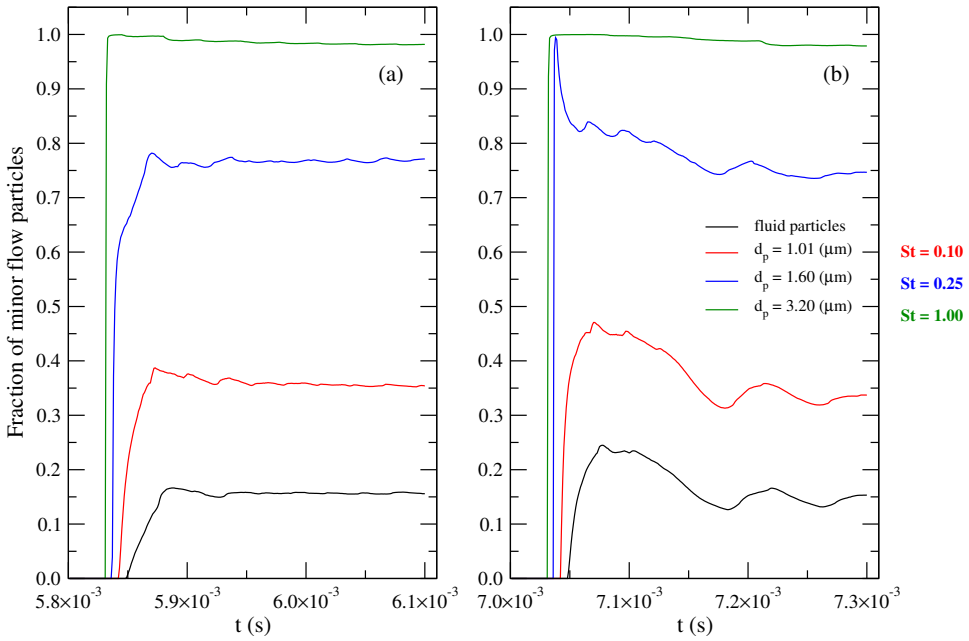

Figure 2.43: Minor flow collection vs. time computed using different time windows

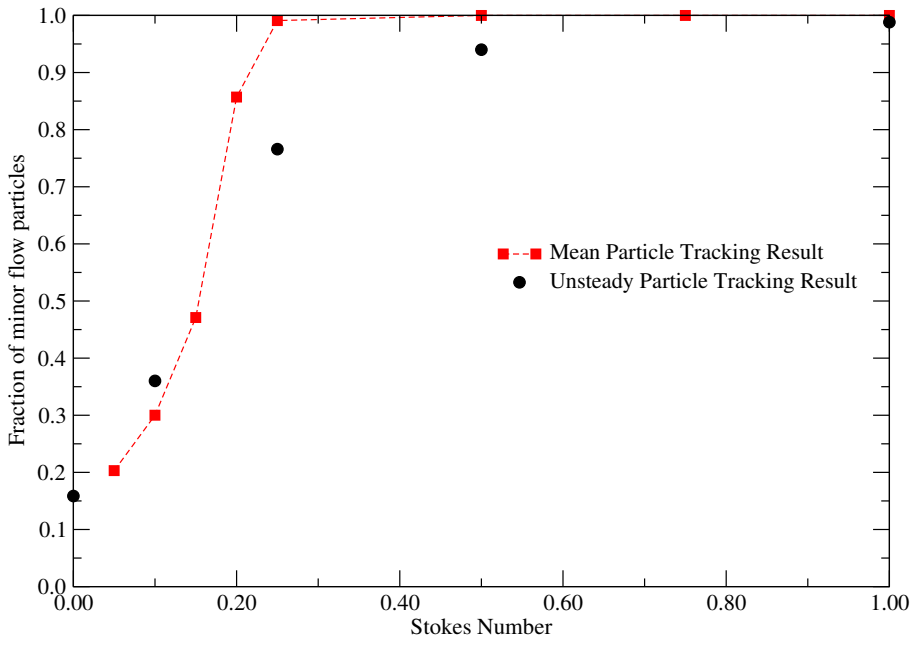

Figure 2.44: Statistical minor flow collection (or propagation) from two time windows compared with mean tracking results of figure 2.17

Chapter 3

Large Eddy Simulation

While the two-dimensional Navier-Stokes solutions presented in Chapter 2 are indispensable for enhancing the understanding of the fundamental mechanisms that come into play during virtual impaction, they are after all only representative of situations where the two-dimensional flow approximation is valid. Thus, to study the flow dynamics of a real life apparatus, such as the circumferential slit virtual impactor, a large eddy simulation is undertaken. In the upcoming sections we will establish the mathematical equations that comprise the core of the method, along with the eminent turbulence closure paradigms that constitute the science of subgrid scale modeling. Finally, two important flow configurations are analyzed to verify the implementation of an ingenious model which is not part of the commercial FLUENT code.

3.1 Overview of the Method

In an LES the three-dimensional unsteady energy containing motions are directly obtained on the grid, whereas the small scale movements or eddies, that are unattainable by the grid are modeled. The latter, of course, are believed to be isotropic and not affected by the flow geometry. The equations solved in LES govern the dynamics

of the large scale eddies of the flow by "filtering" the Navier-Stokes equations. In a direct numerical simulation (DNS), the velocity field $\mathbf{U}(\mathbf{x}, t)$ must be computed on length scales comparable to the Kolmogorov scale. Such a requirement dictates strict and expensive rules on the numerical grid. Fortunately, LES alleviates some of that burden and computes a filtered velocity field $\overline{\mathbf{U}}(\mathbf{x}, t)$, which is still highly capricious. It should not be confused, however, that coarse grids are acceptable. In fact, in order for the sub-grid scale model to adequately mimic the cascade of energy from the resolved large turbulent eddies to the residual motions, the cutoff filter size must lie in the inertial subrange of turbulence. Further constraints arise when a solid boundary is present, and the cost of an LES increases so that the viscous boundary layer is properly computed.

3.2 Mathematical Formulation

A generic definition for a filter function $G(\mathbf{x}, \mathbf{y})$ that produces a filtered velocity field is given by:

$$\overline{\mathbf{U}}(\mathbf{x}, t) = \int_{\Re^3} G(\mathbf{x}, \mathbf{y}) \mathbf{U}(\mathbf{y}, t)\ d\mathbf{y}, \tag{3.1}$$

with the constraint that

$$\int_{\Re^3} G(\mathbf{x}, \mathbf{y})\ d\mathbf{y} = 1. \tag{3.2}$$

In a finite volume discretization it is practical to use the cell control volume as an implicit filter [63]. Therefore, the filter commonly known as "top-hat" is simply for the mono-dimensional case:

$$G(x) = \begin{cases} \frac{1}{\Delta} & \text{if } |x| \leq \frac{\Delta}{2} \\ 0 & \text{otherwise} \end{cases} \tag{3.3}$$

where Δ is the filter width. The filtered velocity then becomes a local average:

$$\overline{\mathbf{U}}(\mathbf{x}, t) = \int_V \mathbf{U}(\mathbf{x}', t)\ d\mathbf{x}',\ x' \in V \tag{3.4}$$

where V is the volume of a computational cell. The residual velocity is consequently defined by

$$\mathbf{u}'(\mathbf{x}, t) \equiv \mathbf{U}(\mathbf{x}, t) - \overline{\mathbf{U}}(\mathbf{x}, t), \tag{3.5}$$

which is reminiscent of the classical Reynolds decomposition. It must be emphasized, however, that $\overline{\mathbf{U}}(\mathbf{x}, t)$ represents an instantaneous rather than a mean quantity, and $\overline{\mathbf{u}'} \neq 0$. Applying the filtering operation to the equations of motion, the filtered continuity equation for an incompressible flow becomes:

$$\frac{\partial \overline{U}_i}{\partial x_i} = 0, \tag{3.6}$$

and the filtered momentum equation takes the form:

$$\frac{\partial \overline{U}_i}{\partial t} + \overline{U}_j \frac{\partial \overline{U}_i}{\partial x_j} = -\frac{1}{\rho}\frac{\partial \overline{P}}{\partial x_i} + \nu \frac{\partial}{\partial x_j}(\frac{\partial \overline{U}_i}{\partial x_j}) - \frac{\partial \tau_{ij}}{\partial x_j} + g_i, \tag{3.7}$$

where $\overline{P}(\mathbf{x}, t)$ is the filtered pressure, and $\tau_{ij} \equiv \overline{U_i U_j} - \overline{U}_i \overline{U}_j$ is the *residual or subgrid-scale* stress tensor. The above equations are strikingly similar to the Navier-Stokes equations, which means that the same well-established numerical methods can be applied for their solution, if only the unknown stress term can somehow be related to the primitive variables.

3.3 Residual Stress Tensor Modeling

From a physical point of view, the residual stress τ_{ij} should underscore the influence that the unresolved part of the flow has on the computed field. A precise theoretical explanation of such mechanism is not in existence, yet there are a number of hypotheses that attempt to clarify this relationship (see for example [63, 64]). With that in mind, a straightforward and efficient eddy-viscosity approach relates the subgrid-scale deviatoric stress tensor to the resolved strain rate tensor:

$$\tau_{ij} - \frac{1}{3}\tau_{kk}\delta_{ij} = -2\nu_T \overline{S}_{ij}, \tag{3.8}$$

$$\overline{S}_{ij} = \frac{1}{2}\left(\frac{\partial \overline{U}_i}{\partial x_j} + \frac{\partial \overline{U}_j}{\partial x_i}\right). \tag{3.9}$$

where ν_T is a subgrid scale eddy viscosity. The first model to parametrize ν_T is known after Smagorinski [65], in which the following assumption holds:

$$\nu_T = (C_s\Delta)^2|\overline{S}_{ij}|, \tag{3.10}$$

where C_s is the *Smagorinski coefficient*, $\Delta \equiv V^{1/3}$ is the local filter length scale, and $|\overline{S}_{ij}|$ is the magnitude of the strain rate tensor defined via $|\overline{S}_{ij}| \equiv \sqrt{2\overline{S}_{ij}\overline{S}_{ij}}$. It is evident that a fixed value for C_s is unreasonable, and a more intelligent choice is by far beneficial. Nonetheless, early attempts were able to determine a useful coefficient ($C_s \approx 0.17$) for the special case of forced, stationary, isotropic turbulence (see [66] for a derivation and references), but it became clear later on that application to a variety of flows is impossible. For instance, in flows with a prevalent mean shear, like a channel, this value proved to be overly dissipative, and ad hoc adjustments were required. Ideally, the coefficient ought to go to zero under laminar conditions, and viscous wall-regions. Moreover, an ability to respond to events associated with

transition to turbulence is highly desirable. To accommodate such complications that are bound to arise in complex geometries, such as the round slit virtual impactor, a *dynamic* eddy viscosity model is selected.

3.3.1 The Lagrangian Dynamic Subgrid Scale Model

In general, a dynamic model samples information from the resolved velocity field in order to breed an optimum value for the Smagorinski coefficient. The basic idea involves the use of filters with different filter widths. In addition to the original grid filter Δ, a secondary *test filter* is explicitly invoked with a width $\widehat{\Delta} \cong 2\Delta$. The filtering operation on this hypothetically coarser mesh yields analogous equations as before, and thus introduces what is referred to as the *subtest-scale* stress $T_{ij} = \widehat{\overline{U_i U_j}} - \widehat{\overline{U}_i}\widehat{\overline{U}_j}$. A pioneering insight into this procedure originated by Germano *et al.* [67] came from the following algebraic identity:

$$L_{ij} = T_{ij} - \widehat{\tau_{ij}}, \tag{3.11}$$

which relates the resolved and directly computable turbulent stress $L_{ij} \equiv \widehat{\overline{U}_i \overline{U}_j} - \widehat{\overline{U}_i}\widehat{\overline{U}_j}$ to the subgrid-scale stresses at the two filtering levels. The usefulness of this identity is seized by assuming a functional form to the stresses τ_{ij} and T_{ij}. Hence, expanding T_{ij} via the Smagorinski approximation analogous to (3.8), we get:

$$T_{ij} - \frac{1}{3} T_{kk}\delta_{ij} = -2(C_s\widehat{\Delta})^2 |\widehat{\overline{S}}_{ij}|\widehat{\overline{S}}_{ij}, \tag{3.12}$$

where $\widehat{\overline{S}}_{ij}$ is similarly defined as in equation (3.9). Substitution of equations (3.8) and (3.12) into the identity (3.11) leads to an overdetermined system of five equations with one unknown C_s. Lilly [68] proposed minimizing the error associated with the use of the Smagorinski model in the Germano identity through a least-squares approach which yields the following expression for computing C_s at each point in space:

$$C_s^2 = \frac{L_{mn}M_{mn}}{M_{pq}M_{pq}}, \tag{3.13}$$

where $M_{ij} = 2[\Delta^2|\widehat{\overline{S}_{ij}|\overline{S}}_{ij} - \widehat{\Delta}^2|\widehat{\overline{S}}_{ij}|\widehat{\overline{S}}_{ij}]$. Computations reported in the literature with the above expression for the coefficient proved to be troublesome due to the excessive variation of the eddy-viscosity field in both space and time. Possible remedies included averaging the expression over homogeneous directions, and accurate results in a channel flow were obtained [67, 69]. In another more complex flow problem around an airfoil with spanwise homogeneity [70], the same technique rendered unrealistic negative coefficients in regions where the flow is laminar, which required *clipping* (i.e. setting $C_s = 0$) in order to conduct a stable calculation. As can be seen, for fully inhomogeneous flows there is a necessity for a more robust approach.

The Lagrangian dynamic subgrid-scale model [71] performs an averaging operation along the trajectories of fluid-particles. In other words, the model coefficient at a point $\mathbf{x}$ depends on the history of the flow pathlines leading up to $\mathbf{x}$. Essentially, the analysis attempts to minimize the error of the closure model in the "Germano identity" over the trajectory of the fluid particle. This results in an expression for the coefficient:

$$C_s^2(\mathbf{x}, t) = \frac{\Im_{LM}}{\Im_{MM}}, \tag{3.14}$$

where

$$\Im_{LM}(\mathbf{x}, t) = \int_{-\infty}^{t} L_{ij}M_{ij}(t')W(t - dt')\,\mathrm{d}t', \tag{3.15}$$

$$\Im_{MM}(\mathbf{x}, t) = \int_{-\infty}^{t} M_{ij}M_{ij}(t')W(t - dt')\,\mathrm{d}t', \tag{3.16}$$

and $W(t - t') = T_m^{-1}e^{-(t-t')/T_m}$ is an exponential weighting function that renders the

above integrals as solutions to a set of relaxation-transport equations:

$$\frac{D\Im_{LM}}{Dt} = \frac{1}{T_m}(L_{ij}M_{ij} - \Im_{LM}), \tag{3.17}$$

$$\frac{D\Im_{MM}}{Dt} = \frac{1}{T_m}(M_{ij}M_{ij} - \Im_{MM}), \tag{3.18}$$

where $T_m = 1.5\Delta(\Im_{LM}\Im_{MM})^{-1/8}$ is a "memory" time scale (see [71] for a discussion and other options).

3.4 Model Validation

The Lagrangian dynamic model is implemented as a *user defined function* (UDF) in FLUENT to complement the existing solver. In terms of numerics there are a number of key issues that must be addressed. The primary concern is the solution of the two additional transport equations (3.17 and 3.18). It turns out that an approximate solution is sufficient to insure the workability of the model. Of course, this is seen as an advantage given the already hefty cost of a standard LES protocol. Following [71], we discretize equation (3.17) in time using a first order scheme:

$$\frac{\Im_{LM}^{n+1}(\mathbf{x}) - \Im_{LM}^{n}(\mathbf{x} - \overline{\mathbf{U}}^{n}\Delta t)}{\Delta t} = \frac{1}{T^n}([L_{ij}M_{ij}]^{n+1}(\mathbf{x}) - \Im_{LM}^{n+1}(\mathbf{x})), \tag{3.19}$$

where the *superscript* indicates the variable at the n^{th} time step, similarly for equation (3.18). Surely, the value of $\Im_{LM}$ at the previous time step n and at a position $(\mathbf{x} - \overline{\mathbf{U}}^{n}\Delta t)$ will not necessarily coincide with an Eulerian meshpoint, which warrants interpolation to time advance the equations. First the search for the "nearest neighbors" of the upstream location must be completed, and then a suitable interpolation scheme is invoked. The former task is accomplished by pre-processing the grid struc-

ture information so that the neighbors of each computational cell are stored and ready to be quickly accessed during the course of the simulation (i.e. $O(1)$). The latter task is handled by the same second-order interpolation scheme used for particle tracking. As mentioned before, the dynamic procedure requires an explicit test-filtering operation. The most suitable choice, of course, is the top-hat filter which is consistent with the finite-volume discretization. Therefore, $\widehat{\overline{U}}(\mathbf{x})$ is simply the local average of $\overline{U}(\mathbf{x})$ involving the neighbor cells. Mathematically, given a grid filtered variable $\overline{\phi}$, its corresponding test filtered variable is:

$$\widehat{\overline{\phi}} = \frac{\sum_{i=1}^{N_c} \overline{\phi}_i V_i}{\sum_{i=1}^{N_c} V_i} \tag{3.20}$$

where N_c is the number of neighboring cells. In the upcoming sections we will present the results of this model in two canonical turbulent flow problems.

3.4.1 Fully Developed Turbulent Channel Flow

The cornerstone of wall bounded turbulent flows is the fully developed channel. The clarity of this geometrical problem makes it a righteous ground to target the understanding of fundamental concepts related to the mechanics of wall generated turbulence. For obvious reasons, numerous experimental and theoretical studies were dedicated to the analysis of a channel flow. Absolutely, the performance of any turbulence closure model is first sought here since it can add strength to the model's capability of dealing with more complex configurations, which will undoubtedly share some of those basic flow characteristics as the channel. It should be stated that the original authors confirmed the correctness of the Lagrangian subgrid-scale dynamic model in a fully developed turbulent channel flow at a Reynolds number $Re_\tau \approx 641$, based on friction velocity, $U_\tau \equiv (\tau_w/\rho)^{1/2}$, and channel half-width δ_h. The numerical method relied on a pseudo-spectral code [72]. Our aim is to demonstrate the ad-

vantage of the model in a less specialized and multi-purpose code such as FLUENT. The DNS results of Moser *et al.* [73] will be used to attest the accuracy of the implementation using the standard numerical tools available in FLUENT. The channel dimensions, relative to $\delta_h \equiv 1\ m$, are taken to be $2\pi\delta_h \times 2\delta_h \times \pi\delta_h$ in the streamwise (x), wall-normal (y), and spanwise (z) direction, respectively. The underlying mesh consists of $98 \times 66 \times 66$ cells. The non-uniform distribution of grid cells in the y direction is shown in figure 3.1, for the half-width. Periodic boundary conditions are prescribed in the x and z directions, with a constant streamwise pressure gradient to drive the flow. The Reynolds number based on the mean centerline velocity and δ_h is 3300, corresponding to $Re_\tau = U_\tau \delta_h / \nu = 180$, using $\nu \equiv \frac{\mu}{\rho} = \frac{0.0025}{1.0}\ m^2/s$.

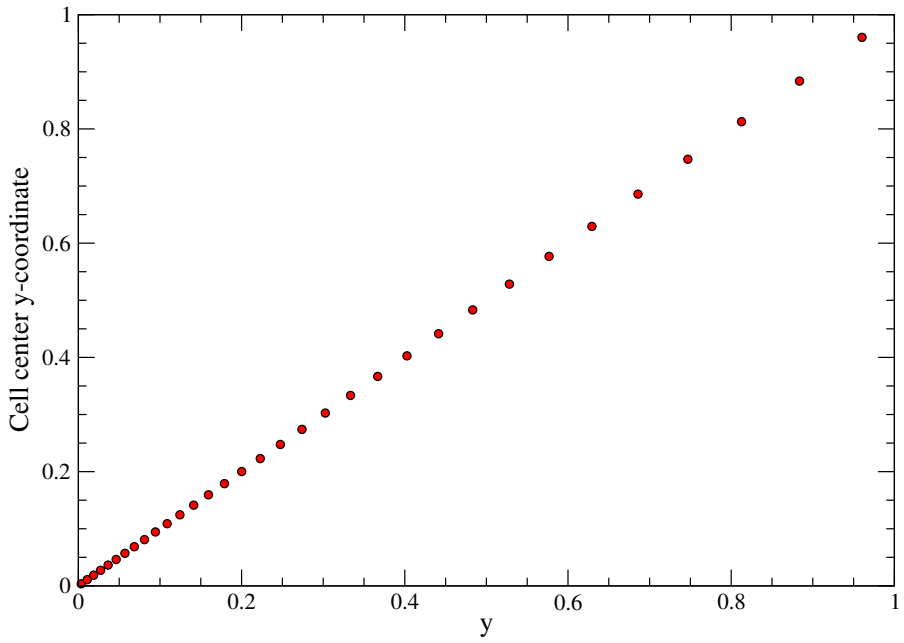

Figure 3.1: Nonuniform channel mesh normal to wall

The simulation is started from another LES calculation at a slightly higher Reynolds number [74]. The initial velocity field is interpolated onto the current grid, and the flow is evolved for a long period of time before reaching a statistical steady

state. Acquisition of data begins and averaging is performed over a number of time steps $N_t \Delta t \sim 3.6T^+$, where $T^+ \equiv \delta_h / U_\tau$ is a dimensionless wall-time unit. The statistical mean velocity is then computed as the time average:

$$< U_i >= \frac{1}{N_t} \sum_{j=1}^{N_t} \overline{U}_i(t_j), \tag{3.21}$$

and the root mean square (rms) velocity is:

$$U_i^{rms} = \left[\frac{1}{N_t} \sum_{j=1}^{N_t} (\overline{U}_i(t_j) - < U_i >)^2 \right]^{1/2}. \tag{3.22}$$

Figure 3.2 shows the time-mean streamwise velocity in the center of the channel, averaged over a number of spanwise sampling locations and non-dimensionalized by U_τ (i.e. $< U >^+ \equiv < U_x > / U_\tau$, where $U_\tau = 0.45$). It is clear that excellent agreement is obtained between the DNS and LES predictions. The linear behavior up to $y^+ \equiv yU_\tau/\nu$ of 5 is also shown, along with the log law near the centerline (dashed lines). Figure 3.3 depicts the level of velocity fluctuations normalized by U_τ. The peak in streamwise turbulence intensity is predicted very well, with a slight shift. There is some disagreement near the centerline where the grid is relatively coarser. On the other hand, exceptional accord in the wall-normal and spanwise intensity levels is achieved.

3.4.2 Turbulent Flow Past a Square Cylinder

The flow around a bluff body is a "tough" test case to investigate the effectiveness of the Lagrangian dynamic model. From a fluid dynamics point of view, the wake flow at a high Reynolds number ($Re \approx 21,400$) exhibits quite complex features of "coherent" vortex structures. Near the front end, of course, a stagnation region must be properly resolved, as well as a highly deformed shear layer, with strong recirculation on the back side. This problem has also captured the attention of many turbulence

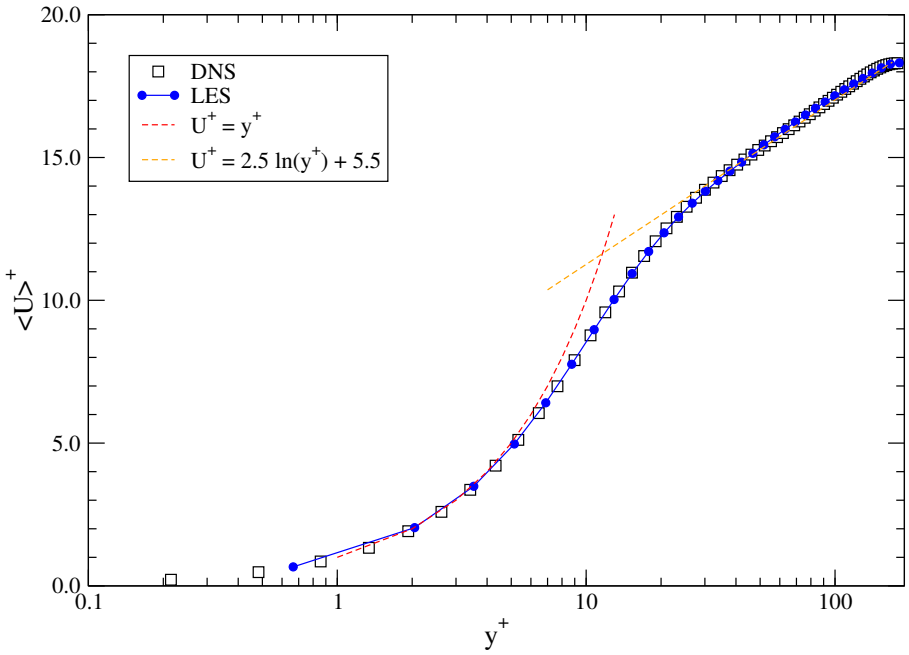

Figure 3.2: Spanwise averaged mean velocity profile; DNS data from [73]; law of the wall & log-law are shown for comparison

numericists [75, 76], and experimentalists [77, 78]. For the sake of this research, it is presumed that similar flow characteristics will be present in the virtual impactor. Figure 3.4 shows a cross section of the three dimensional computational domain. Flow is from left to right. The origin lies at the center of the backside edge. The dimensions relative to the short edge length $d_s = 1\ m$ are: $7.4d_s$ (upstream), $15.8d_s$ (downstream), $9.35d_s$ (top/bottom), and $A = 4d_s$ (depth). A stretched mesh with fine gridding near the cylinder walls is designed based on recommendations established by Sohankar *et al.* [76], but with a higher number of nodes. Explicitly, $288 \times 192 \times 32$ control volumes are assigned for this calculation compared to $185 \times 105 \times 25$ used by the aforementioned authors. Figure 3.5 is a representative plot of the cell center locations in the immediate proximity of the cylinder. The free stream velocity $U_\infty = 0.32\ m/s$ is chosen such that for air, $Re = U_\infty d_s/\nu = 21400$. The boundary conditions prescribed a uniform flow at the inlet ($\overline{U}_x = U_\infty, \overline{U}_y = \overline{U}_z = 0$) with 1% turbulence intensity. This value

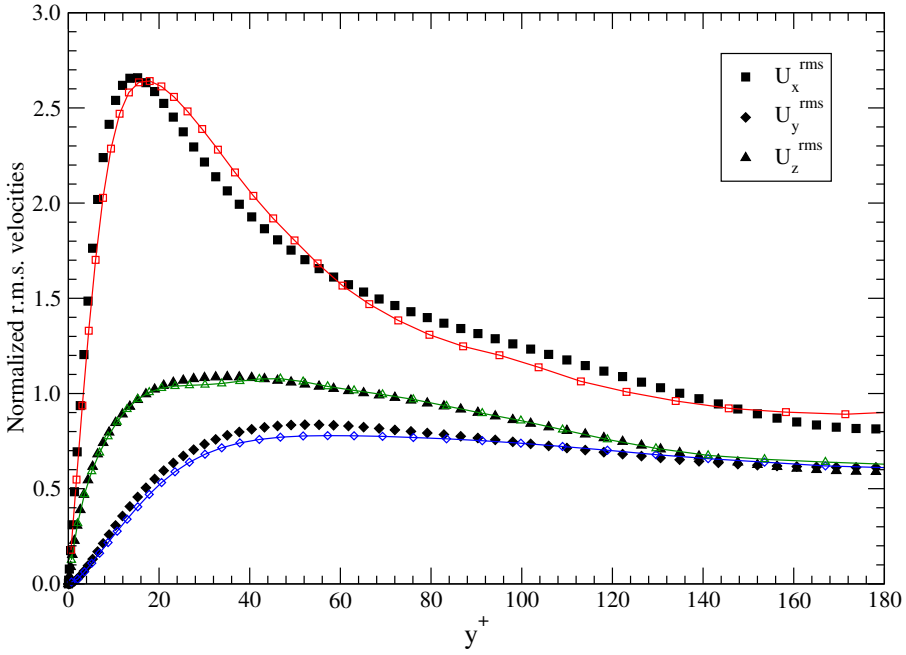

Figure 3.3: Spanwise averaged root mean square velocity components; 'colored lines': LES, 'symbols': DNS data from [73]

comes as a middle ground between the 2% value reported in the experiment [78], and the completely laminar profile specified in the literature simulation. Lastly, the convective boundary condition discussed in the Appendix is utilized for the outflow plane. The flow is evolved from rest using the Smagorinski model for about 80 time units, $T^* \equiv d_s/U_\infty$, after which the Lagrangian model functions (equations 3.17, 3.18) are initialized and the simulation is carried out for $43T^*$ more units. Data averaging is then performed over approximately seven shedding cycles, or $60T^*$, as shown in figures 3.6 and 3.7, which record the lift and drag coefficients, evaluated from the net pressure and viscous forces on the cylinder walls in the y and x directions, respectively, and defined by:

$$C_L = \frac{\text{surface lift}}{\frac{1}{2}\rho(A \times d_s)U_\infty^2} \tag{3.23}$$

$$C_D = \frac{\text{surface drag}}{\frac{1}{2}\rho(A \times d_s)U_\infty^2} \tag{3.24}$$

The mean lift ($\overline{C}_L$) and drag ($\overline{C}_D$) coefficients are also drawn. This affords a comparison of the simulation global predictions with the reference experimental and numerical data. Furthermore, it is customary to report on the Strouhal number, which is a dimensionless measure of the wake shedding period T_s,

$$St_h = \frac{d_s}{T_s U_\infty}. \tag{3.25}$$

Table 3.1 summarizes the different models' predictions along with the results extracted from the literature. The last two columns relate to the root mean square of the lift and drag signals, respectively. The slight variations in the r.m.s. values for the drag coefficient are somewhat expected because of the high frequency of the signal, and changes in the length of the sampling time frame. The focus will now be on the ability to predict velocity statistics in the turbulent wake. Figure 3.8 shows the spanwise- and time-averaged streamwise velocity, normalized by U_∞, downstream of the body at its centerline. Also shown, are results from a dynamic version of the Smagorinski model obtained by Sohankar *et al.* [76]. In their calculation, the authors resorted to spatial averaging in the homogeneous z direction in order to solve for the model coefficient using equation 3.13, as well as restricting the total viscosity to the positive space ($\nu + \nu_T \geq 0$). An important physical observation is the wake closure point, which is the position behind the cylinder having a zero velocity. It appears that the Lagrangian dynamic LES predictions for the mean velocity are very much in tune with the experimental data [78], especially in the near wake. In addition, beyond the closure point, the growth rate of the wake velocity is adequately captured up to $x \approx 2$, after which there is a slight increase in the restored velocity compared to the experimental data. There are a number of reasons that can contribute to this behavior which we will comment on after we present the results for the second order

statistics. Figure 3.9 shows the root mean square streamwise velocity also averaged in the spanwise plane. In this case, it seems the fluctuation peak predicted by the simulation is somewhat higher than what is found in the experiment, but in the long wake the agreement is excellent. Lastly, figure 3.10 depicts the behavior of the r.m.s. wall-normal averaged velocity. Good agreement is witnessed in the near wake but the simulation fluctuation levels experience a much faster decline in the far wake. The trend that is educed by looking at the simulation results compared to the experiment, suggests that generally in the near wake where the mesh resolution is highest, the model performs well, whereas as we move further away from the cylinder the mesh resolution is stretched which can lead to some error. It should be stated, however, that not only numerical errors can be the reason for the observed discrepancies. In fact, subtle differences exist between the flow conditions set in the simulation and those of the real experiment, namely the laboratory investigators report that the presence of the cylinder in their laboratory channel resulted in 5% to 10% deficit in the centerline inflow velocity. In addition, the level of free stream turbulence was found to be $\approx 2\%$. In the LES calculation, we only superimpose 1% perturbation on to the uniform incoming flow. Finally, the length of the cylinder into the plane, or aspect ratio can be a factor. Clearly, in the simulation it is not economical to construct a very long cyliner, thus the use of periodic boundary conditions may prohibit the emergence of some spanwise structures that develop for long aspect ratios ($A = 9.75d_s$ *in experiment*). With regard to the results, however, we notice that the only potentially problematic deviations are those of the wall-normal velocity fluctuations away from the cylinder. We already alluded to the role of the grid in that region, but we can also recall the LES results of the channel flow, particularly figure 3.3, where there was also a nominal drop in the wall-normal intensity levels. This may very well be an inherent weakness of the filtering procedure in elongated grids.

LES/EXP	St_h	$\overline{C}_D$	C'_L	C'_D
Smagorinski	0.126	2.23	1.26	0.27
Dynamic Lagrangian	0.129	2.18	1.28	0.34
Experiment [78]	0.130	2.10	—	—
Smagorinski [76]	0.127	2.22	1.50	0.16
Dynamic Smagorinski [76]	0.126	2.03	1.23	0.20

Table 3.1: Comparison of Strouhal number, mean drag, r.m.s. lift, & r.m.s. drag for flow past a square cylinder. 'Dynamic Lagrangian' is the adopted simulation result

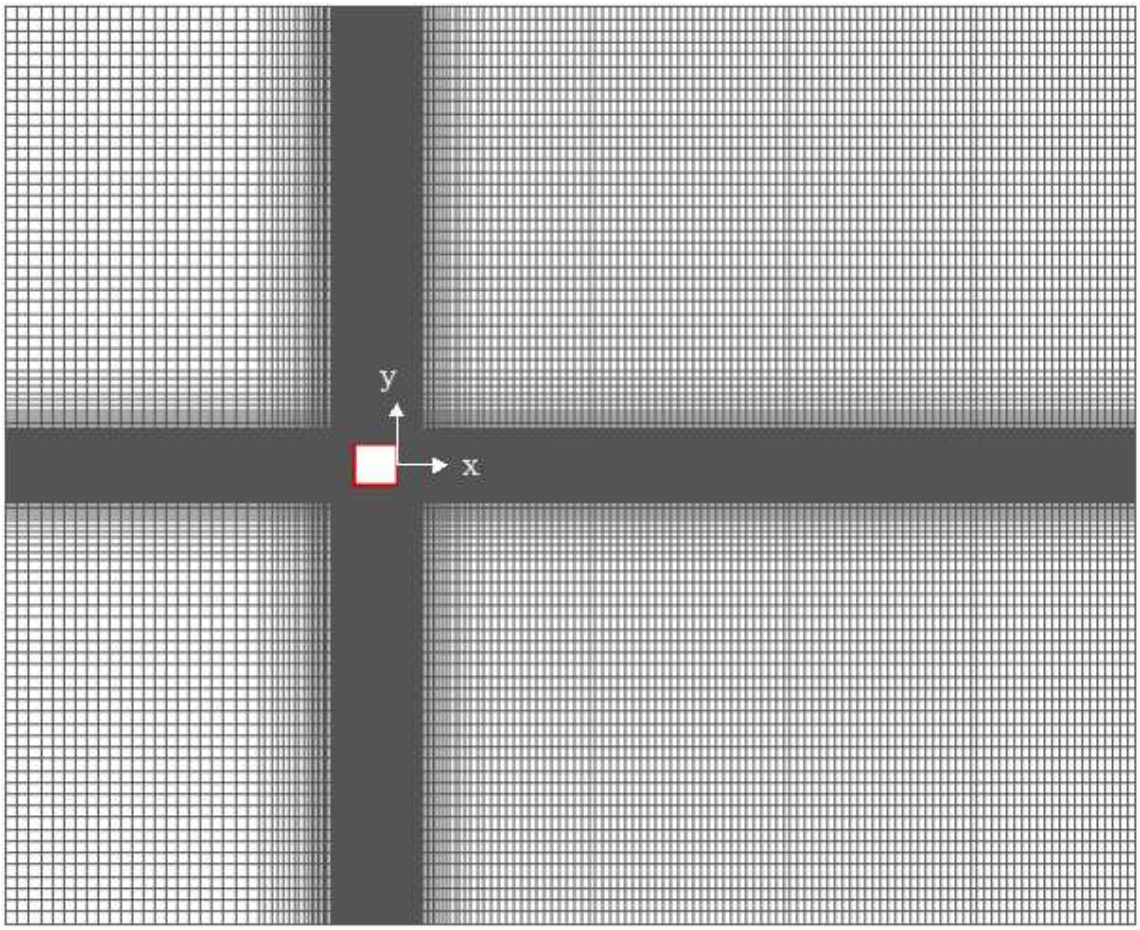

Figure 3.4: Slice of computational domain of flow past a square cylinder

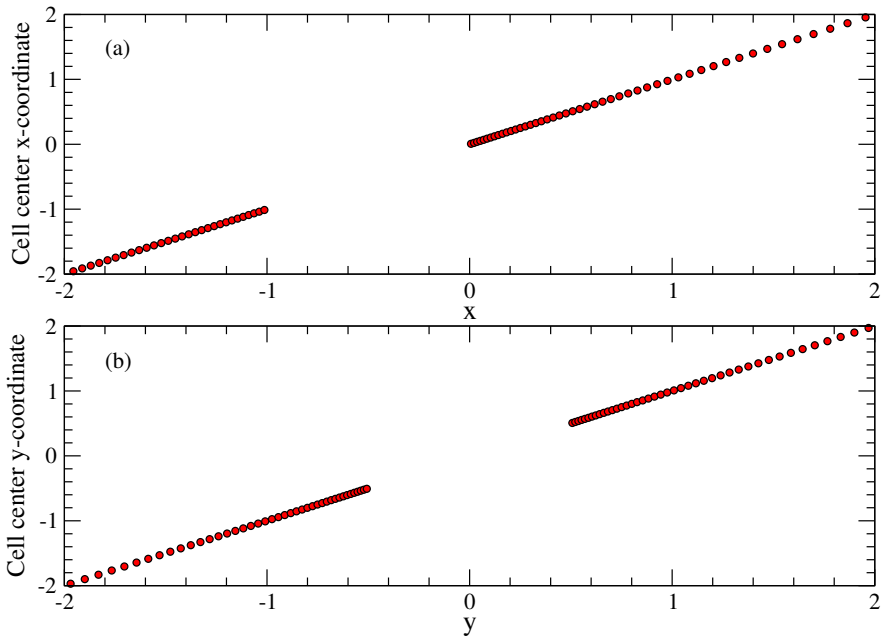

Figure 3.5: Nonuniform mesh around square cylinder. (a) Horizontal; (b) Vertical

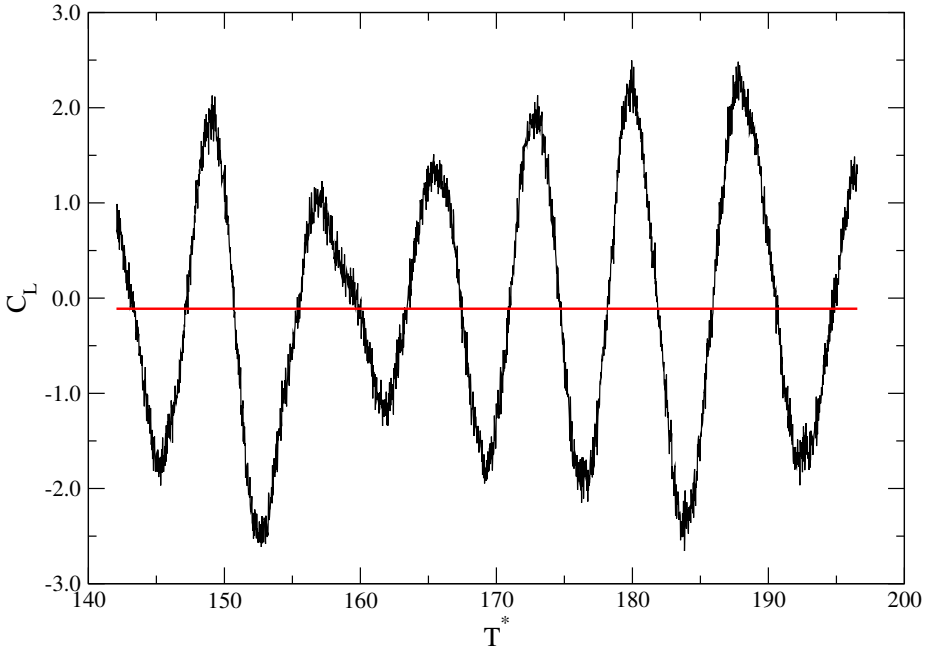

Figure 3.6: Square cylinder lift coefficient versus time

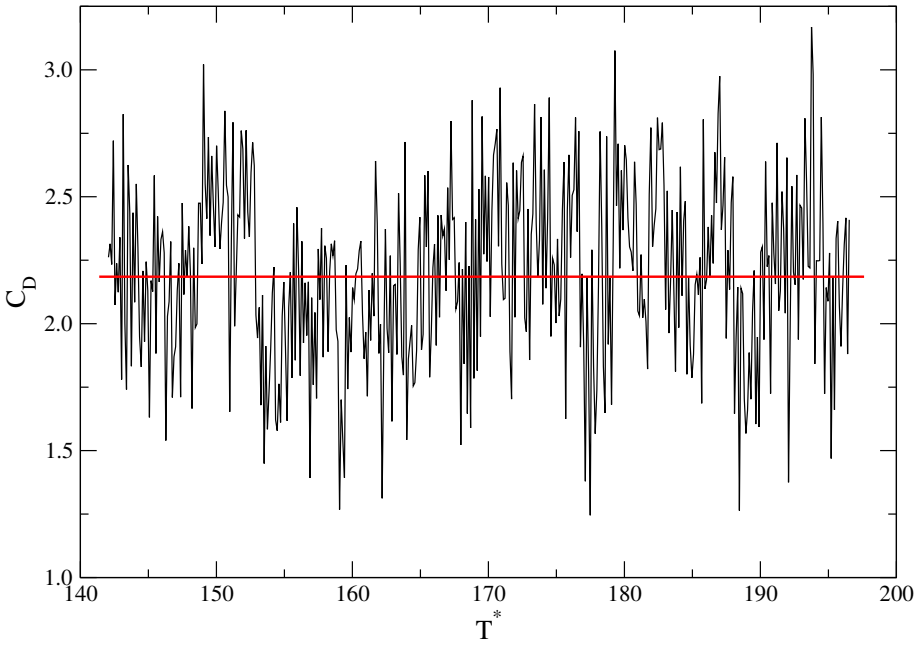

Figure 3.7: Square cylinder drag coefficient versus time

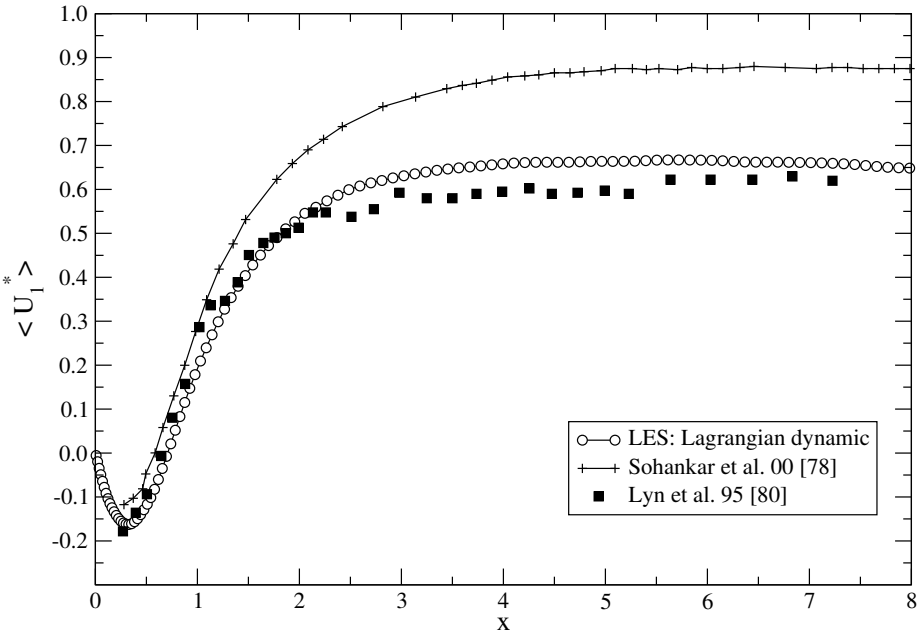

Figure 3.8: Normalized streamwise velocity averaged in z and t. Cylinder wake: $y = 0$

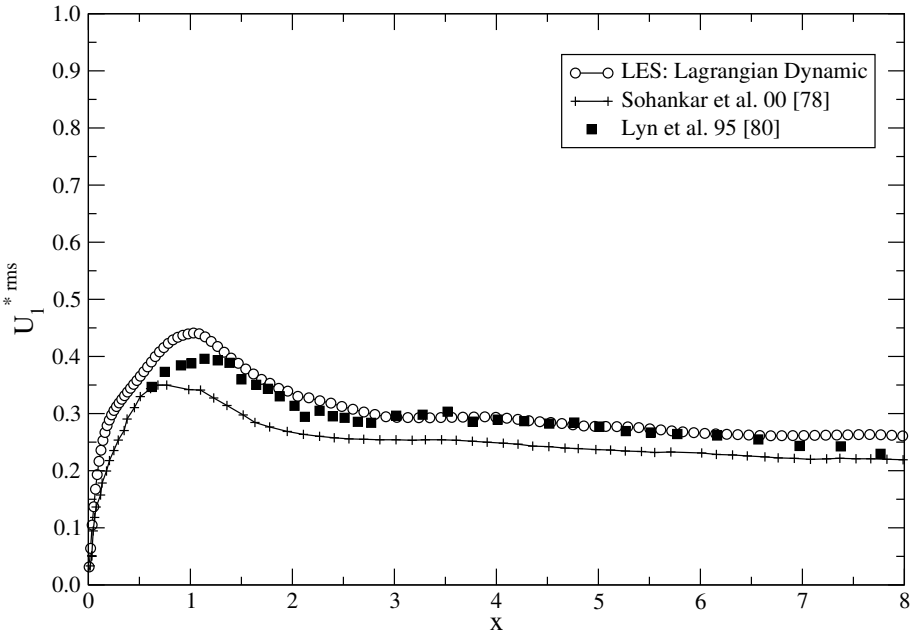

Figure 3.9: Normalized streamwise r.m.s. velocity averaged in z and t. Cylinder wake: $y = 0$

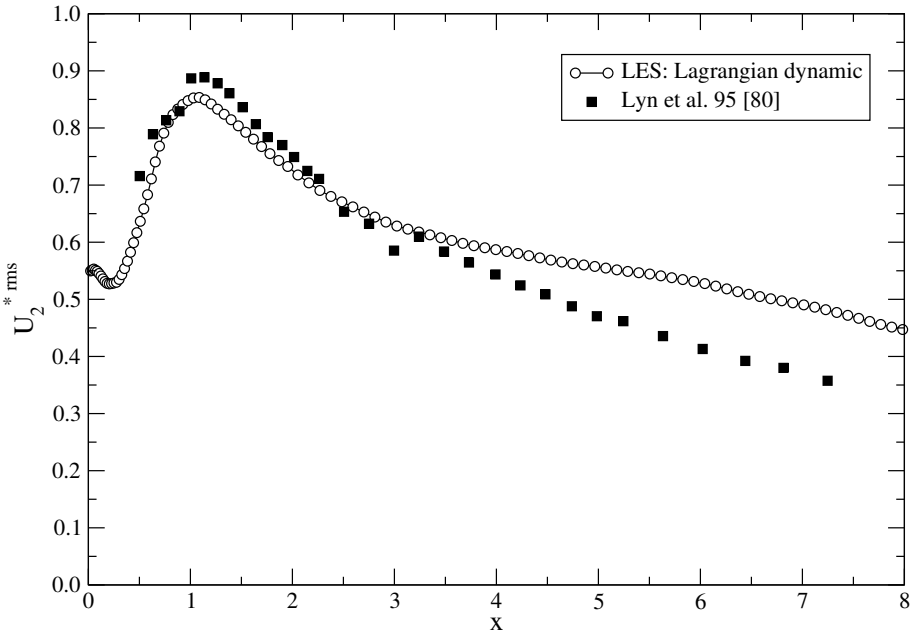

Figure 3.10: Normalized wall-normal r.m.s. velocity averaged in z and t. Cylinder wake: $y = 0$

Chapter 4

LES of Round Slit Virtual Impactor

In this chapter we shall examine and discuss the results of the large eddy simulation performed on a real virtual impaction device. A representative image of a complex geometry cylindrical slit design is shown in figure 4.1. For our purposes, a computer model based on the dimensions of a prototype apparatus is generated along with a structured internal mesh of the flow domain. A number of turbulence closure models for the residual stresses are evaluated, and their performance in terms of CPU time and accuracy will be compared. The final analysis will focus on the behavior of aerosol particles and their interplay with the coherent eddy dynamics. We conclude by interpreting the simulation predictions in light of preliminary particulate collection experimental data.

4.1 Geometry & Flow Conditions

The prototype device is pictured in figure 4.2 as it stands in a wind tunnel experiment. The device functions by pulling particle-laden air through a narrow cylindrical slit (red arrows). The mixture then separates internally when it reaches

the virtual impactor jet which is hidden from view. The major flow in the top and bottom annulus is exhausted through pipes connected to vacuum pumps. The minor flow, on the other hand, is diverted radially to the focal center tube. The outer diameter of the entire compartment is 12.70 cm. A computer generated design of the sampler is shown in figure 4.3, and a sample grid used in the LES computation is shown in figure 4.4. Note that we are only simulating a $\pi/4$ sector of the full circle. Hence, the planar dimensions are identical to the two-dimensional geometry studied earlier (see figure 2.1). The numerical mesh is first applied to a single vertical plane in the domain, and then rotated to produce hexahedral or six-faced cells. Two computational grids with increasing levels of clustering are constructed. The first mesh consists of 4.08 million cells. The critical region formed by $W \times S \times C$ contains $35 \times 60 \times 170$ control volumes, where $W = 0.70\ mm,\ S = 1.47\ mm$, & $C = 8.26\ mm$ designates the length of the jet arc joining the border planes where *rotational* periodic boundary conditions are applied. Surely, the node distribution near the no-slip walls of the jet and its expansion bays is non-uniformly spaced, as was done in the 2-D study. The finer mesh lattice holds 6.01 million cells. The refinement focused on areas near sharp edges as well as denser radial allocation, specifically 220 $vs.$ 170 cells along the arced jet extension. In terms of wall units, there is no straightforward location where the friction velocity can be defined. Instead, we probe the wall region of the major flow jet as it shears past the inclined expansion bay in order to quantify the grid spacing relative to the local velocity gradient near the wall. The dimensionless grid size $(\Delta x^+, \Delta y^+, \Delta z^+)$ of the first cell is $(4.2, 0.6, 1.8)$, and $(3.1, 0.6, 1.3)$ for each mesh, respectively. Similar inflow and outflow boundary conditions as in **case II** of Chapter 2 are set. The flow parameters correspond to a total sampling rate $Q_T = 600\ liters/min$, at a Reynolds number $Re \equiv 2WU_o/\nu = 4744$, based on average jet centerline velocity and hydraulic diameter. The minor flow on the opposite end of the jet is consistently fixed at $Q_m = 0.10\ Q_T$.

In the upcoming sections, we shall interpret the results obtained from three separate calculations. Initially, the velocities in the cells are set to zero, and the simulation is conducted using the Smagorinski model (equation 3.10 with $C_s = 0.1$). The calculation time step remained $\Delta t = 1.0 \times 10^{-6}\ s$. The flow is evolved for approximately $45\tau_{vi}$ time units, after which the Lagrangian model functions (equations 3.17, 3.18) are initialized and the simulation is progressed for additional $168\tau_{vi}$ units before statistics are accumulated. A secondary computation involving the Lilly dynamic model (equation 3.13) is also analyzed. The third and final calculation is computed on the finer mesh from an interpolated coarser solution using the Lagrangian dynamic model in order to assess the influence of the grid on the results. As mentioned earlier, the refinement enhanced the grid resolution in areas near the jet shear layers, as well as the azimuthal spacing. Table 4.1 outlines the numerical parameters for all the large eddy simulations performed in this study. The LES equations are solved by the same second-order implicit scheme (see Section 2.3.2 for details). Table 4.2 summarizes the computational expense associated with each run. The figures in Table 4.2 are obtained by measuring the CPU time in seconds of **eight** AMD Opteron^{270} parallel processors. The wall-clock-time ideally should correspond to $1/8^{th}$ the total CPU time, however it is slightly more due to the message passing cost, which is quantified as a percentage of *actual/ideal* time, in the last column. It is demonstrated, therefore, that the newly implemented Lagrangian dynamic model is only 35% more expensive than the standard Smagorinski model, and merely 4% more than the dynamic Lilly, which is built-in with the commercial FLUENT code.

Case	Model	Mesh Size	Δt (s)	U_{in} m/s	Re	$Q_m/Q_T{}^*$
I	Smagorinski	4.08×10^6	1.0×10^{-6}	1.07	4744	10.0 %
II	Lilly	4.08×10^6	1.0×10^{-6}	1.07	4744	10.0 %
III	Lagrangian	4.08×10^6	1.0×10^{-6}	1.07	4744	10.0 %
IV	Lagrangian *refined*	6.01×10^6	1.0×10^{-6}	1.07	4744	10.0 %

Table 4.1: Summary of models and numerical parameters used in each large eddy simulation. *setting ratio (not necessarily constant with time)

Case	Model	CPU Time (s)	Wall-Clock Time (s)	Comm.(%)
I	Smagorinski	1580.0	246.4	24.8
II	Lilly	2005.8	321.1	28.1
III	Lagrangian	2211.6	333.1	20.5
IV	Lagrangian *refined*	3307.6	494.8	19.7

Table 4.2: CPU usage and parallel communication overhead per LES time-step

4.2 Virtual Impaction Statistics

In order to understand the general characteristics of the flow, it is important to probe its time-averaged behavior. In the current context, as was initiated in the 2-D study, statistics of the fluid velocity and pressure are accumulated for a significant number of jet throughput times. Table 4.3 identifies the span of dimensionless time units stored for each model. Note that the examined flow fields are saved after considerable passage from startup, and the time-averaged results are believed to be statistically converged. As mentioned earlier, we shall first examine the effect of the underlying mesh on the flow statistics. We choose a vertical plane in the middle of the computational domain (i.e. $\pi/8$ rotation), and sample the time-averaged velocity magnitude and root mean square velocity components. Figure 4.5 is a representative plot of the time-mean velocity, $< U >= \sqrt{< U_x >^2 + < U_y >^2 + < U_z >^2}$, and out-of-plane r.m.s velocity components as obtained from solutions using the Lagrangian dynamic model on the two aforementioned grids. The profiles are recorded at $x^* = 0.5$, in other words half-way between jet and collection. As can be seen, the influence of the grid is negligible on the mean velocity. There is a slight shift in the peak of the U_x^{rms}

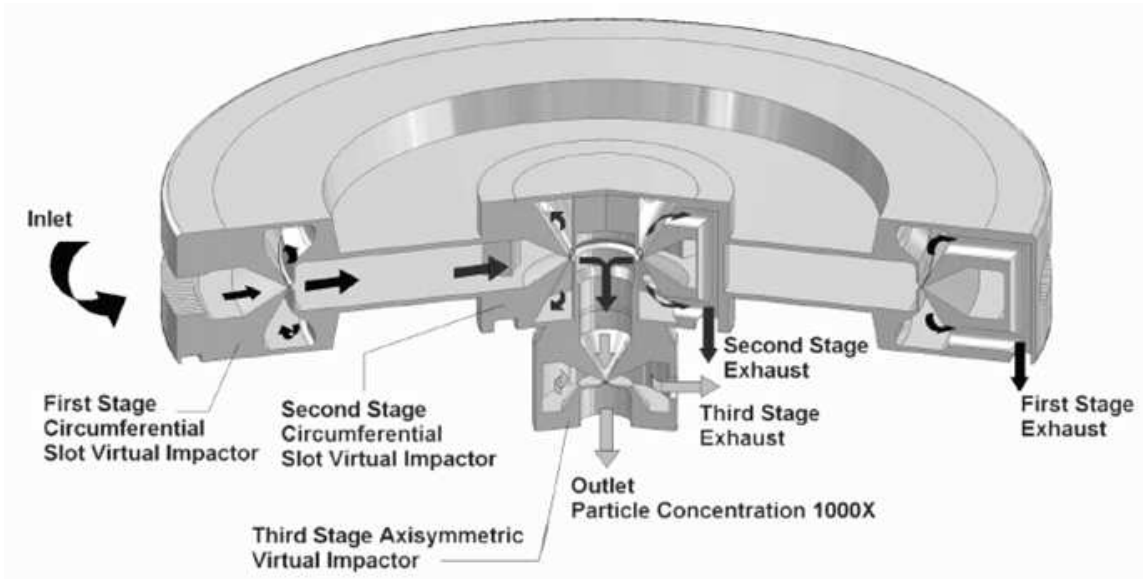

Figure 4.1: Rendering of a multi-stage circumferential slit virtual impactor from [59]

profile at the outer jet mixing layer. The most pronounced effect lies in the U_z^{rms} profile. Recall that the finer grid resolution is enhanced along the circumference. For this reason, the influence of the refinement is manifested as a dampening of the fluctuation levels, primarily in the mixing layer regions above and below the jet column. Henceforward, in the discussions pertaining to second-order statistics we shall utilize the solutions of the finer grid.

The current three-dimensional large eddy simulation is indeed the preferred approach for mimicking the flow dynamics inside the prototype sampler, however, having invested in a direct two-dimensional simulation, it is natural to question the suitability of such an approach. Figure 4.6 shows a comparison between a 3-D and the 2-D solution. We limit this interrogation to the mean velocity behavior in the

Case	Model	$N_t \Delta t / \tau_{vi}$
II	Dynamic Lilly	36
III	Dynamic Lagrangian	62
IV	Dynamic Lagrangian *refined*	57

Table 4.3: Number of jet throughput time-units included in the LES statistics

Figure 4.2: Prototype circumferential personal aerosol sampler

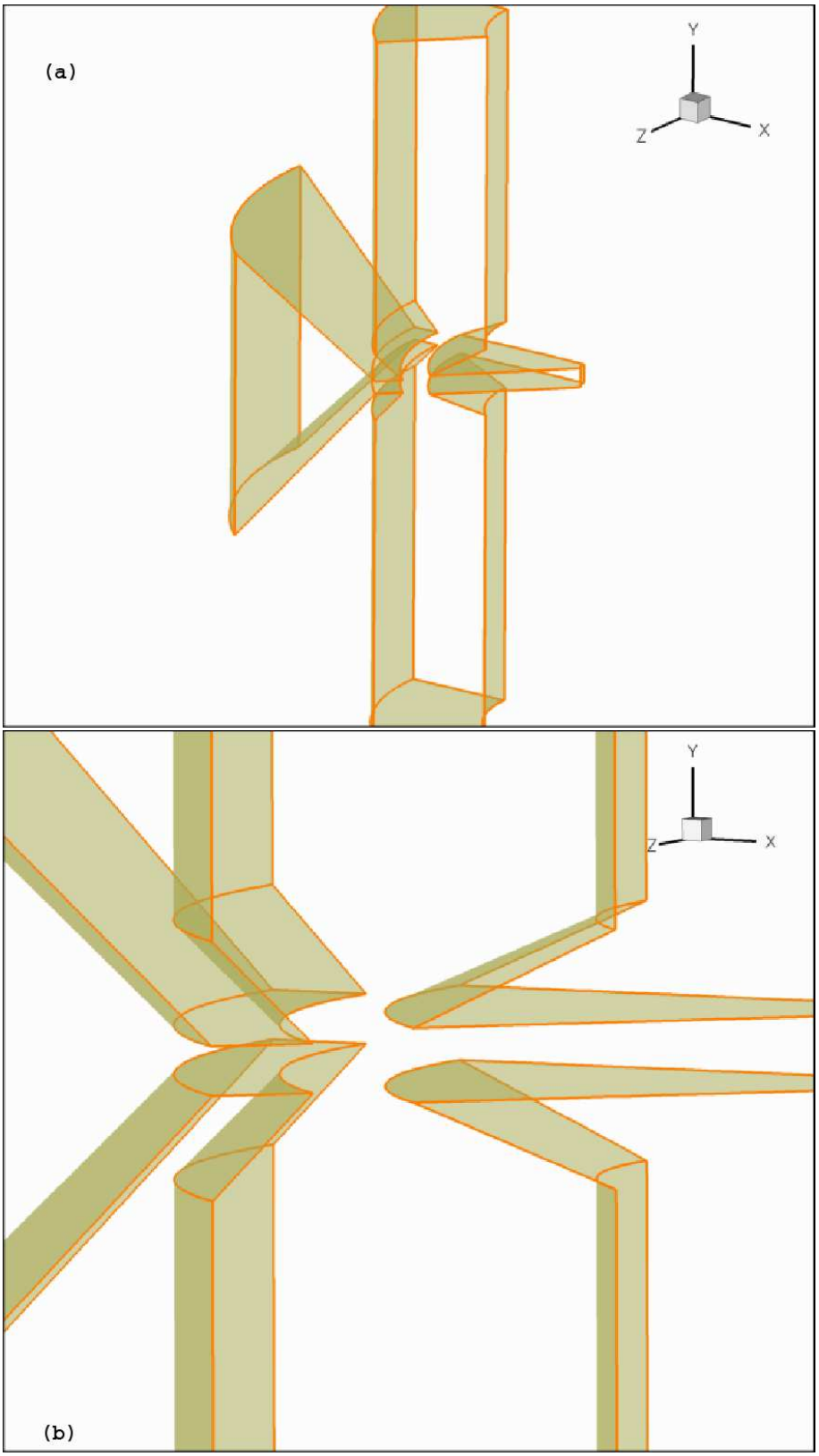

Figure 4.3: LES computational domain with rotational periodic boundary conditions representing the circumferential virtual impactor. (a) full view, (b) nozzle view

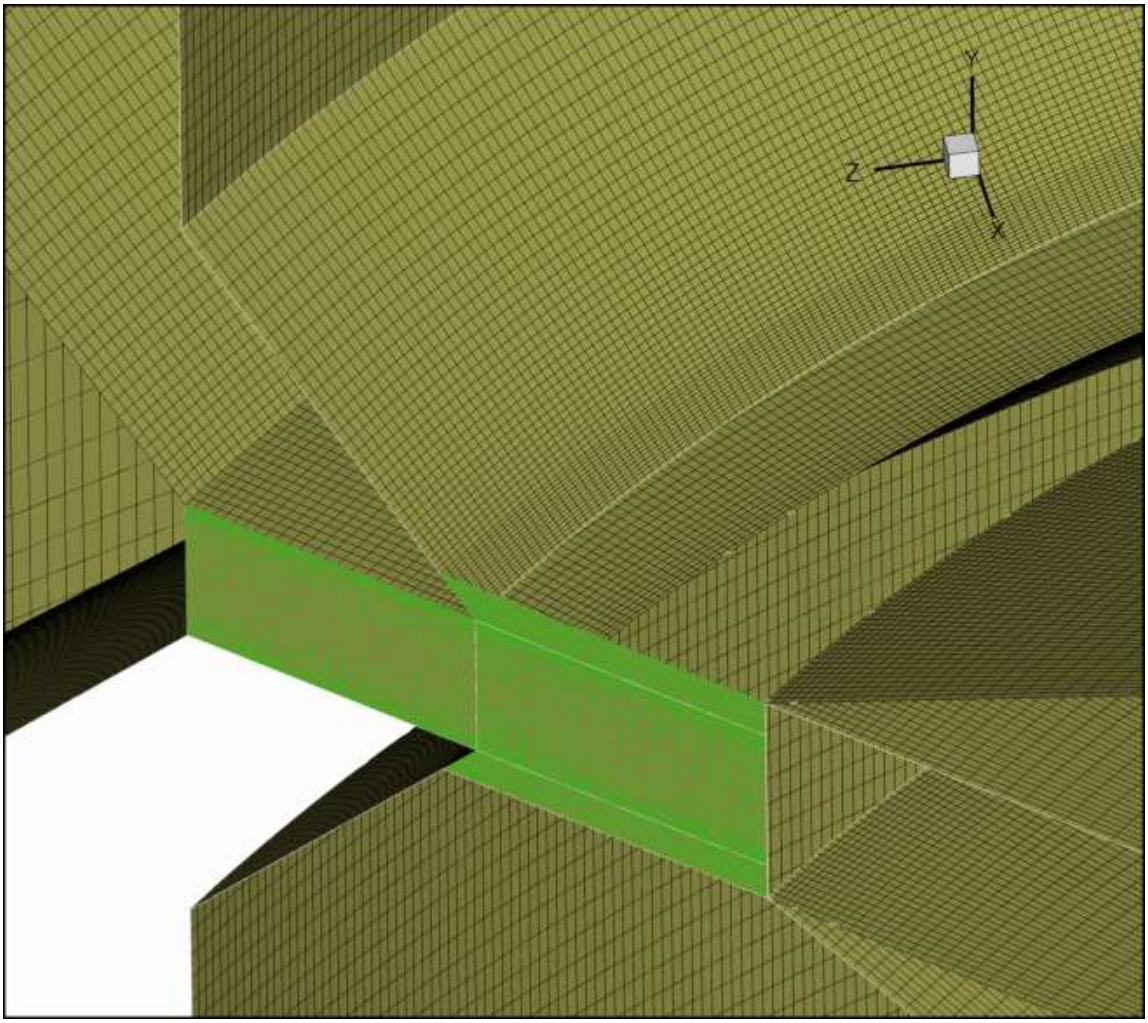

Figure 4.4: Sample mesh outline around radial virtual impaction nozzle

virtual impaction gap. The LES data points are consequently normalized by the **same** centerline velocity U_o, and plotted along with the two-dimensional numerical data which is taken from figure 2.5 for the same x^* position. Evidently, the compliance of the LES solution is remarkable. The areas where the mismatch occurs seem to be isolated to the jet mixing layers above and below the jet axis. It is natural to expect the three-dimensional mixing layers to exchange momentum in all three directions, which may explain the reason for the slight gain in velocity compared to the planar solution. To get an overall intuition about the mean velocity behavior, we show in figure 4.7 the time-averaged velocity contours in the $\pi/8$ cross-sectional plane of the device. It is substantial to realize the nature of the secondary jets feeding into the major flow chambers. We already alluded to the fact that the main axial jet carries similar characteristics as the two dimensional case since the preponderant length scale affecting the mean flow is the jet width. The major flow jets, however, are more likely to exhibit unique features due to their exposure to energetic three dimensional interactions that are no longer governed by a universal macro-scale. First, we will interpret the time-averaged profiles undergoing expansion in the bottom shear layer as a building block for understanding the transient evolution. Analogous to the two-dimensional analysis of section 2.4.1, figure 4.8 illustrates the vertical velocity $< U_y >$ as obtained from both the LES and 2-D simulations, at three lateral locations extending from the nozzle to the minor flow probe. It can be seen that there are considerable discrepancies between the two solutions. The same reasoning used to explain the streamwise growth of the mixing layers is also applicable here. Of course, we do not believe that the LES predictions in the sliced plane should exactly resemble those of the 2-D simulation. Support for this argument lies in the evidential presence of x- and z-velocity components, not included in the given profiles. Hence, the differences are more likely an outcome of the physics rather than of numerical or model errors in the 3-D calculation. One interesting observation concerning the

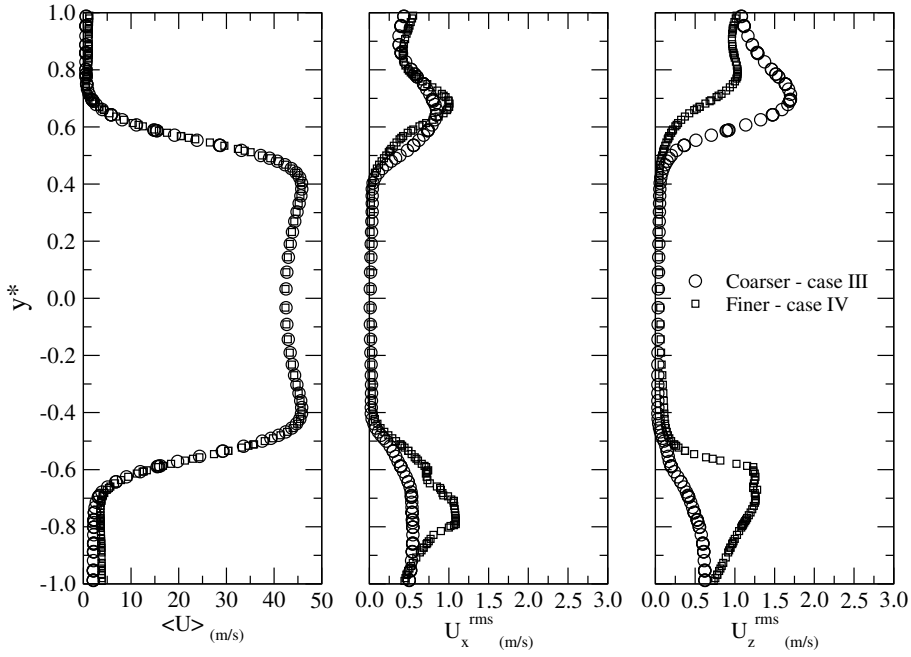

Figure 4.5: Effect of grid refinement on the mean and rms U_x and U_z velocity profiles

major flow jets is the degree of deflection which leads to their impingement once they reach the chamber walls. It is learned from figure 4.7 that a significant amount of velocity magnitude is present in the boundary layers rebounding from those walls. A closer look at this phenomenon and its consequence on the particle transport will be presented in a later section.

The role of the subgrid scale turbulence model in the large eddy simulation of this genre of flow warrants an inquiry. Obviously with the absence of certified experimental data on the fluid phase statistics, it will be difficult to judge the accuracy of any given model. Nevertheless, in the following discussion we shall present some prognostic results concerning the performance of the Lagrangian dynamic and Lilly models. The objective is to demonstrate that the mechanism by which the eddy-viscosity coefficient is computed, is directly responsible for the outcome of the results. Therefore, forecast on the superiority of a certain model will be made based on first

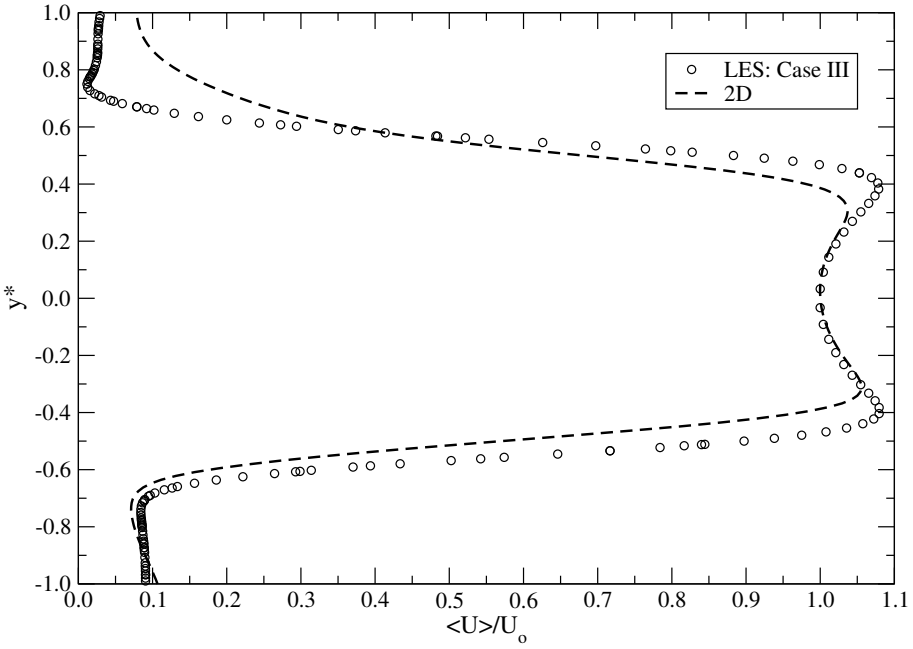

Figure 4.6: Statistical mean velocity profile at jet mid-gap: LES-Lagrangian vs. 2D-Case II

principles and physical arguments. Previously, we previewed the behavior of the Lagrangian model at virtual impaction in relation to the "no-model" two-dimensional solution. Figure 4.9 is a comprehensive representation of the LES time-mean velocity profiles as they transform from the nozzle to the collection probe. The solutions of the two turbulence models are normalized by the same nozzle centerline velocity U_{oo}. It is shown that despite the initial identical lateral footprint at $x^* = 0.25$, the two models predict rather discordant profiles as the flow approaches the collection nozzle. Undoubtedly, the dissipation of the turbulent kinetic energy which is influenced by the magnitude of the dynamic coefficient is not the same. Recall that in the Lilly model C_s is computed via equation (3.13), whereas in the Lagrangian model, equation (3.14) is employed. Figure 4.10 is a clear indicator of the relative scales of C_s at the re-laminarization stage. The constant value used in some LES calculations with the "static" Smagorinski model is also shown for reference. Fortunately, the two

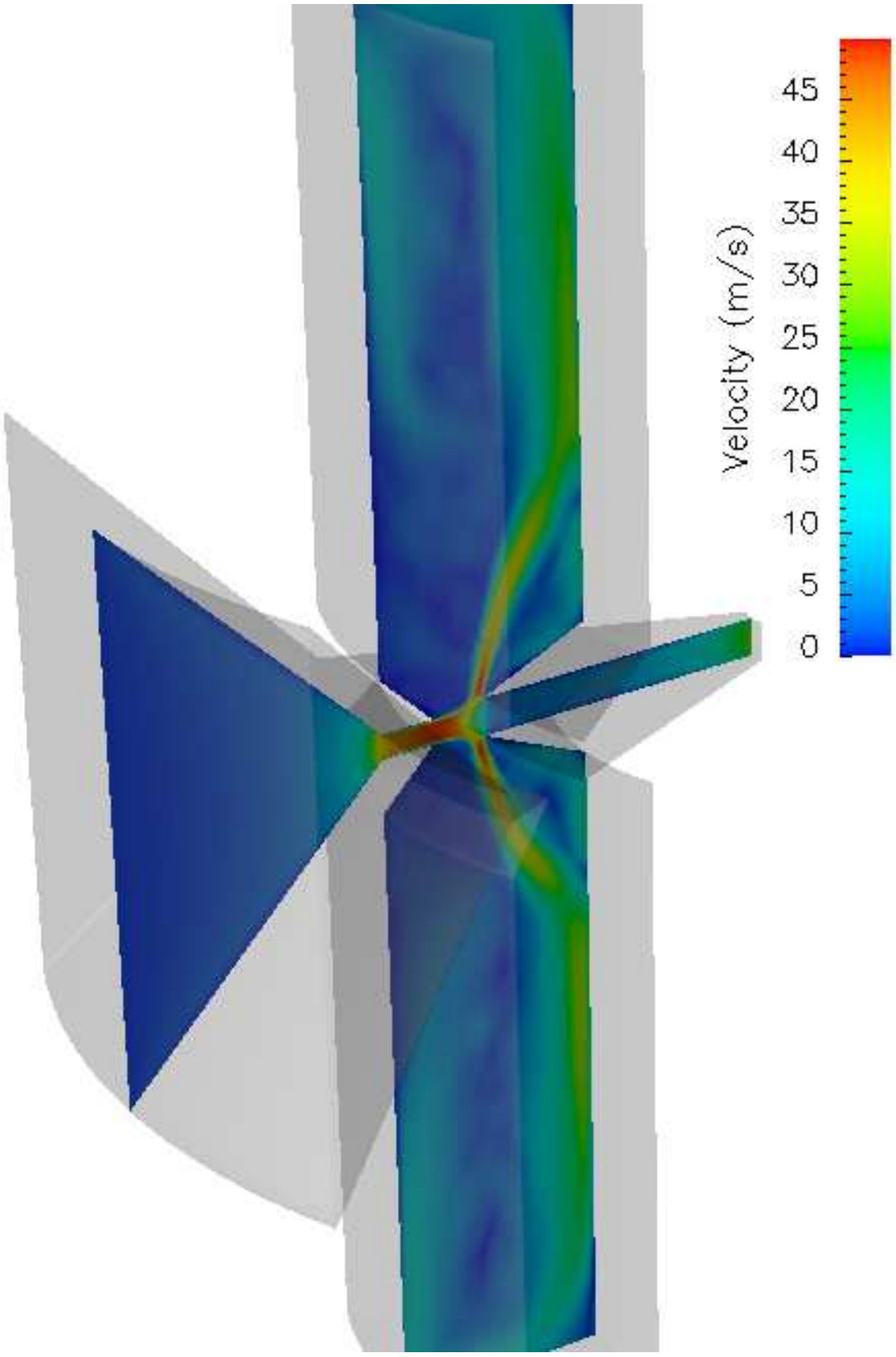

Figure 4.7: Lagrangian dynamic model LES-case III: Mean velocity contours mapped to $\pi/8$ plane

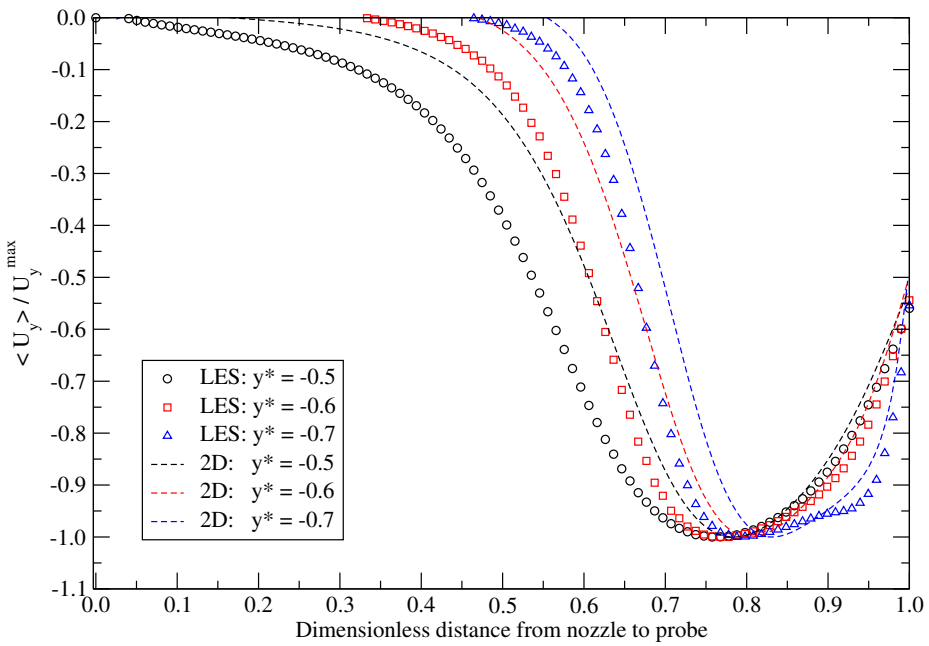

Figure 4.8: Statistical mean expansion velocity profile at nozzle boundary layer: LES-case III vs. 2D-Case II

dynamic models predict correct levels of near zero magnitude in the pseudo-laminar jet column (i.e. $-0.5 < y^* < 0.5$), however, in the mixing layers the maximum value of the coefficient predicted by the Lagrangian model exceeds that of the Lilly formulation by a factor of 4.5, and that of the traditional Smagorinski constant by 1.8. Evidently, the Lagrangian model is more responsive to the dynamics of the flow. Not only is it capable of intersecting with the theoretical constant of 0.1, but it is also mindful of different flow regions that require perhaps lower or higher eddy-viscosity (note equation 3.10). The proper prediction of model constant during transition to turbulence in boundary layers has proved to be a challenging problem [79]. It was shown by other researchers that simple models relying mainly on the Smagorinski relationship with empirical modifications to the model coefficient are not very suitable. One allegation, however, is clear; during the late stages of transition it is commendable that the residual stress model provide some energy dissipation to

replenish the cascade process.

We continue to focus on this issue as we address another section of the device where interesting mechanics are present. The following discussion considers the flow dynamics that accompany the major flow ejection jet. In order to assess the level of turbulence fluctuations and its relation to the model coefficient we approximate the turbulent kinetic energy as

$$K \approx \frac{1}{2} < (u_i^r)^2 >, \tag{4.1}$$

where u_i^r is the velocity fluctuation vector of the *resolved* LES field. Formally, as pointed out in [45], the true turbulent kinetic energy contains additional terms that are inaccessible by LES. Albeit, in an effort to estimate the energy residing in the subgrid scales, we have confirmed that the error in maximum K between the finer and base grid over the entire domain is: $\kappa = (K_{finer}^{max} - K_{coarser}^{max})/U_{oo}^2 \approx 0.01$. In other words, the maximum unresolved energy in the base grid amounts to only 2% of the mean kinetic energy of the main jet. Three sampling locations perpendicular to the inclined expansion bay are monitored, as marked in figure 4.11. Figure 4.12 shows the turbulent kinetic energy profiles at the three designated locations. It is clear that the Lilly model consistently provides higher turbulent kinetic energy levels than the Lagrangian model. Moreover, there appears to be two lateral positions or peaks away from the wall where the turbulent kinetic energy is mostly concentrated. Before we examine the physical reasons for this behavior, we show in figure 4.13 the magnitude of the eddy-viscosity coefficient at the same sampling stations from instantaneous LES fields. It is believed that the modest or relatively low values of the dynamic coefficient in the Lilly model are causing the overshoot witnessed in the turbulent kinetic energy profiles. Essentially, the magnitude of the eddy-viscosity in the Lilly model is too low to provide any significant sub-grid-scale stresses that can effectively diffuse the energy being generated above the grid-filter scale. The Lagrangian model,

on the other hand, can sustain higher values of C_s that soar as high as four times the classical constant. To further decipher the mechanistic differences between the two closure models, we compute the turbulent viscosity using equation 3.10, and the same LES fields whose dynamic coefficients were shown in figure 4.13. Figures 4.14 and 4.15 show instantaneous iso-surfaces of the turbulent viscosity ratio $\nu_T/\nu = 2$ for the Lilly and Lagrangian models, respectively. It is discernible that the instantaneous LES field in the Lilly simulation is poor in its resolution of the eddy-viscosity "blobs", which is strictly an outcome of the insignificant contributions of the SGS dynamic model, since the same grid and numerical algorithms are used for each calculation. Meanwhile, wide regions of the major flow in the Lagrangian computation exhibit such blobs, which signify the extent of the turbulent viscosity relative to the molecular viscosity. Clearly, a favorable advantage is gained from the Lagrangian model, especially if we wish to educe the nature and role of the coherent structures. The time-averaged turbulent kinetic energy field from the Lagrangian LES is mapped in figure 4.16 for the $\pi/8$ plane. As mentioned earlier, the behavior of the secondary jets is of concern, due to the centralization of the highest kinetic energy near the wall. A sampled profile in the middle of the expansion edge is shown in figure 4.17, for the mean velocity as well as the kinetic energy. In light of such results, and recalling the contours of figure 4.7, it is evident that the turbulent kinetic energy is distributed around the maximum velocity inclined-jet-axis. This, in fact, leads to the dual stream of kinetic energy concentration witnessed in the contours of figure 4.16. Incidentally, it is also the location where the highest r.m.s. *vorticity* fluctuations are present. It is presumed that such a peculiar deportment is an outcome of the shear layer vortical structures, and the consequential turbulence interactions near the wall, which in turn feed back to the bulk flow in the chambers. For reasons mentioned above, and to guarantee proper resolution of the coherent structures, the upcoming discussion of large eddy dynamics will be performed using the results of the Lagrangian dynamic model.

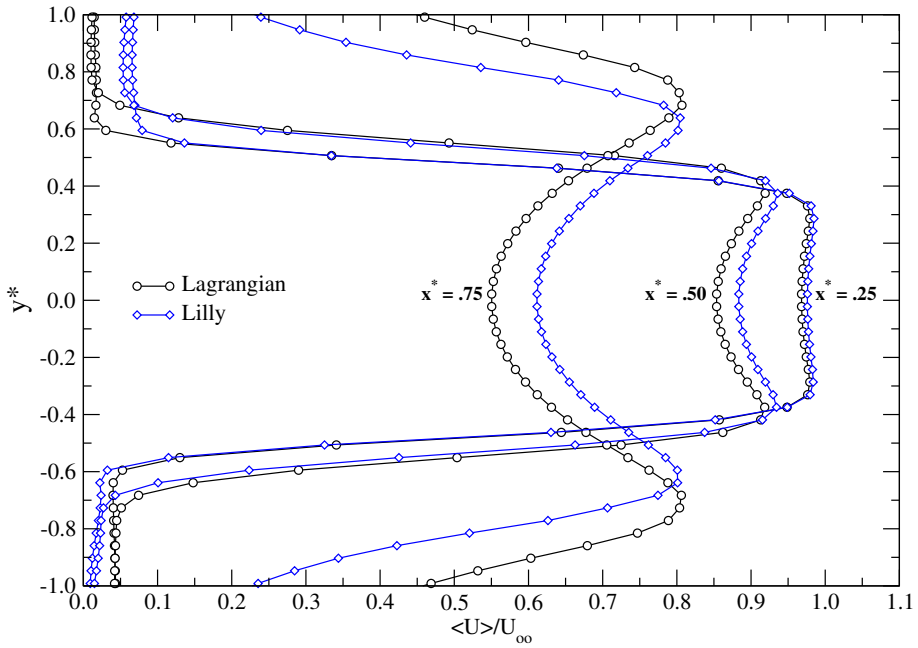

Figure 4.9: Statistical mean velocity profile during virtual impaction: LES-Lagrangian-case III vs. LES-Lilly-case II

4.3 Free Boundary Layer Properties

The structural features of the three-dimensional shear layers issuing from the secondary jets of the major flow are analyzed in this section. In section 2.4.3 we performed a rigorous analysis on the evolution of the two-dimensional vortical structures. In retrospect, the 2-D visualizations allowed us to identify the *mirrored* Kelvin-Helmholtz instability associated with the detachment and growth of coherent eddies in the separating shear layers. The next logical step, of course, is to seek an understanding of this mechanism in three dimensions. Hence, using the LES fields of the Lagrangian model (case III), the fluid mechanical properties of the 'free boundary layer' are examined. It is imperative, however, to realize that the large eddy simulation field does not resolve all the scales of motion, which means that some of the small-scale fluctuations, or certain types of eddies described in the 2-D study will

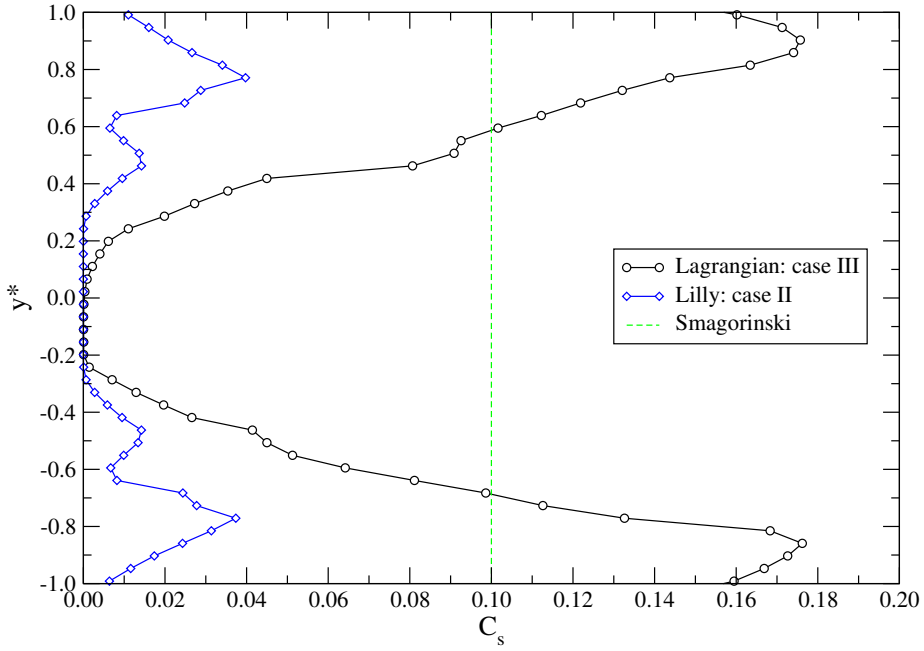

Figure 4.10: Instantaneous eddy-viscosity coefficient in virtual impaction gap at $x^* = 0.75$ and $\pi/8$ plane

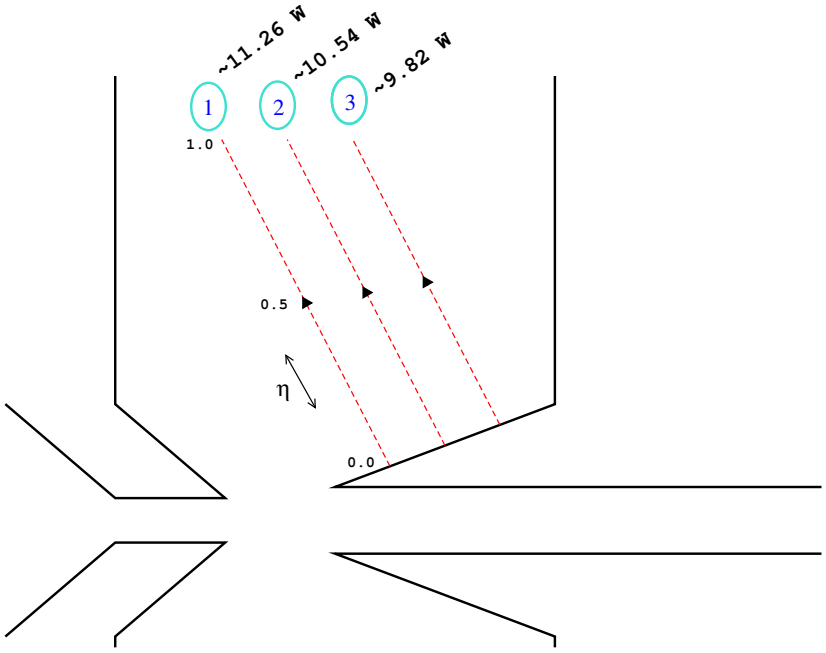

Figure 4.11: Location and length of major flow jet sample lines in the $\pi/8$ plane

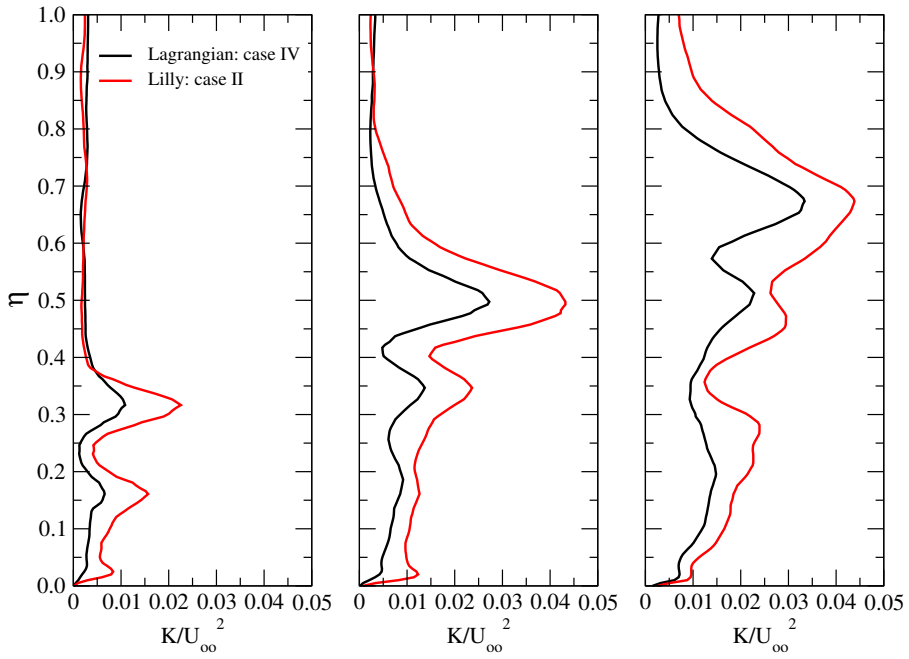

Figure 4.12: Time averaged kinetic energy of the fluctuating velocity field of major flow jet on sample lines 1 to 3 in figure 4.11 from left to right

not be present. Nevertheless, the discussion will focus on the nature of the resolved motions. The premise of any complex flow analysis lies in deciphering its vorticity dynamics. Figure 4.18 is a visualization of the 3-D vortex sheets created by the cross-flow jet, in an average sense. The iso-surface is computed from the regions of the time-mean field possessing $\sim 55\%$ of the reference jet value $\Omega_o \equiv \frac{U_j}{W/2}$. As shown, there are two distinguished types of shear layers. The upper layer is an outcome of the deflecting jet, and its origin can be traced to the boundary layer in the throat of the nozzle. The lower shear layer is a child of the leading edge boundary on the opposite end of the nozzle. To further characterize this behavior, we plot in figure 4.19 the non-dimensionalized vorticity and velocity profiles at the same oncoming sampling line of figure 4.11. Evidently, the vorticity rich layers are not aligned with the core of the emerging jet, but are segregated on either side of its main thrust axis. This result leads us to believe that the coherent structures of the unsteady realizations,

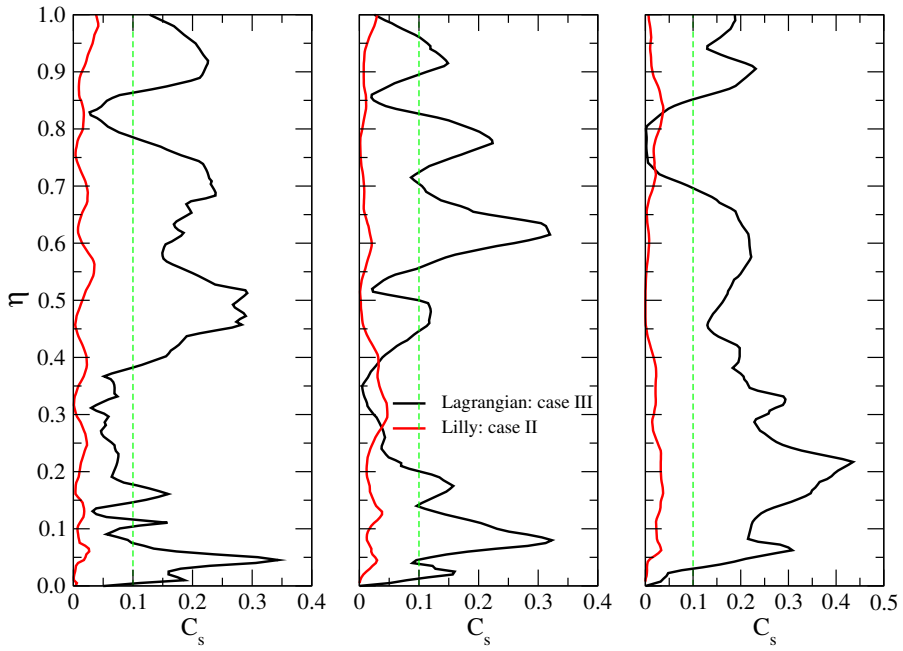

Figure 4.13: Instantaneous eddy-viscosity coefficient of major flow jet on sample lines 1 to 3 in figure 4.11 from left to right

which are paraded by the so called *wake vortices*, are not shed from the jet but are foiled from vorticity brought to bear by the free boundary layers. In fact a similar finding by Fric & Roshko [28] is documented for the unbounded jet-in-crossflow. It is also interesting to note the difference in vorticity magnitude and thickness among the distinct shear layers. The upper agglomeration has a thickness that is comparable with the jet width ($\delta \approx .95W$), and its maximum magnitude does not exceed Ω_o, whereas the lower layer's thickness is $\delta' \approx 0.8W$, thus admitting higher maximum vorticity. Before we consider some instantaneous revelations of the vorticity field, we shall attempt to address the degree of turbulence anisotropy. Figure 4.20 depicts the root mean square x-velocity fluctuations in the lower shear layer extended between the nozzle lip and the minor flow entry point. A similar plot for the rms z-velocity is shown in figure 4.21. The three vertical positions where the profiles are sampled cover the $\pi/16, \pi/8, \& \ 3\pi/16$ rotated planes of the cylindrical domain. As can be

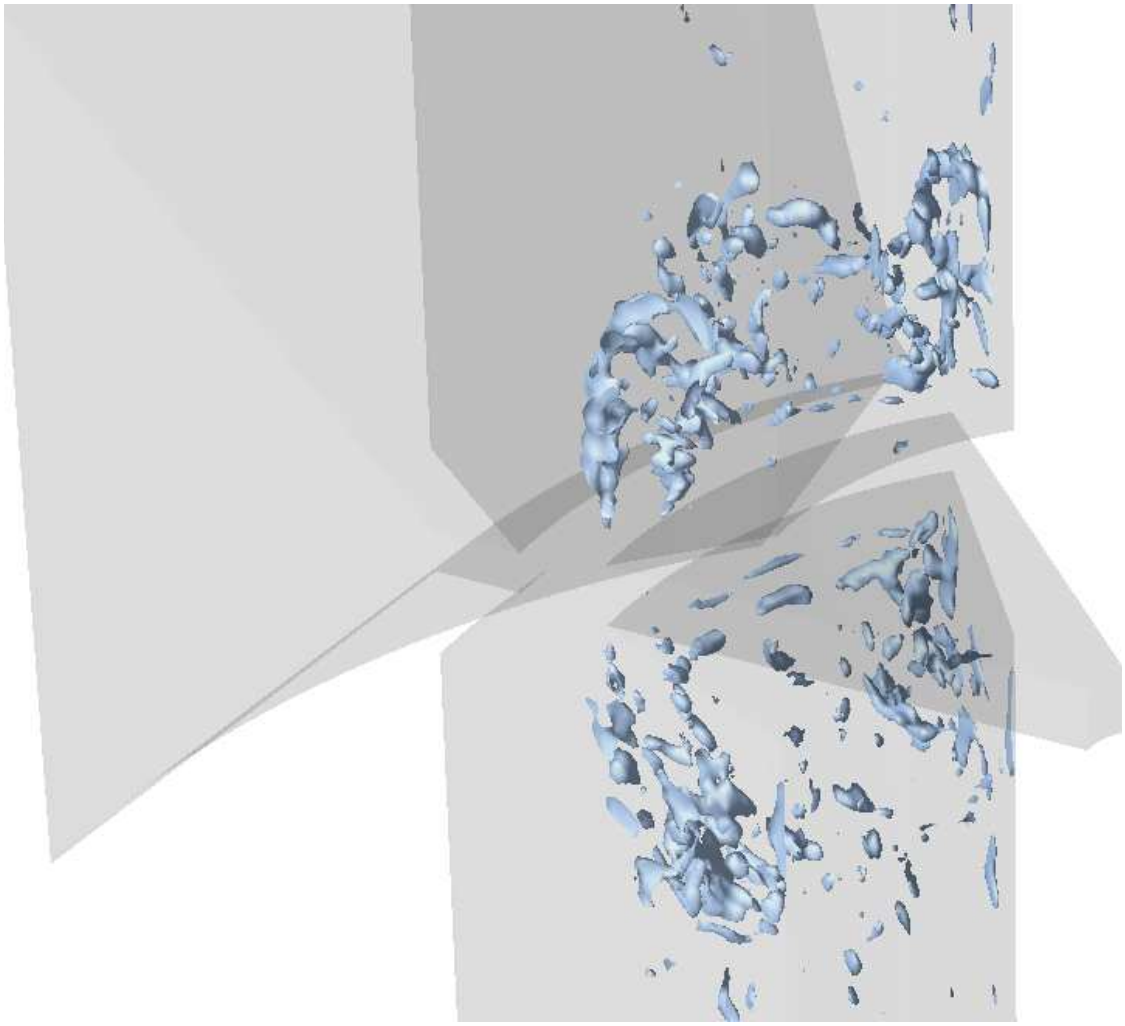

Figure 4.14: Lilly model LES:case II isosurfaces of instantaneous subgrid turbulent viscosity ratio = 2.0

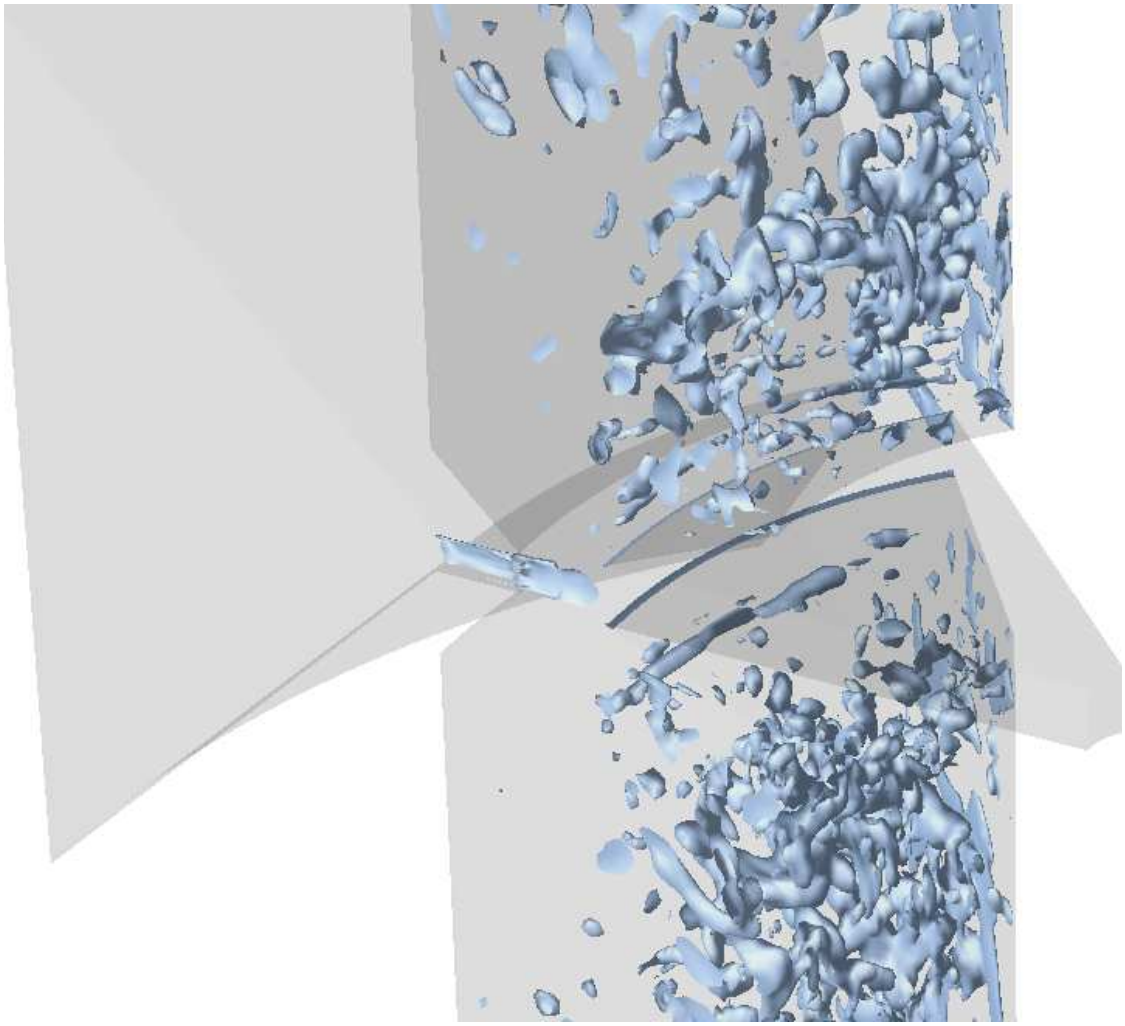

Figure 4.15: Lagrangian model LES:case III isosurfaces of instantaneous subgrid turbulent viscosity ratio = 2.0

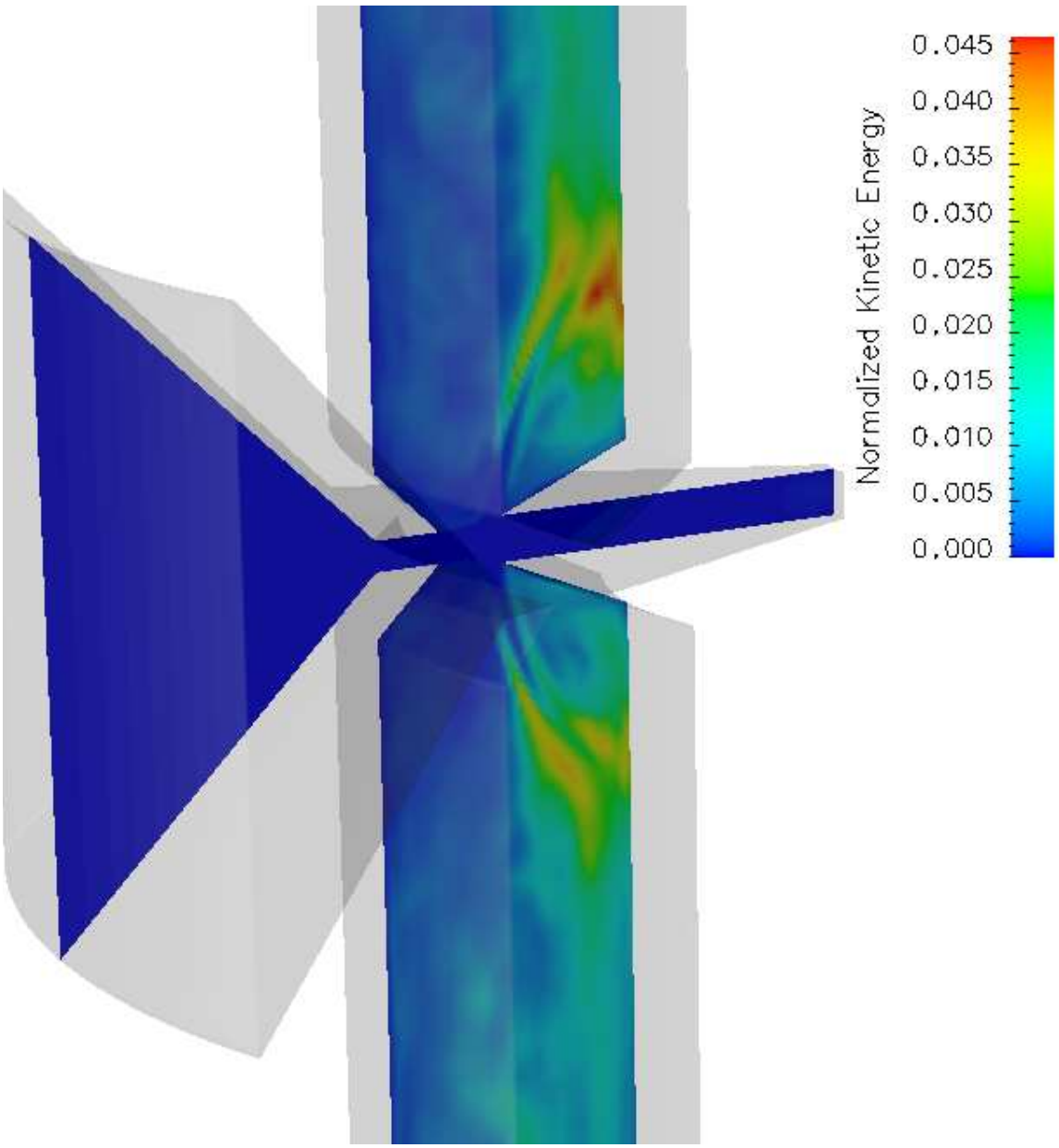

Figure 4.16: Lagrangian model LES: case IV time-averaged kinetic energy contours mapped to $\pi/8$ plane and normalized by U_{oo}^2

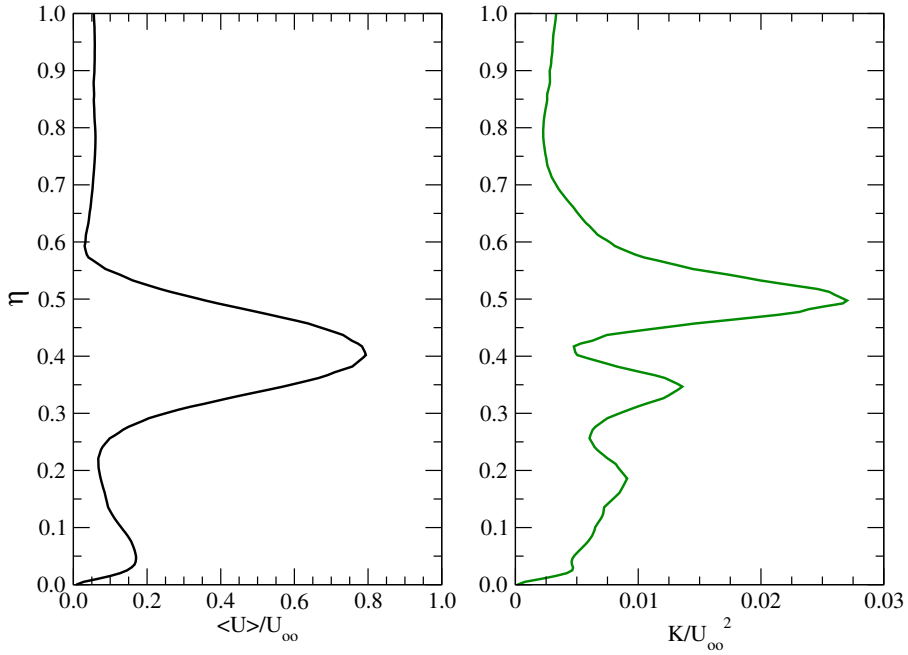

Figure 4.17: Lagrangian model LES:case IV time-averaged normalized velocity magnitude and turbulent kinetic energy across major flow jet - middle sample line 2 in figure 4.11

seen, the growth of the turbulent activity across all angles begins modestly in the most inner shear layer at $y^* = -0.5$ (height of nozzle wall). The fluctuations then in turn increase substantially as we go further down to $y^* = -0.6$ and $y^* = -0.7$, in other words deeper into the separated shear layer. Surely, the mixing between the high speed jet and the low speed fluid in the cavity is the breeding ground for such turbulent intensities. Concerning the anisotropy of the turbulence, which quantitatively amounts to roughly 2% of the mean jet velocity in the x and z directions, it is apparently dependent on the angular location within the flow. It must be pointed out that the maximum fluctuation levels in the y-direction are negligible ($\approx 0.6\%$ of U_{oo}). It is observed that in the middle plane at $\pi/8$, the rms velocities are slightly less than their counterparts near the periodic boundaries. As a consequence, the variation among the individual rms velocity components at the different angles is a testament to the hetrogeneous nature of the separation events, and eddy formation sequences that give rise to the observed turbulence.

Notably, the time-averaged results of the large eddy simulation can illuminate some of the dominant physics of the flow, however, the fascinating insight provided by the unsteady phenomena is uniquely rich. To this end, we focus our attention hereinafter to the developmental attributes of the coherent structures which can only be educed from *instantaneous* fields. Figure 4.22 shows instantaneous contours of the x-vorticity magnitude mapped to the $\pi/8$ slice, and normalized by Ω_o. Similarly, figures 4.23 and 4.24 are of the y- and z- vorticity component at the same timestep, respectively. To facilitate the identification and role of the different interactive events, we categorize **five** key structures as the main drivers of vortex maneuvering. Based on the labels shown in figure 4.22, table 4.4 summarizes the critical structures:

The primary sources of vorticity as alluded to previously are the curved shear layers emanating from the virtual impaction jets. First, the upper free boundary layer 'A' is

Label	Name
A	upper free boundary layer vorticity source
B	lower free boundary layer tearing-edge vorticity source
C	circulatory wall-born vortices
D	wake vortices
E	rebound wall-born vortices

Table 4.4: Critical vortical structure identification

an extension of the originally thin vorticity layer in the throat. This consistent fluid structure contains significant contributions of both x- and z-components of vorticity. Recall that we also symbolized the mean thickness of this layer by δ in figure 4.19. Obviously, the same behavior is observed in the lower section of the main jet (also labeled 'A'), where the parallel layer possesses equal vorticity magnitude but opposite in sign. Using the right hand rule, the top layer 'A' undergoes rotation in the counter-clockwise direction, while negative vorticity in the bottom layer 'A' implies clockwise rotation. Second, the free boundary layer 'B' occurs on the lower brink of the major flow jet on either side of the nozzle due to the tearing or slashing action of the sharp wall-edge. These layers whose mean thickness was characterized by δ', rotate in a direction that is opposite to their companion 'A' layers.

In an unsteady oscillatory motion, the free boundary layers begin to deform, twist, and bend, thus producing a streak of centrifugal concentrations of vorticity called wake vortices, that carry the 'D' label. These eddy like structures seem to captivate higher magnitudes of z-vorticity, judging by the scale of the contour levels. The convection of the wake vortices away from their roots leads eventually to their impact on the side walls of the major flow chamber. Evidently, the complex mechanics by which this occurs is difficult to describe, however, a clear outcome of such events is the emergence of tube like structures that are aligned with the vertical axis. The fact that we observe high concentrations of y-vorticity near the wall in figure 4.23 attests to the cogency of this argument. Moreover, the structure labeled 'E' in figure 4.22 is

a byproduct of the wall impaction event. Finally, the last type of primordial vortices 'C' are the ones generated near the expansion bays beneath the 'B' shear layers. The circulation bubble formed on the bayside of the expansion slot is highlighted in figure 4.25, which shows the velocity vectors in the plane at the same instant as the vorticity contour plots. The wall-born eddies take on the task of disrupting the 'B' layers, which can result in a more forcible shedding activity. The velocity vectors plot also reflects the rebound nature of the type 'E' vortex. It is shown that the eruptions of 'E' structures are forcing a breakup in the streamlines of the major flow jet.

To investigate the three-dimensional characteristics of the coherent structures, a new mathematical quantity must be introduced. A well-known eduction scheme based on the second invariant of the velocity gradient tensor is employed [80]. The Q-criterion is defined by

$$Q = \frac{1}{2}(\overline{\Upsilon}_{ij}\overline{\Upsilon}_{ij} - \overline{S}_{ij}\overline{S}_{ij}), \tag{4.2}$$

where $\overline{\Upsilon}_{ij}$ and $\overline{S}_{ij}$ are respectively the resolved rate-of-rotation, and rate-of-strain tensors. It is then straightforward to argue that the regions of the turbulent flow where Q is positive must mark the fluid elements whose rotation outweighs their strain. Figure 4.26 is a representative picture of the types of eddies that can be visualized by the Q-criterion. We set the iso-surfaces value to be 20% of ${\Omega_o}^2$, in order to isolate the 'D' type wake vortices extruding from the 'B' layer. Note that Q can also be recast in terms of the vorticity modulus:

$$Q = \frac{1}{4}(|\Omega|^2 - |S|^2). \tag{4.3}$$

Using the illustration in figure 4.26, we are able to educe the shape and size of the tube-like structures emanating from the lower free boundary layer 'B'. Evidently, such structures possess higher rotation strength than the ones emanating from the upper

free boundary layer 'A', since the latter is not visible. If we reduce the iso-surface threshold value to 10% of ${\Omega_o}^2$, as depicted in figure 4.27, the type 'A' structures begin to appear. It is remarkably clear that the eddies of the wake vortices originate as thin straight tubes, but quickly become amenable to re-orientation as they travel downstream in the major flow chamber. This is particularly visible in the helical "piped" structures which grow extensionally along the spanwise direction. The vertical alignment which is caused by the stretching of the vortices near the walls is also evident. Figure 4.28 is another manifestation of the same structures but colored with pressure so that to accurately mark the core of the vortical agglomerations. From this figure we are able to ascertain that the eddies, despite their similar physical characteristics, can still be associated with asymmetrical regions of the flow that possess different magnitudes of pressure and velocity. The inspection of transient animations also allows us to identify a new set of processes that are hard to capture from still images. For instance, the ability to coagulate two smaller longitudinal tubes to form a larger paired structure is witnessed near the impaction area of the major flow jet. Naturally, the occurrence of such events is closely tied, at least in their earliest stage, to the type 'E' vortices identified earlier. In the next section, we will consider the motion of the discrete particles, and accordingly scrutinize the influence of the discovered coherent structures on their transport mechanics.

4.4 Particle Transport

4.4.1 Description of Wind Tunnel Experiment

Before we interpret the outcome predictions of each model, a brief description of the experimental facility is chartered. The device was tested in a laboratory wind tunnel having a $3' \times 3'$ cross-section. The blower parameters were set to produce a wind velocity of 5.0 MPH (or 2.24 m/s). The aerosol was generated from a "multi-jet"

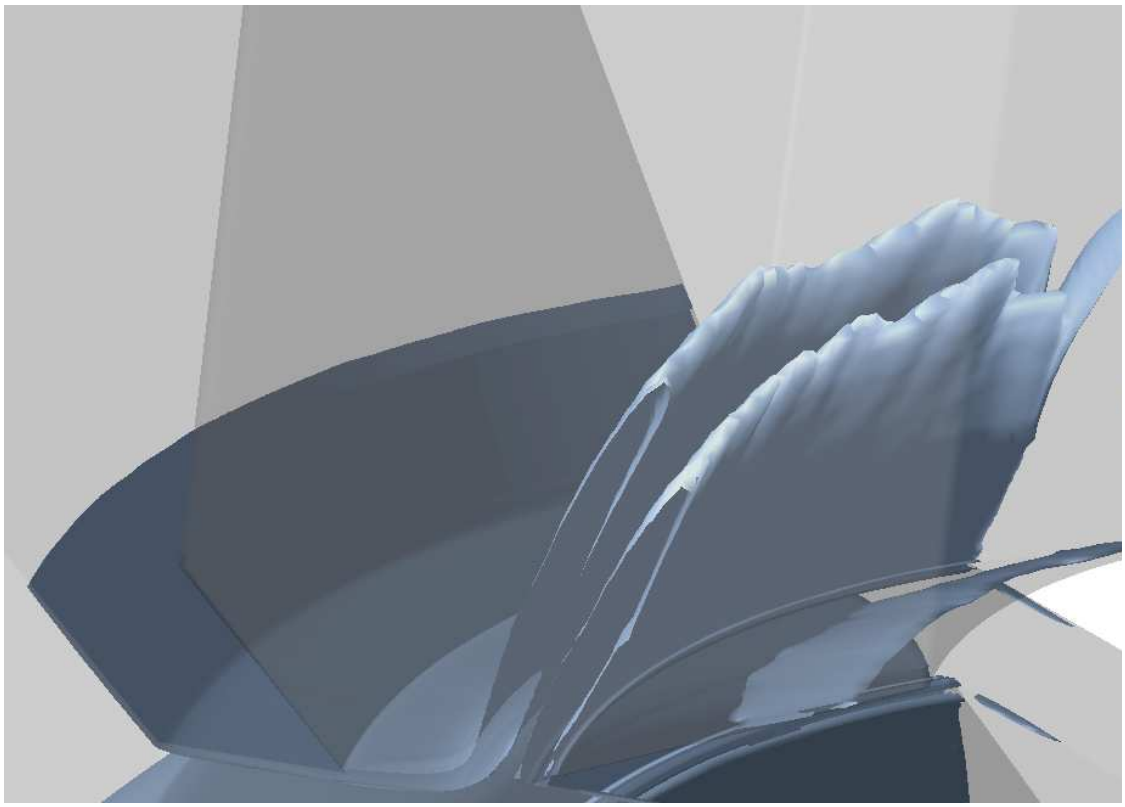

Figure 4.18: Lagrangian model LES:case III isosurface of time-averaged vorticity modulus $|\Omega| = 0.55|\Omega_o|$, shown for the nozzle section

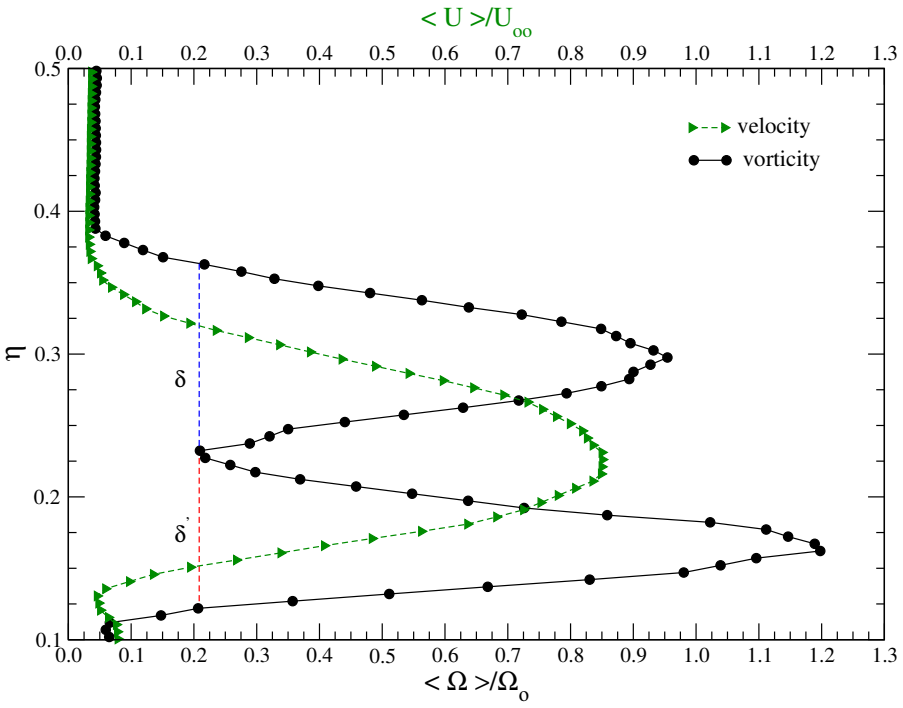

Figure 4.19: Lagrangian model LES:case III normalized time-averaged 3 components of velocity & vorticity showing thickness of dual vorticity layers - sample line 1 in figure 4.11

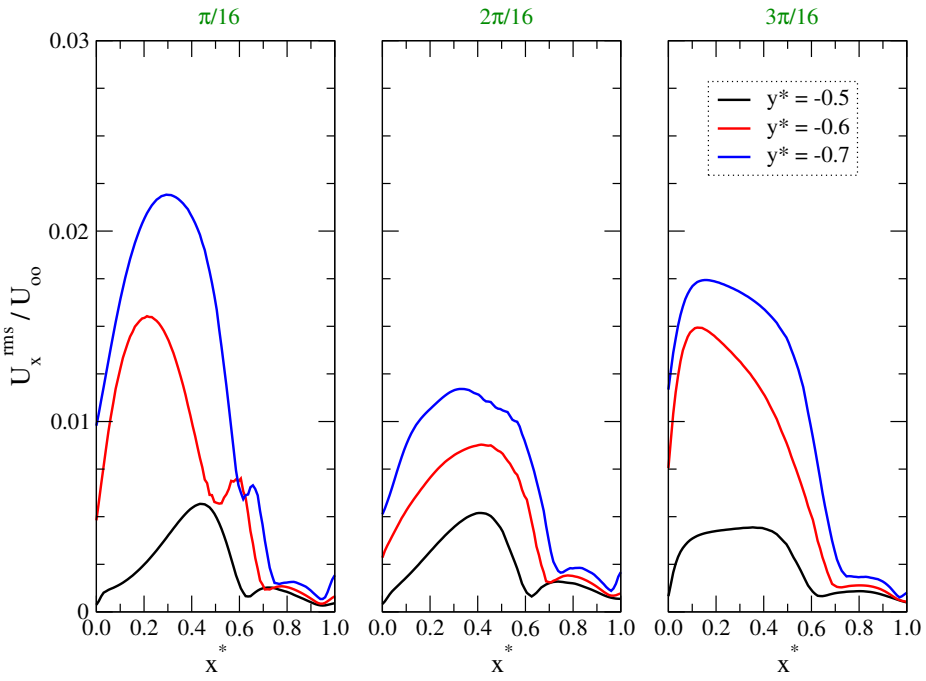

Figure 4.20: Lagrangian model LES:case IV U_x^{rms} profiles at three rotated angles within the free boundary layer

collision nebulizer that is fed from an oleic acid solution, and positioned roughly 25 feet upstream of the device. The shooting stream of the nebulizer was focused onto a household fan blowing in the opposite direction of the wind in order to maximize the degree of perfusion. Some quantitative attempts were made to insure uniform distribution of the aerosol downstream. The device, on the other hand, was connected to vacuum motors controlled by electronic knobs that alter the flow rates of each of the minor and major flow, and monitored by pressure drop gauges. The pressure drop of the major flow predicted by the simulation amounted to $\sim$ 1500 Pa, which is very close to what the experiment utilized. The minor flow tube was also connected to a digital aerodynamic particle sizer (APS) (see figure 4.31), the measurements of which constitute the data sets presented herein. Basically, the APS acts as a particle counter, thus displaying the number of sampled particles for each size bin. The separation efficiency is then computed as the ratio of number concentration in

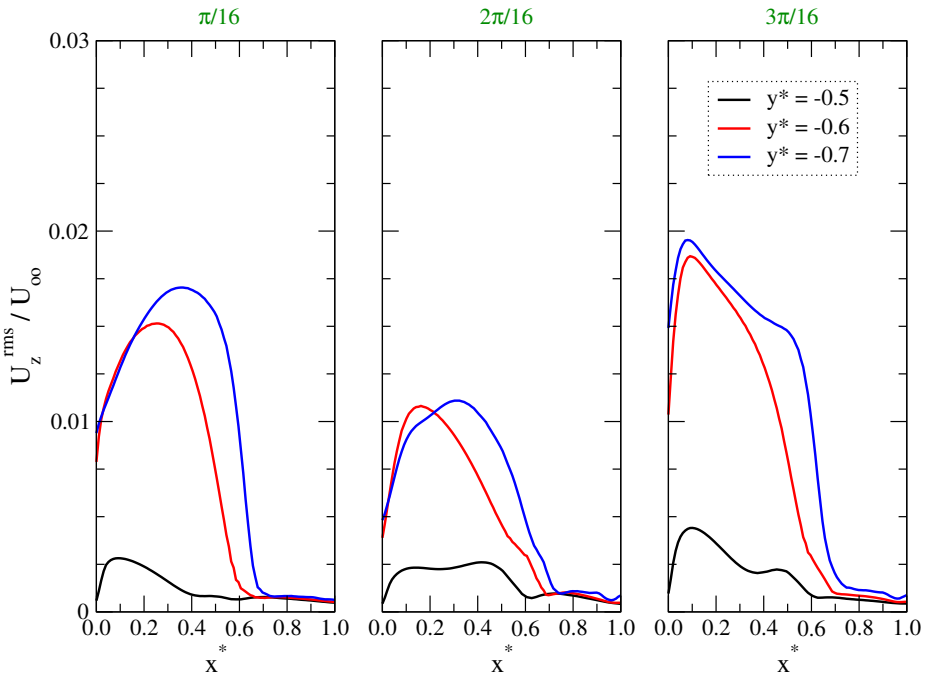

Figure 4.21: Lagrangian model LES:case IV U_z^{rms} profiles at three rotated angles within the free boundary layer

the minor flow relative to a reference ambient reading.

4.4.2 Efficiency Characterization

The aim of analyzing the fluid mechanical properties of the complex flow inside the virtual impactor is strongly conjugated by the need to understand the behavioral properties of the aerosol particles being transmitted by this flow. As a first step in that direction, we shall consider the ability of the LES fields to relay the particles across the virtual impaction gap, and consequently assess the separation efficiency. Analogous to the routine of section 2.4.2, we compute the trajectories of mono-disperse samples of particles released in the circumferential throat section. Approximately 276,000 particles were used for each size injection. Compared to the 2-D simulation, the randomization algorithm that assigns the starting positions is modified such that less particles are distributed in a given plane, and more particles are packed in the

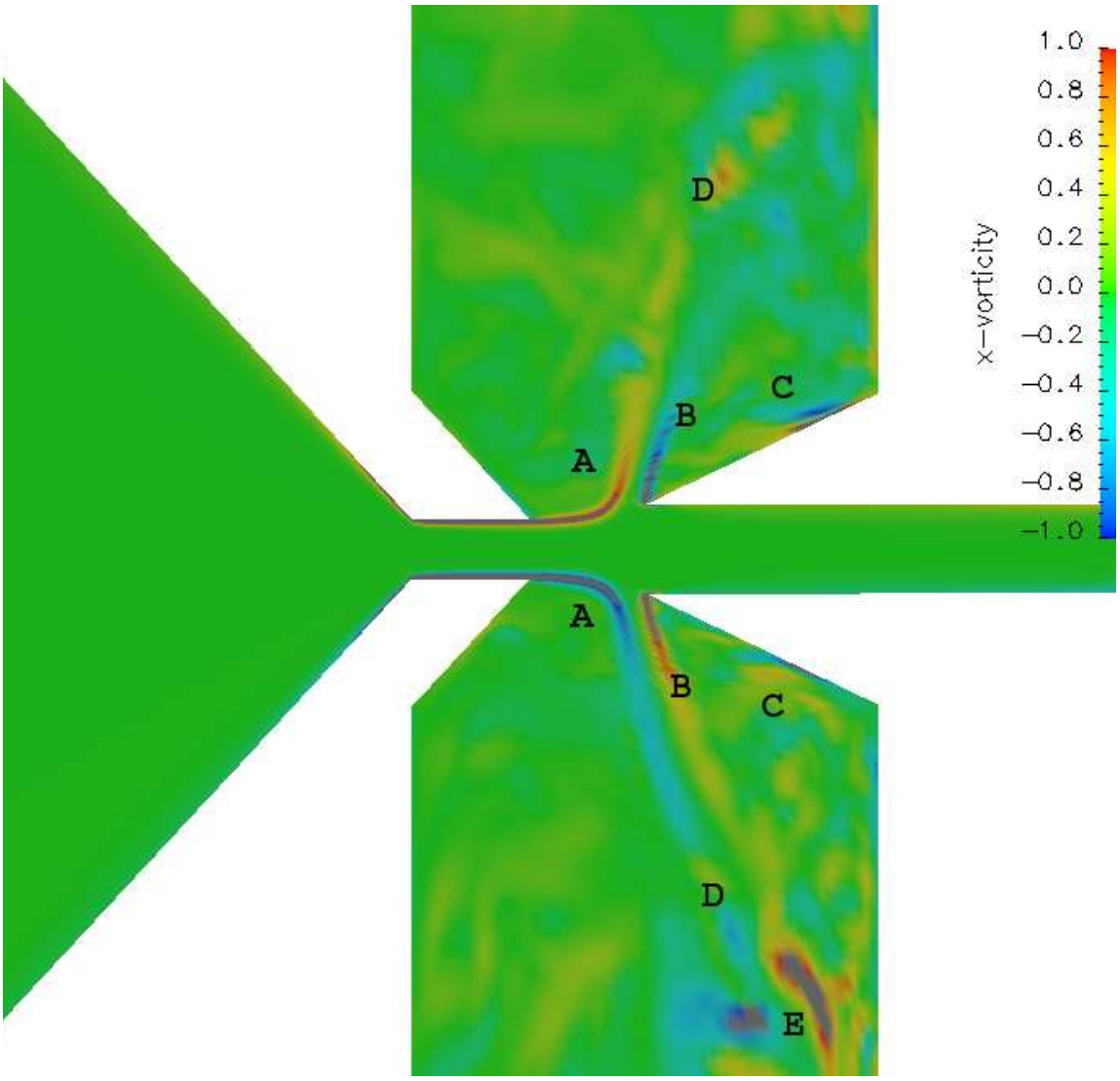

Figure 4.22: Lagrangian model LES:case III instantaneous x-vorticity (Ω_x) contours mapped to $\pi/8$ plane, normalized by Ω_o

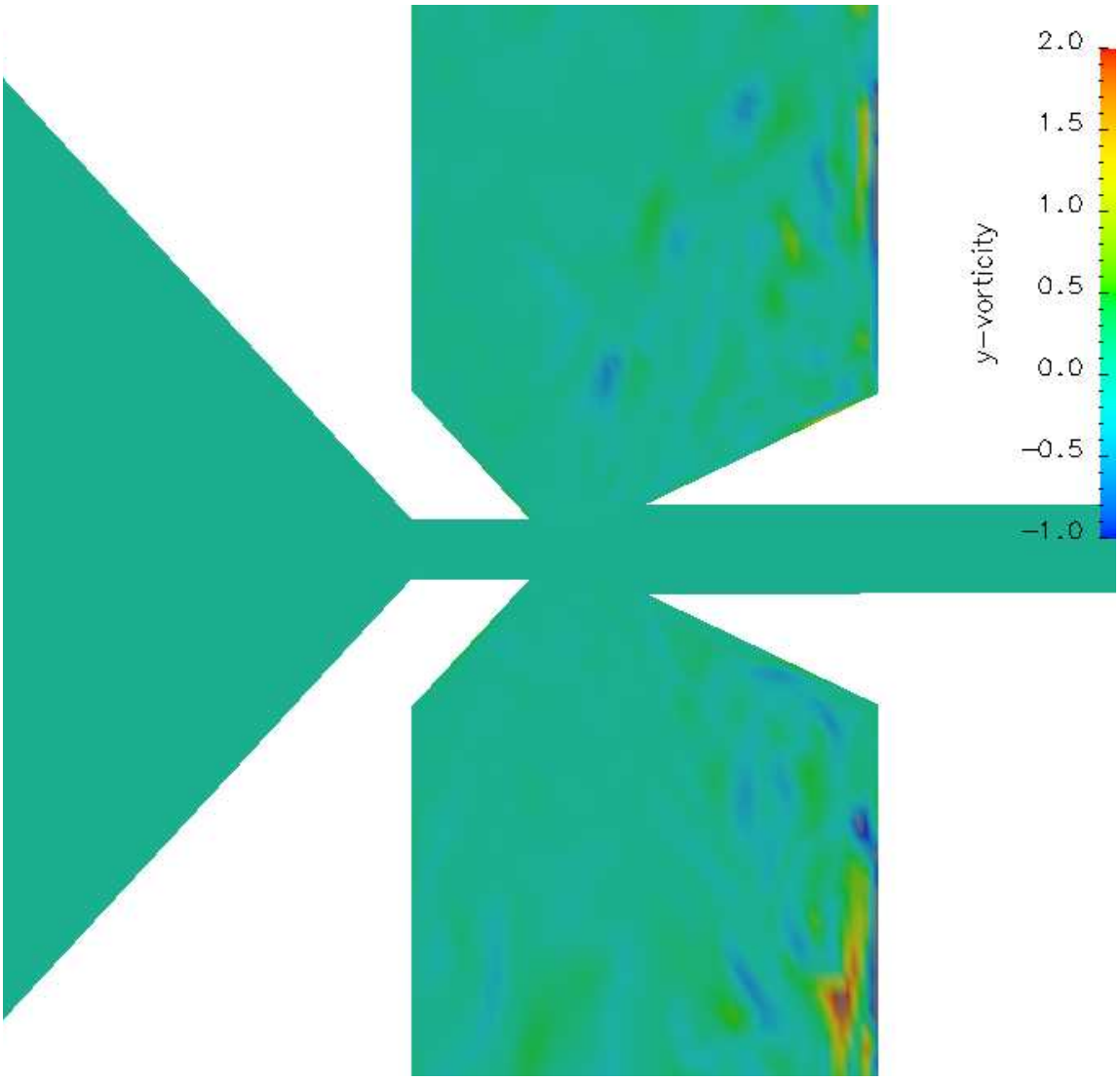

Figure 4.23: Lagrangian model LES:case III instantaneous y-vorticity (Ω_y) contours mapped to $\pi/8$ plane, normalized by Ω_o

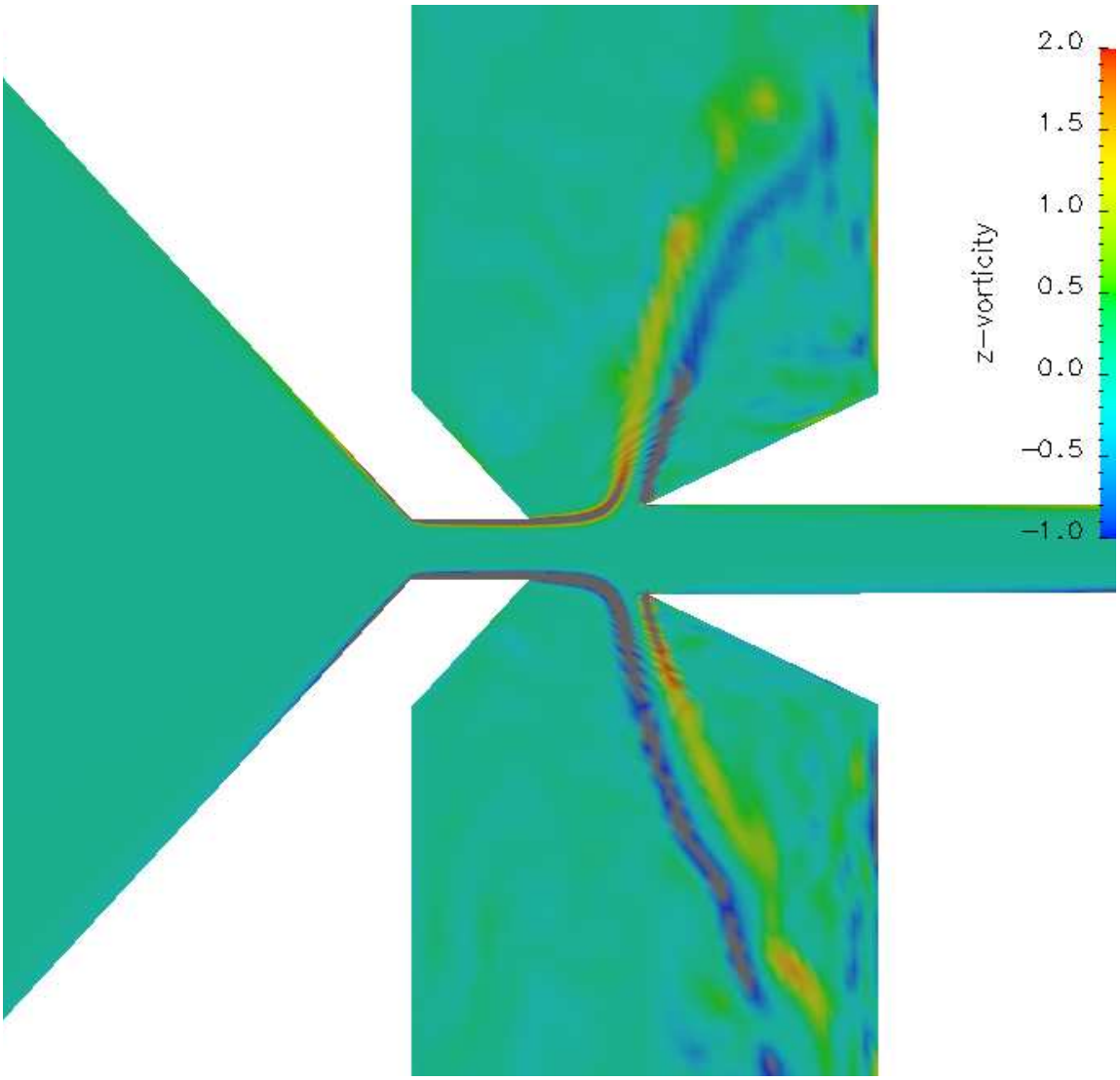

Figure 4.24: Lagrangian model LES:case III instantaneous z-vorticity (Ω_z) contours mapped to $\pi/8$ plane, normalized by Ω_o

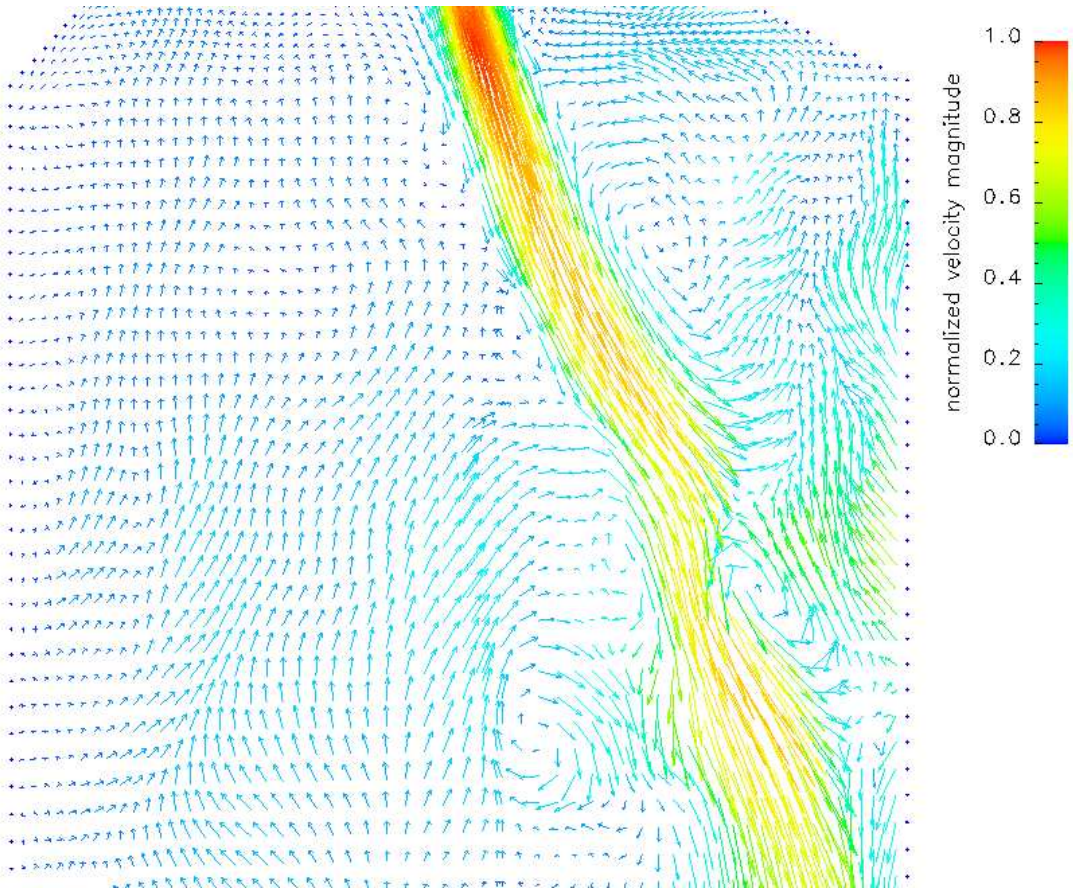

Figure 4.25: Lagrangian model LES:case III instantaneous velocity vectors mapped to $\pi/8$ plane, normalized by U_{oo}, shown for the lower major flow chamber

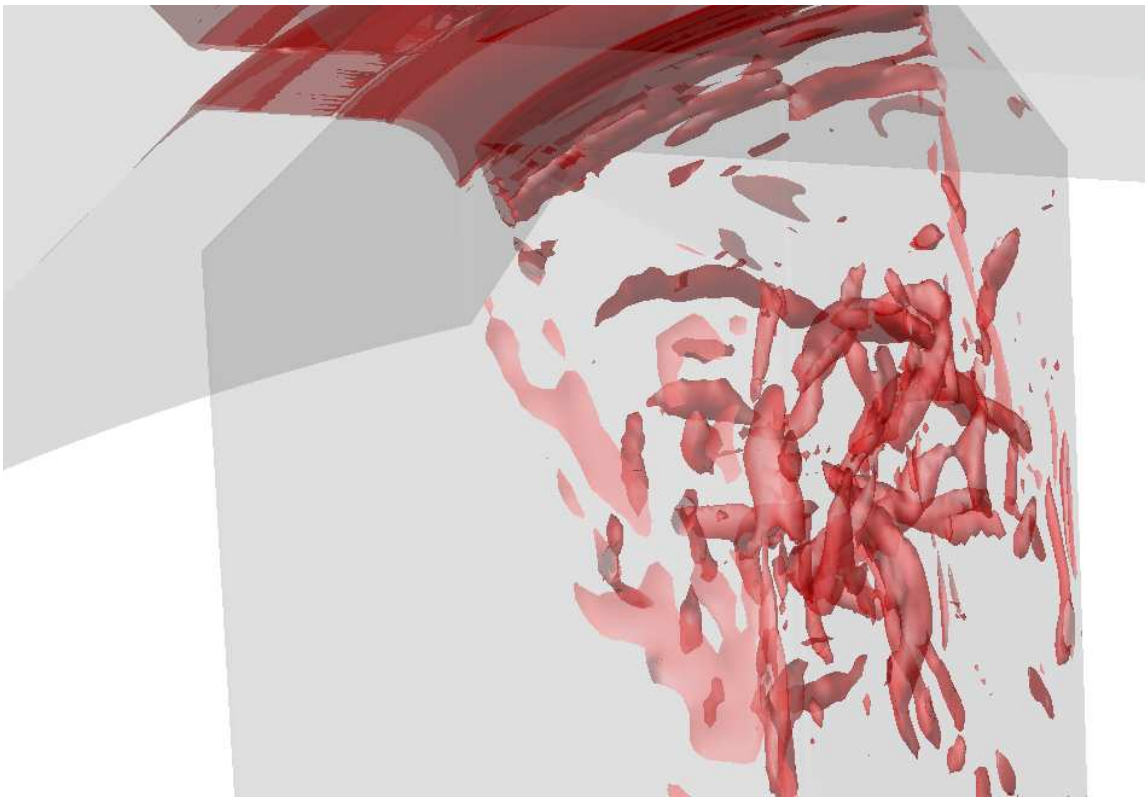

Figure 4.26: Lagrangian model LES:case III instantaneous isosurfaces of $Q = 0.2{\Omega_o}^2$, shown for the lower major flow chamber

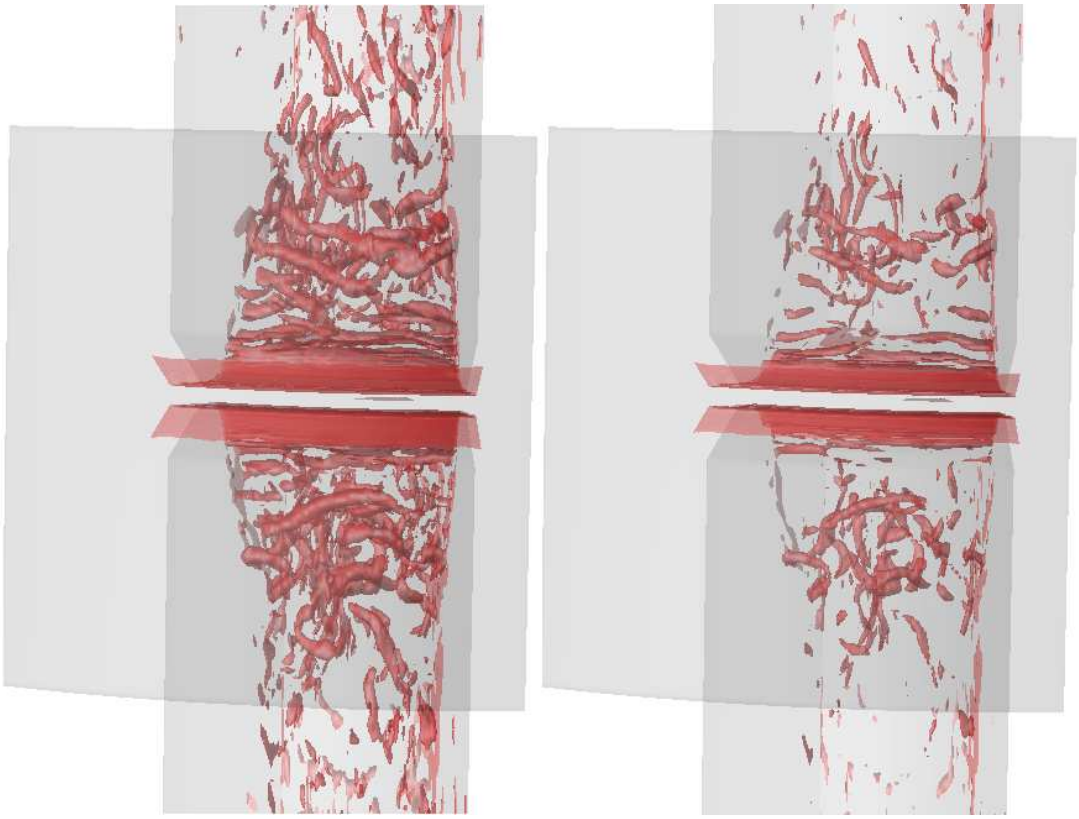

Figure 4.27: Front view: instantaneous isosurfaces of: $Q = 0.1{\Omega_o}^2$ (left), and $Q = 0.2{\Omega_o}^2$ (right), shown from an outer perspective of the entire domain (*inflow is into the paper, separation occurs laterally*)

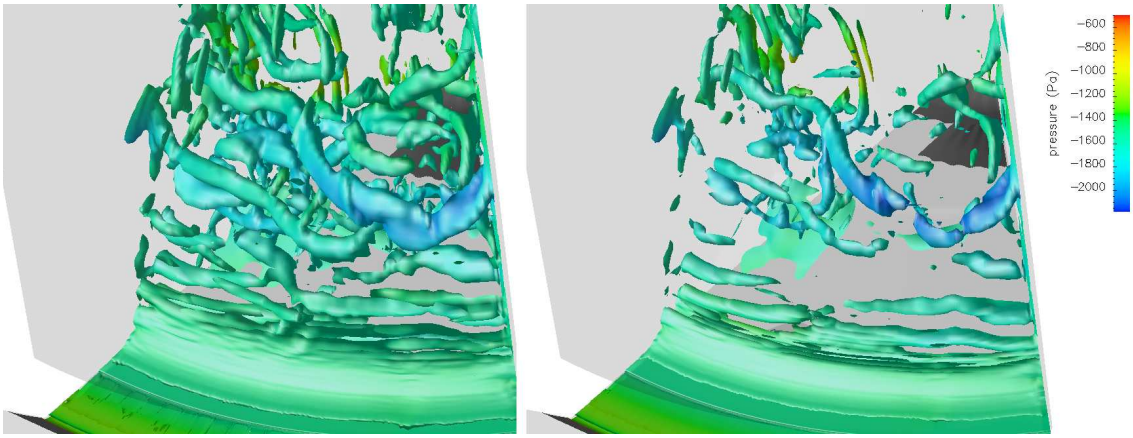

Figure 4.28: Top view: instantaneous isosurfaces of: $Q = 0.1{\Omega_o}^2$ (left), and $Q = 0.2{\Omega_o}^2$ (right) colored by gauge pressure, zoomed view of the upper nozzle issuing into the major flow

spanwise direction. Using the time-averaged field of the Lagrangian model LES (case III), and that of the Lilly model (case II), the particle equation of motion is integrated forward in time until the particles exit the major flow outlets. A sample pictorial of the individual *mean* paths followed by the particles is shown in figure 4.29 for two representative initial stations. At the end of each run, the separation efficiency (equation 2.18) is recorded. The results obtained from this calculation are then plotted for each discrete particle diameter and shown in figure 4.30, along with the prior 2-D results, and the preliminary experimental data [81].

The experimental data points in figure 4.30 were obtained for a minor-to-total flow ratio of 0.10, and 0.15, and were accumulated over trials that sample air for a number of minutes. Granted that the experiment conveys the real trends of particle collection, it can be argued that the LES results attained by the Lagrangian dynamic model are the most suited to reflect such behavior. First, we can see that the 2-D simulation predicts rather unrealistic or excessive penetration for the larger particles. This is most reasonably an outcome of the *idealized* and constrained two-dimensional flow field. The efficiency curve given by the Lilly model LES, appears to also exaggerate the separation. We believe that the increase in velocity prediction witnessed in figure 4.9, is the primary factor that leads to this disparity. Concerning the slight discrepancies among the Lagrangian model predictions and those of the experiment, we can think of two reasons that can explain the mismatch. First, aside from the lack of confidence or error levels that quantify the aerosol distribution measurements, it seems that the simulation data points resemble an experiment that could have been performed at a different Q_m/Q_T ratio. The justification stems from the fact that, to a large extent, we observe the *numerical* data points to lie in between the two experimental curves. It is highly plausible that inconsistencies in the laboratory equipment affected the setting of the fractional ratio. Second, the density of oleic acid is reported to lie between $0.895 - 0.947\ g/cm^3$, and no attempt was made to

measure the density of the aerosolized droplets in the wind tunnel. The simulation, however, is conducted with a constant density equating that of Polystyrene Latex particles (1.047 g/cm^3). The slightly larger value of the theoretical calculations, gives the same size particles additional inertia, thus increasing their penetration capacities, which may explain the reason for the vertical shift in the simulation plot relative to the $Q_m/Q_T = 0.1$ experimental data points. Furthermore, wettability considerations that are presumably present in the experiment, are not taken into account by the simulation. Another possible explanation for the disparity in the results of the two LES models is presented in the following paragraph.

The remaining discussion of this section will focus on the influence of the unsteady LES fields on the collection of solid particles. In order to circumvent the high cost of computing the trajectories of mono-disperse clouds of particles, we elect to perform the transient particle tracking calculations using a poly-disperse distribution. A similar analysis was presented for the two-dimensional study, and we shall rely on the same initial diameter-distribution shown in figure 2.20. The number of particles, however, was increased to approximately $600,000$ so as to inject a considerable stock from each size bin. Figure 4.33 shows the cloud of particles a few time steps after their release from the throat. It can be seen that the larger diameter particles ($d_p \sim 1.8\ \mu m$) are leading to the front of the issuing jet, while the medium size particles ($d_p \sim 1.0\ \mu m$) are primarily migrating to the peripheral layers of the jet. A subsequent snapshot is taken in figure 4.34, which shows the posture of the same injection as it undergoes virtual impinging. The influence of inertia is clearly depicted. Remarkably, we are able to discern the interaction mechanism between the particles of different size, and the jet shear layers. It appears that the "upper free boundary layer" (structure 'A' in Table 4.4) is a *sink* for the particles of size one micro-meter. The largest particles of course, are inclined to penetrate into the minor flow, and begin to adjust to the laminar profile. The particle transport be-

havior from the LES results seems to be consistent with the analysis concocted in section 2.4.4. An unprecedented stance, nonetheless, that was not inferred from the two-dimensional calculations, is learned from figure 4.34. This is particularly related to the **escapade** of some of the large particles ($d_p > 1.5\ \mu m$) into the major flow. As shown, a considerable portion of the largest particles are subject to accumulation in the "lower free boundary layer" (structure 'B' in Table 4.4), which may very well explain the loss or reduced efficiency witnessed in figure 4.30, compared to the 2-D predictions. Additional support for this argument can be leveraged from figure 4.32 which shows the expansion profile of the secondary jet from the time-averaged LES of case II, and III. It can be seen that the Lilly simulation predicts a "contracted" profile relative to the Lagrangian model. The implications of the stronger major flow jet on particle transport, manifest as reduction in the separation efficiency as witnessed in figure 4.30.

Finally, we attempt to theoretically quantify the concentration per unit volume achieved by the prototype virtual impactor. A new cloud is generated with multiple groups each with an equal number of particles ($N_i = 138,000$) but different particle diameter, as shown in figure 4.35. The number concentration ($\equiv N_i / \sum N_i$) is then equal by design. At the end of the tracking calculation, the concentration in the minor flow is interrogated and plotted along with the initial concentration. As can be seen, the benefit is only attained for particles whose diameter is greater than 2.0 microns. The relative concentration level continues to gradually increase for larger particles, and the maximum that is gained for the 3.2 μm particles is about 7% with respect to the concentration in the throat prior to flow assorting. This finding is important for field studies that intend to intensify the ambient concentration of dilute aerosols.

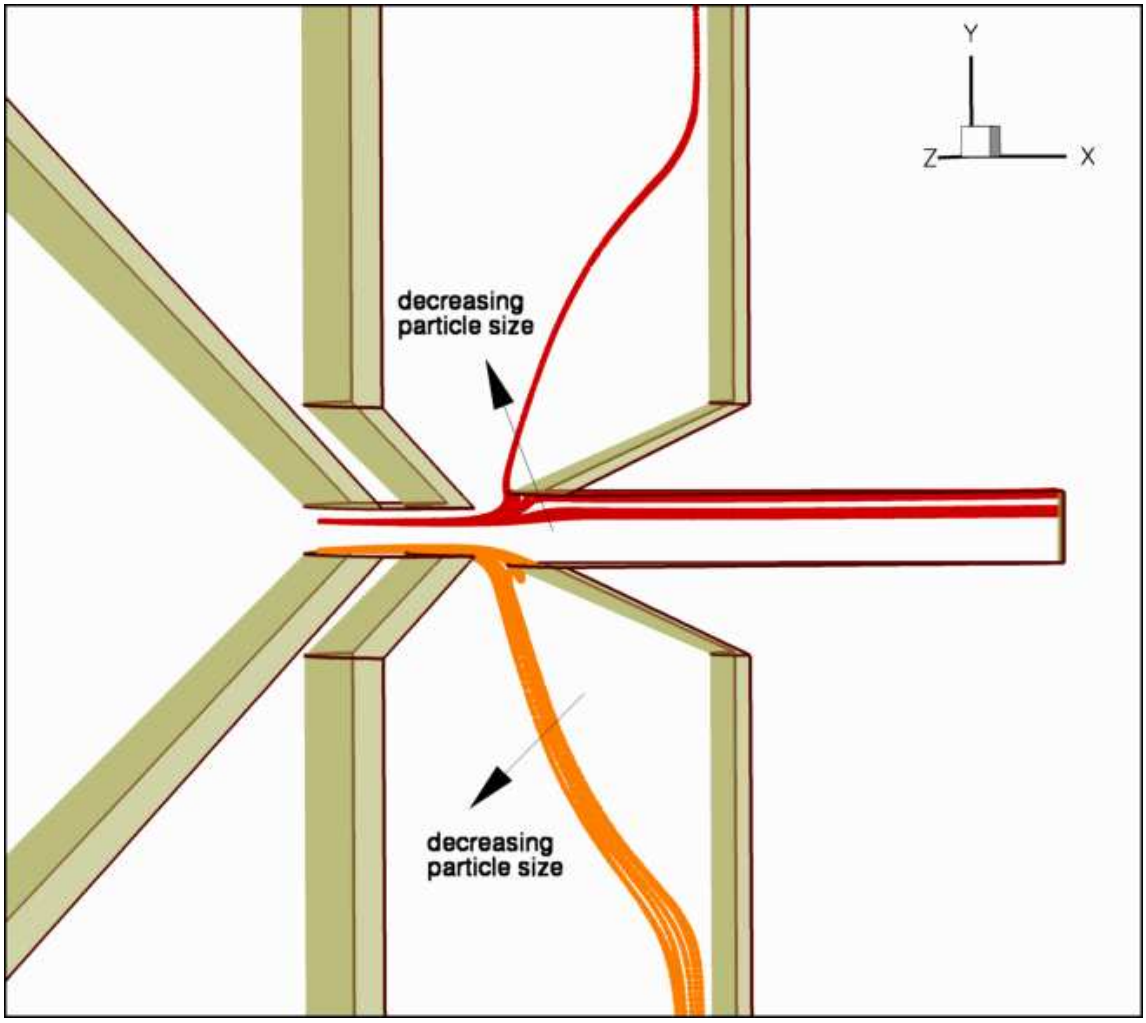

Figure 4.29: Solid particle traces from two starting locations tracked using the Lagrangian model LES mean field:case III. Particle diameters from Table 2.4: $0.72 - 3.20\ \mu m$

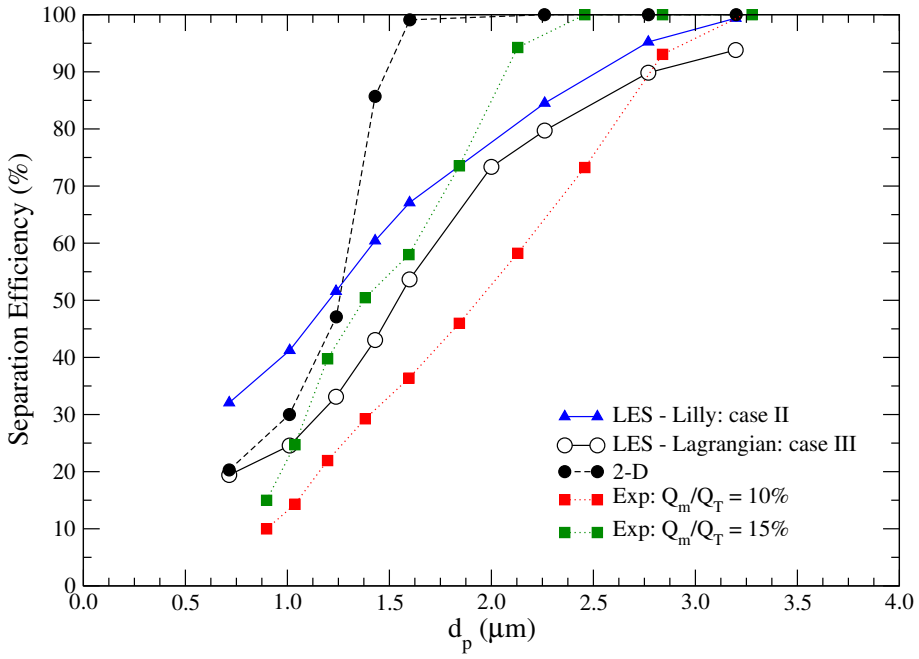

Figure 4.30: Separation efficiency from LES and experiment

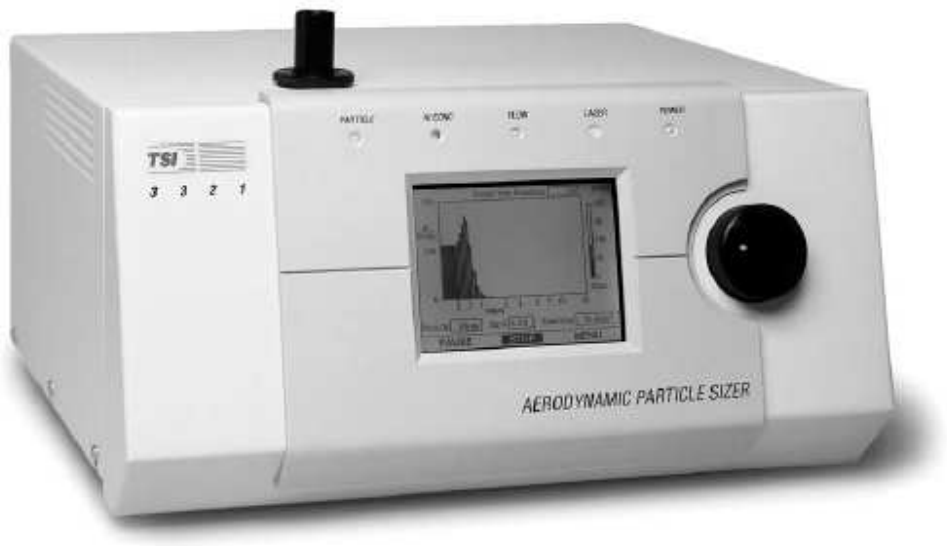

Figure 4.31: Model 3321 Aerodynamic Particle Sizer (picture borrowed from [82])

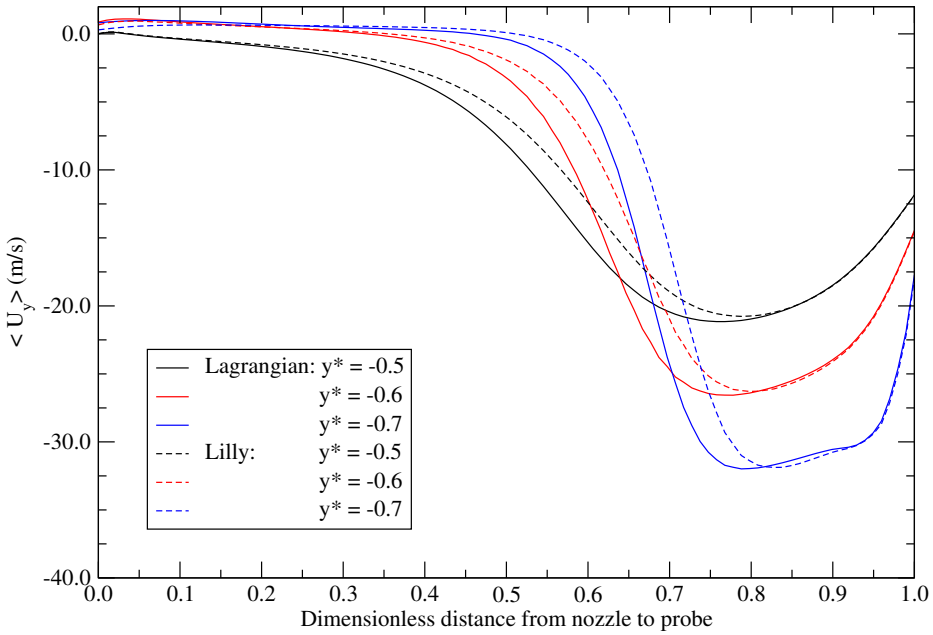

Figure 4.32: LES statistical mean expansion velocity profile at nozzle boundary layer: case II vs. case III

4.4.3 Segregation and Preferential Concentration

In section 2.4.4 we analyzed the fluid and particle interaction mechanisms present in the unsteady 2-D vortical structures. It was found that depending on the entry point to the jet (i.e. boundary layer, bulk centerline, etc.), and the magnitude of the particle dimensionless relaxation time (or Stokes number), the collective behavior of the particle cloud is affected. With regard to the particle propagation to the minor flow, we have shown that there exists a patterning sequence of jet events that cause the particles to selectively accumulate in the collection duct (i.e. braiding, or dancing). In this section, the focus will be primarily on the particle and fluid mixing in the **major flow**. This is particularly important for studying preferential concentration, segregation, and "streaking", and can help in improving the designs of multi-stage systems. In the context of the current large eddy simulation, there is sufficient resolution to educe the three-dimensional coherent structures, and to learn

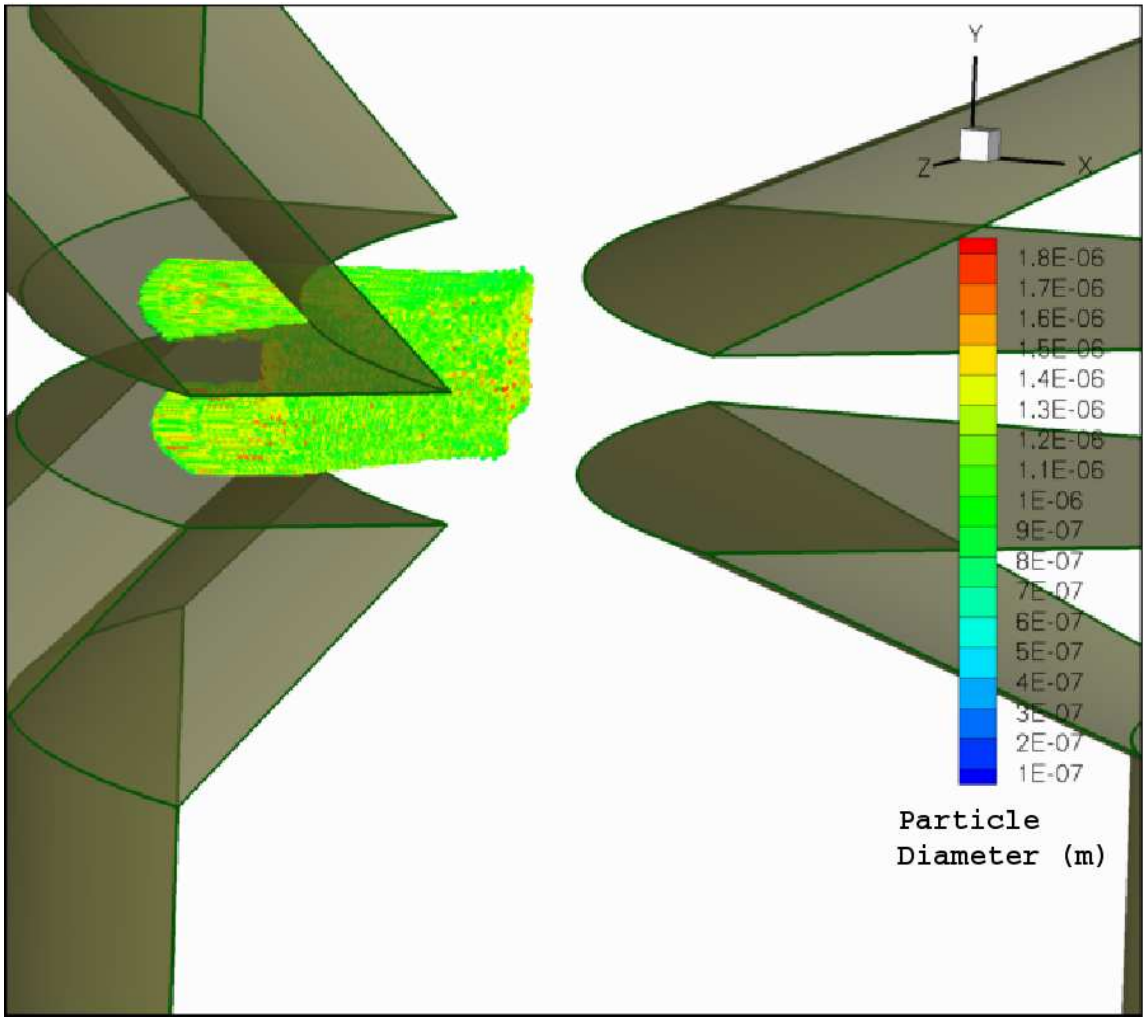

Figure 4.33: Injection of poly-dispersed particles colored by diameter and tracked using instantaneous LES fields-case III

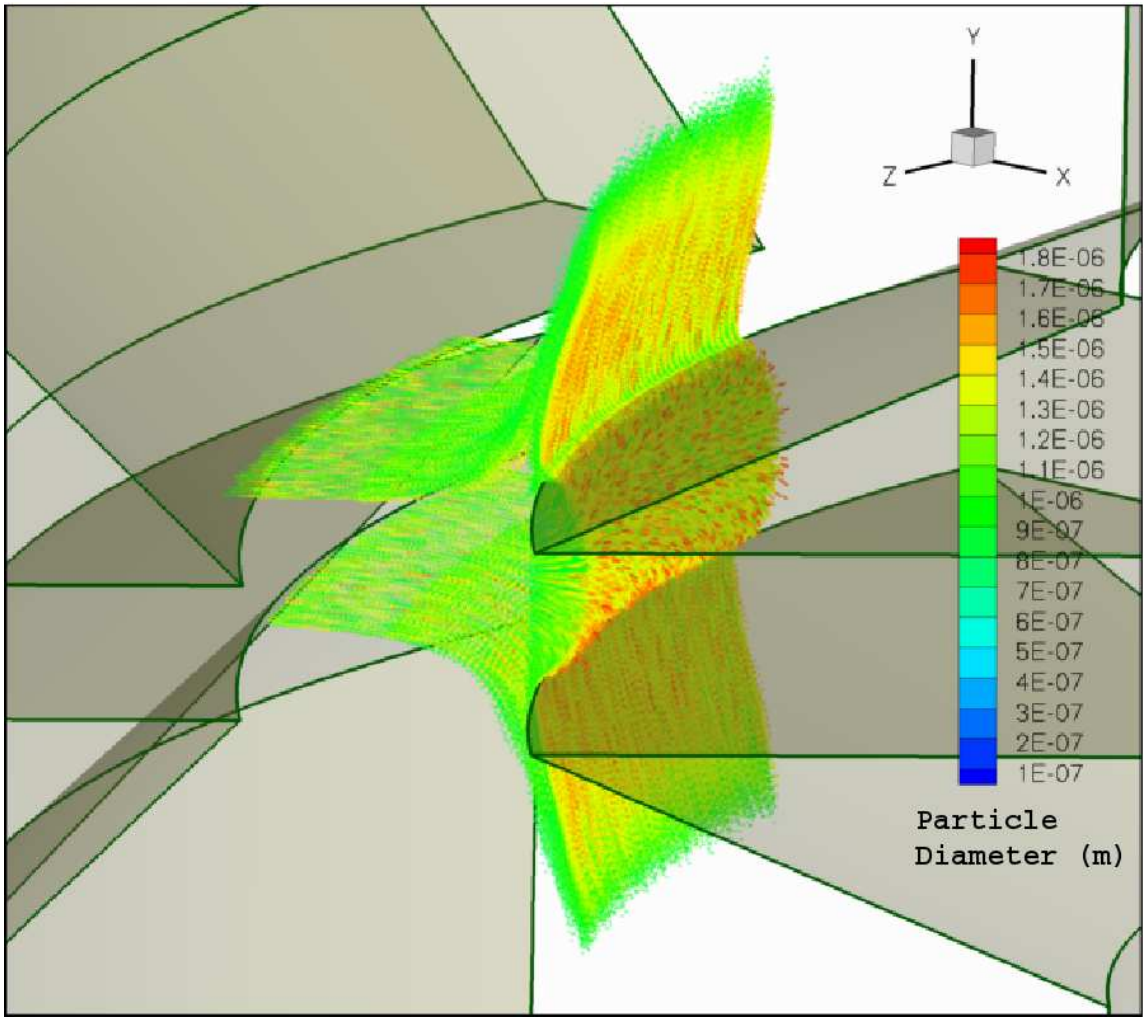

Figure 4.34: Separation of poly-dispersed particles colored by diameter and tracked using instantaneous LES fields-case III. Note transparent walls

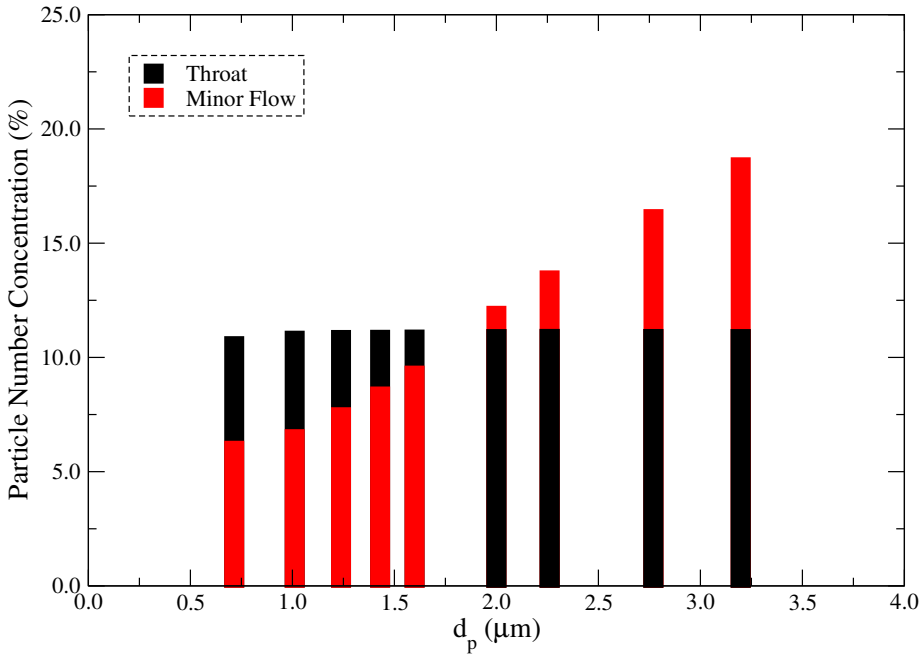

Figure 4.35: Particle number concentration before and after virtual impaction using the Lagrangian model LES:case III

about the influence of such structures on the dispersion of solid particles. It should be noted, however, that the highly resolved two-dimensional simulations of Chapter 2, indicated more vigorous activity near the main virtual impaction jet, than what the LES fields are showing. Nonetheless, the following calculations are conducted using the instantaneous LES velocity fields of the Lagrangian dynamic model (case III), with $575,000$ particles possessing a diameter $d_p = 1.01\ \mu m$. The corresponding Stokes number as listed in Table 2.6 is $St = 0.10$. The purpose for selecting this particular value serves to allow the particles to be responsive to changes in the local fluid velocity field, and from a practical standpoint, sheds insight on the behavior of some biological aerosols of interest in that range. As shown in figure 4.36, the particles are released in the throat boundary layer ($0 < y^* < 0.2$), and after turning with the secondary jet, they begin to experience the *rippling* effects of the coherent structures, as emphasized in figure 4.37.

The most interesting dynamics begin to occur at the shedding phase of the secondary jet, and near the wall section of the major flow chamber. Recall from Table 4.4, the prominence of type 'D' and 'E' structures. It is believed that the interaction of the particles with the flow is dictated by the nature of the evolution of these two types of coherent eddies, and their surrogates. Figure 4.38 shows a series of consecutive instantaneous depictions of the segregation and disruption of the originally uniform particle cloud. In the next set of images, we show the same particle locations superimposed on the fluid structures as educed by the Q-criterion of equation (4.3). Figure 4.39 shows two views from the first picture of the series in figure 4.38. As can be seen, the turbulent activity is restricted to the near wall region, where the coherent eddies are abundant. The subsequent images in figures 4.40 and 4.41 attempt to clarify the organized events that lead to the observed posture of the particles. Evidently, we can recognize that the coherent eddies play several roles. First, the instantaneous stills suggest that the particles preferentially accumulate on the outer boundaries of the tube-like eddies, which seem to engage the particle cloud in a penetrating fashion to create gaps or *streaks*. Second, certain eddies, conceivably the ones with strong rotational strength, are capable of twisting the particle agglomeration causing radial distributions that appear as hollow bindings of particles. Lastly, we observe that the streaking tendency eventually transforms into wider disconnectivity, therefore leading to increased dispersion and scattering of the original particle cloud.

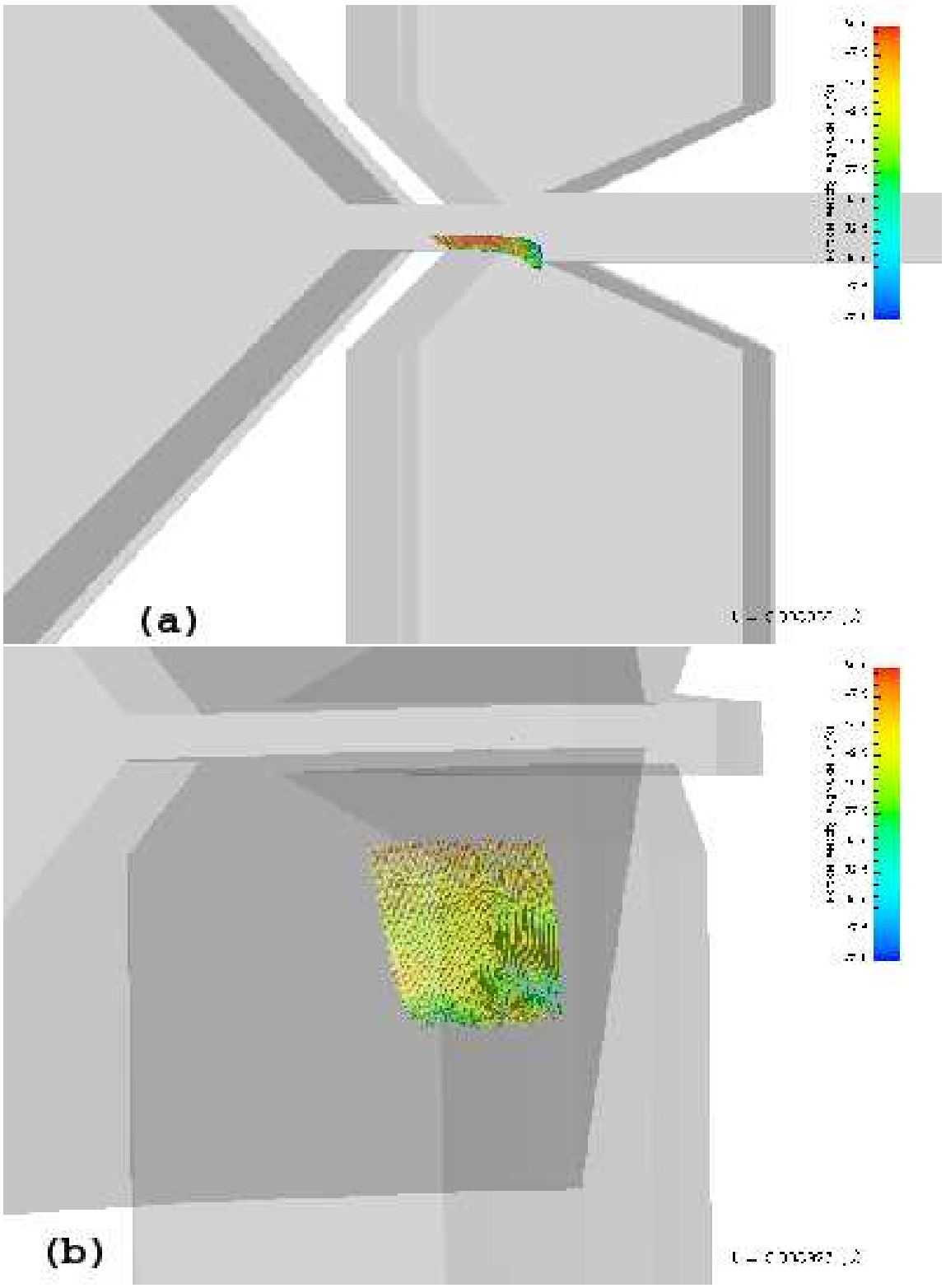

Figure 4.36: Snapshots of solid particles ($St = 0.10$) released from the throat boundary layer, and tracked by LES fields of case III. (a) side view of particles after release, (b) back view of particles entering major flow

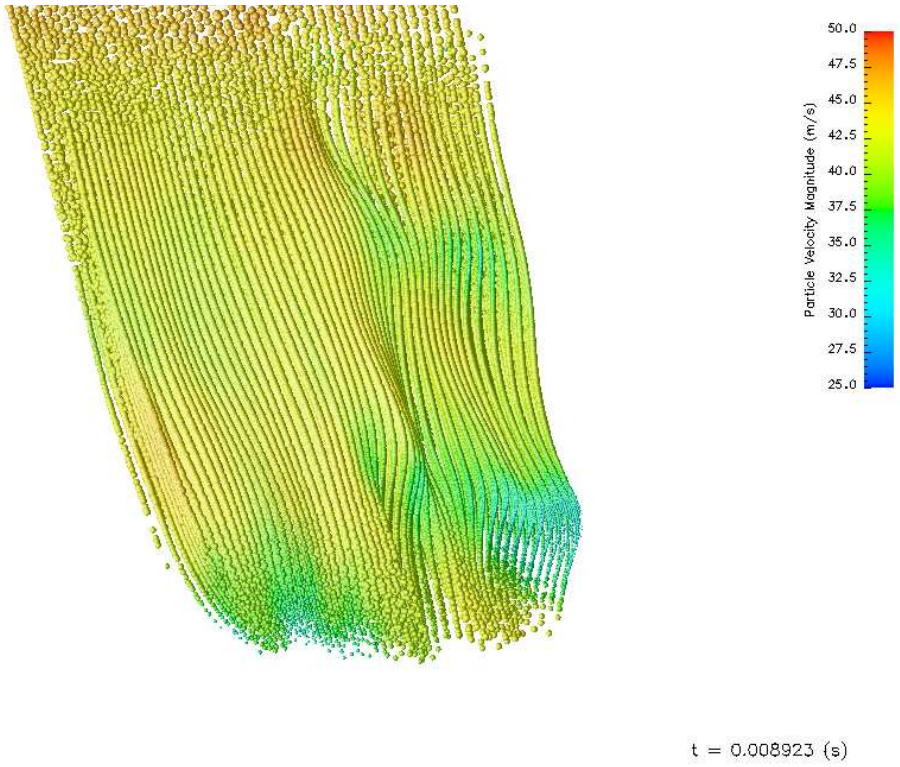

Figure 4.37: LES:case III - Enlarged view of figure 4.36-(b). Solid particles ($St = 0.10$) experiencing rippling in the major flow

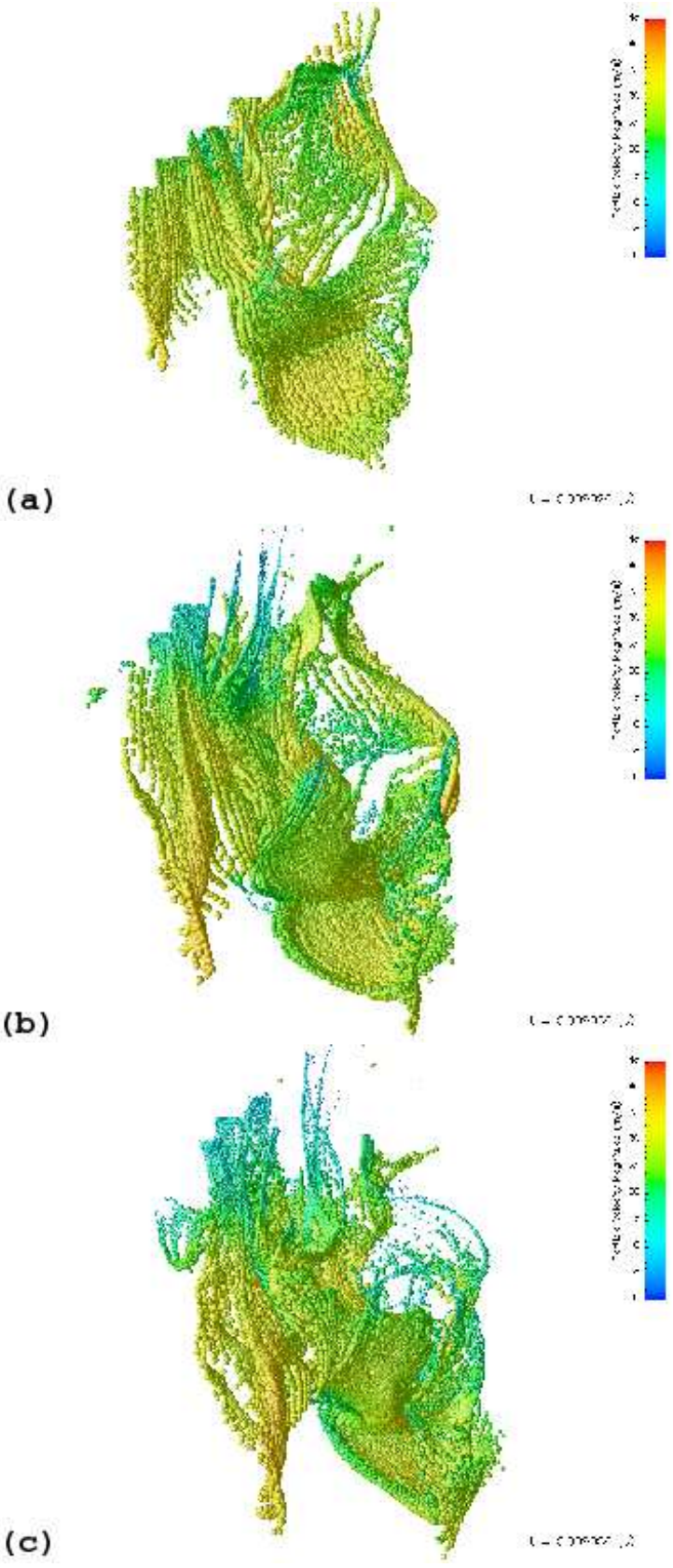

Figure 4.38: LES:case III - Enlarged view of solid particles ($St = 0.10$) dispersing in the major flow. Snapshots taken at: $t_1,\ t_2 = t_1 + \tau_{vi},\ \&\ t_3 = t_1 + 2\tau_{vi}$

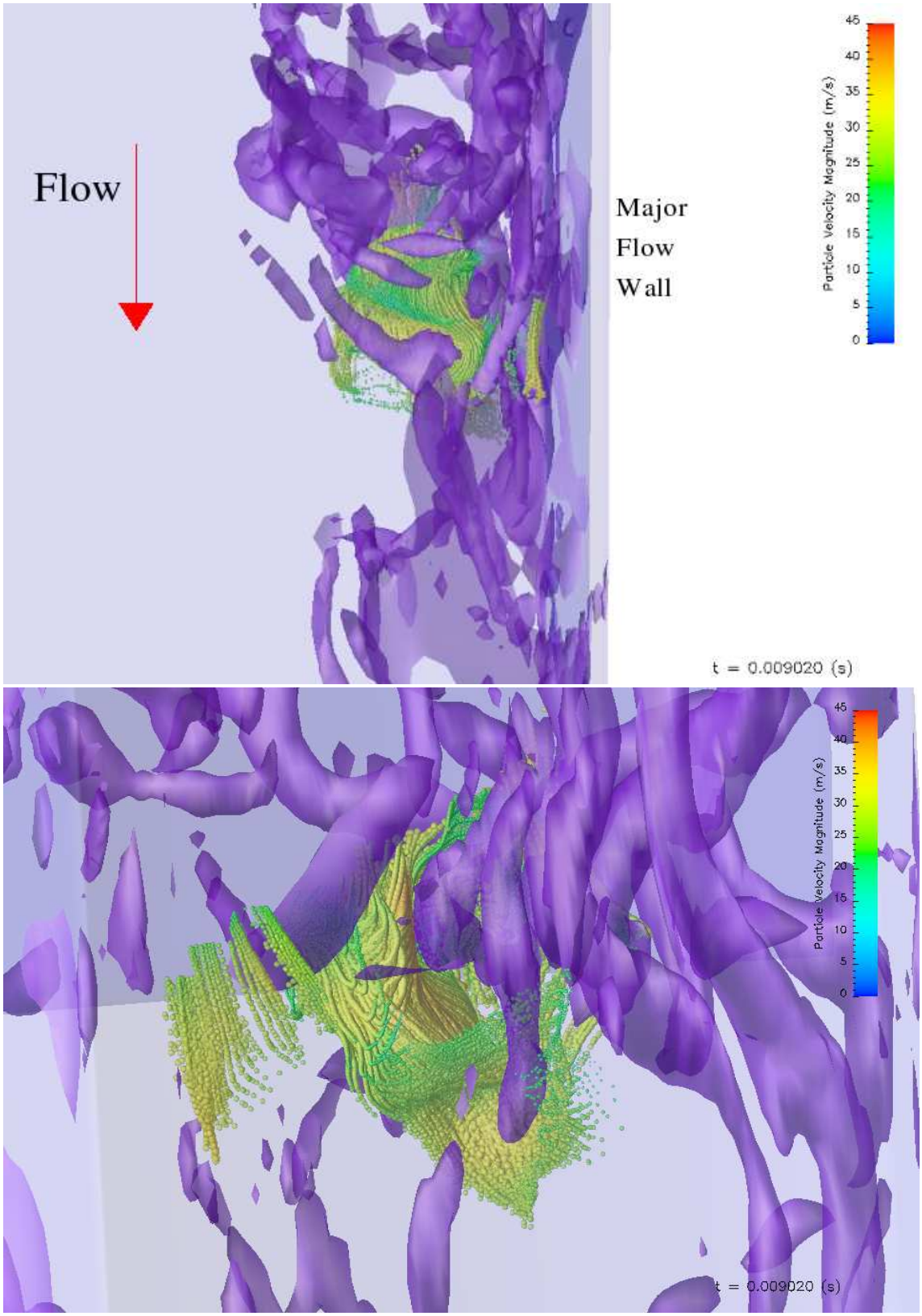

Figure 4.39: LES:case III - solid particles ($St = 0.10$) interacting with eddies of $Q = 0.15{\Omega_o}^2$. Different views taken at t_1 of figure 4.38-(a)

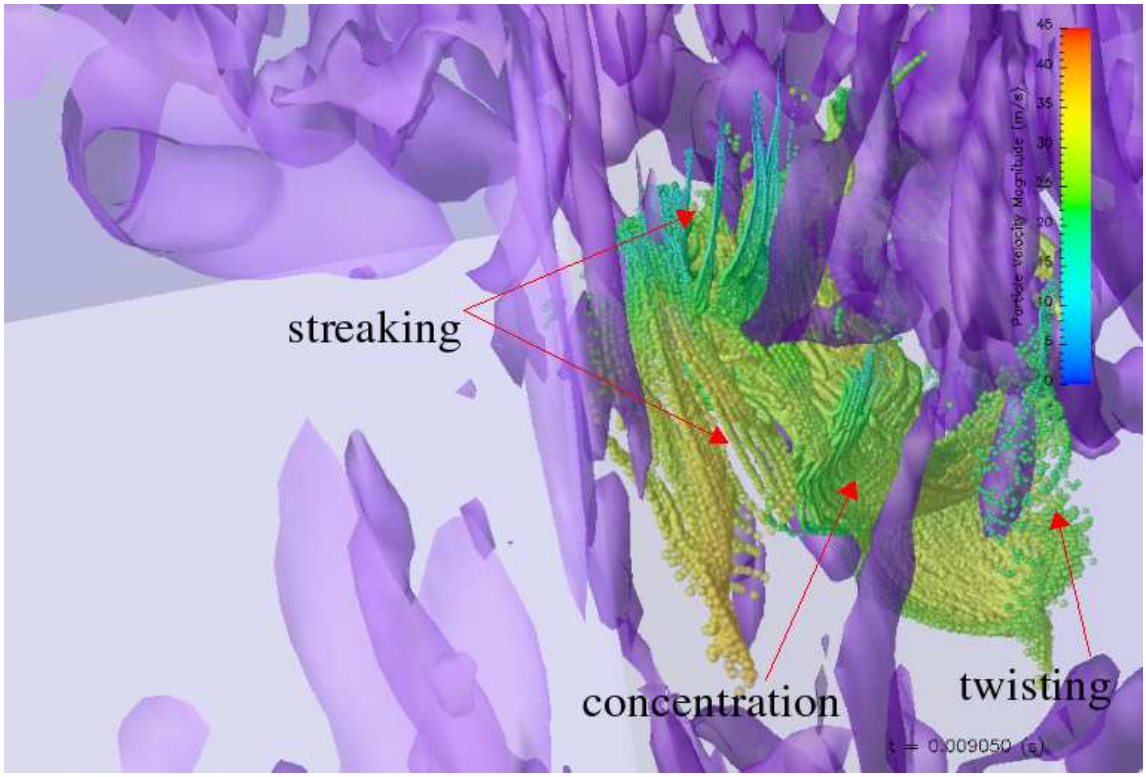

Figure 4.40: LES:case III - solid particles ($St = 0.10$) interacting with eddies of $Q = 0.1{\Omega_o}^2$. Snapshot taken at t_2 of figure 4.38-(b)

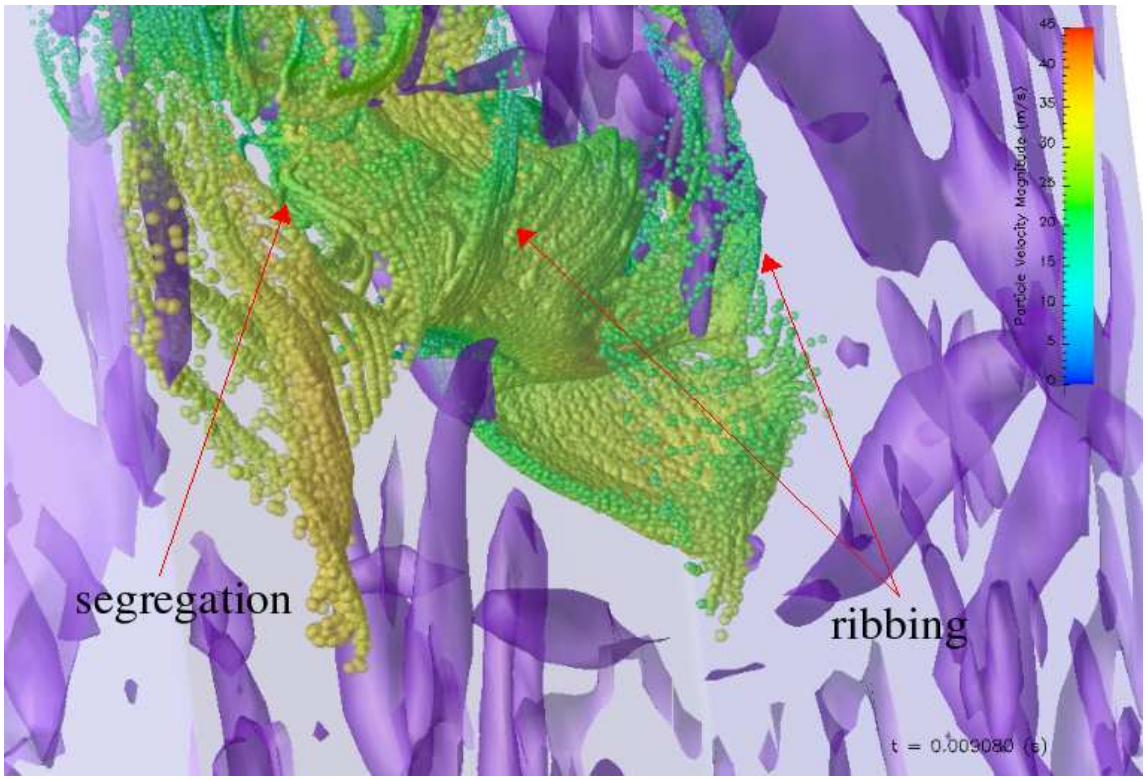

Figure 4.41: LES:case III - solid particles ($St = 0.10$) interacting with eddies of $Q = 0.1{\Omega_o}^2$. Snapshot taken at t_3 of figure 4.38-(c)

Chapter 5

Summary, Conclusions, & Recommendations

5.1 Summary of Two-dimensional Study

The flow of air inside the virtual impactor was modeled using a two dimensional cross-section of the cylindrical apparatus. The complete incompressible Navier-Stokes equations were integrated numerically on a fine mesh using second order methods. This approach is novel and fundamental to the study of virtual impaction jets since it permits the analysis and characterization of the transient small-scale eddies that are essential for particle transport. Antecedent theoretical studies of this type of flow only dealt with steady-state solutions. In this work, three sets of time-dependent flow fields were obtained by changing the inflow velocity of the sampler in order to arrive at different values for the jet Reynolds number. The results allowed for the comparison of stable and unstable flow regimes. The geometrical considerations for the nozzle design relied on experimental evidence from the literature concerning the superiority of protruded configurations. Certain aspect ratio adjustments were made based on numerical analysis, particularly for the virtual impaction gap width in order

to achieve proper flow separation. For all the reported studies, the width of the jet remained $W = 0.7mm$, $S = 2.1W$, and $W_c = 1.5W$.

The fluid equations of motion were advanced from a stationary field using the finite-volume code of FLUENT complemented by a user defined function for the outflow convective boundary conditions. Sufficiently small time steps were used in each case in order to capture the relatively rapid evolution of the organized fluid structures (see Table 2.1 for exact values). The aerosol motion was modeled by solving the particle equation of motion for a sphere including the drag and gravitational acceleration. A custom code that invokes the second order Adams-Bashforth integration scheme was employed in conjunction with dynamic drag coefficients. The results were divided and interpreted within two categories: (i) a time-averaged flow, and (ii) an unsteady flow. The main findings and conclusions are outlined in the following section.

5.1.1 Conclusions

- The 2-D time-mean results of the virtual impactor established the nature of the jet potential core. It was found through successive profiling of the mean velocity that a non-laminar jet exhibits a shorter piercing region where the centerline velocity decays faster than that of a laminar jet.

- A phenomenon termed "shear layer leakage" was discovered under unsteady jet conditions, by which the adverse pressure gradient acts to reduce the centerline velocity, hence causing a local acceleration for the off-axis fluid, coupled with an increase in jet-breadth.

- The re-laminarization behavior prior to minor flow mitigation was clearly demonstrated for the high Reynolds number jets.

- One-way coupled Lagrangian particle tracking with mono-dispersed samples of $100,000$ solid non-interacting spheres was used to query the separation efficiency

and particle loss properties of the virtual impaction and collection nozzles' design.

- The separation efficiency curve versus Reynolds number showed significant reduction in the 50% cut-point diameter. Specifically, the cutpoint particle diameter was 2.80, 1.25, & $0.97\mu m$ for case I, II, and III, respectively. The corresponding $\sqrt{St_{50}}$ was equivalent to 0.39.

- The steepness and asymptotic attributes of the separation efficiency curves from the two-dimensional analysis reflected that of the literature experimental results gathered from a similar virtual impactor with a larger nozzle width.

- The study pioneered in tracking the variations of poly-dispersed aerosol size distributions. This type of analysis revealed a unique picture concerning the behavior of particle distributions **during** virtual impaction. It was found that a high degree of disruption is instigated for particles close to the cutpoint diameter. The effect of backflow from the collection probe was clearly targeted by the "before" and "after" properties of the size distribution.

- The study investigated the role of the jet Reynolds number in altering the final minor flow particle size distribution. It was shown that for the flow conditions understudy, there exists a critical size around 1.2 microns that distinguishes among response mechanisms by which the polydisperse distribution modulates to virtual impaction.

- Transient flow realizations identified the origins of the instability for non-laminar regimes. In the laminar case, the fluctuations were limited to smooth oscillations by the *attached* vorticity rich layers in the major flow chambers.

- At transition and turbulent conditions, it was observed that the free boundary layers begin to separate from the vorticity rich layers extending from the nozzle

throat as well as the leading edge of the probe. The shear layers between the high speed fluid and the relatively motionless fluid cause the materialization of the *mirrored Kelvin-Helmholtz* instability.

- At mild to high Reynolds numbers, it was discovered that the flow instability is **self-sustained** due to the generated disturbances and descendant eddies emerging from the impaction of disintegrated shear layers onto the chamber walls.

- Quantitative analysis based on correlations of the fluctuating velocity components asserted between two types of instabilities inherent to the virtual impaction jet. First, a jet-axis destabilization mode is believed to be natively an outcome of jet-column swinging. Second, a more potent shear-layer mode is stimulated by eddy interaction events, and vortex shedding.

- The theoretical study presented an insightful discussion on the classified Reynolds shear stress components, and pinpointed the location and strength of its most influential contributors within the bent mixing layer.

- Unsteady particle tracking for particles with three Stokes numbers between 0.1 and 1.0 were performed in order to study the particle-eddy interaction mechanism.

- Particles with dimensionless relaxation times less than 0.5 are capable of following the fluid curvatures if they enter the jet near the throat boundary layer, and are consequently flung outwards by the roller vortices. If the particles are traveling above the boundary layer, they will accumulate in a "braided" fashion in the minor flow due to the resonance of the jet core fluctuations. The dispersion level within the probe duct is highest for particles whose $St = 0.10$.

- Particles whose dimensionless relaxation times are greater than or equal to unity

are inclined to aggregate in the minor flow experiencing minimal interaction with the jet dynamics. Those particles ejecting from the throat boundary layer are primarily deposited on the probe walls.

5.2 Summary of LES Studies

The merits of Large Eddy Simulation in engineering fields that require flow prediction and judgment are countless. Ever since its inception as a viable means for understanding transitional and turbulent flows, there has been a tremendous effort to provide accurate and effective models for the closure of subgrid scale stresses. Needless to say, despite the existence of a number of approaches that can fulfill such requirements, very few models in fact are successful in complex geometries, and multi-regimen flows. For this reason, we embarked on implementing and proving the suitability of the Lagrangian dynamic subgrid scale (SGS) turbulence model. After presenting the mathematical framework for conducting large eddy simulation, and highlighting the conventional methodologies sought in modeling the residual stresses, we conceded that for the virtual impactor study an advanced and physically sound scheme is acutely needed, in order to guarantee the proper representation of the coherent structures discovered by the two-dimensional investigation. Hence, the Lagrangian dynamic model was deemed as a felicitous candidate. In summary, the strength of such a model lies in its ability to procure an eddy-viscosity coefficient that is in tune with the dynamics of the flow, particularly the *history* of the flow leading up to the current state.

The first LES study focused on validating the model implementation and its numerical algorithm for a fully developed turbulent channel flow. Undoubtedly, this allowed us to gain confidence in the capabilities of the newly developed code, as well as gauge the performance and accuracy of the numerical schemes in this fundamental flow framework. The results were obtained for a Reynolds number equal to 3300 based

on mean centerline velocity and channel half-width. The prediction of first and second order statistics compared exceptionally well to direct numerical simulation data. The second validation case was carried out for a turbulent flow past a square cylinder. The bluff body was engulfed in a computational domain with spanwise periodic boundary conditions, and lateral symmetry conditions. The Reynolds number based on free stream velocity and edge length was equal to $21,400$. The exhibition of organized vortex shedding was well captured by the simulation. Global quantities such as the Strouhal number, lift, and drag coefficients concerted favorably with the referenced experimental data and other computations. The Lagrangian dynamic model excelled in the prediction of the time-averaged velocity profile in the wake of the cylinder compared to the standard, and even dynamic Smagorinski model. Furthermore, turbulent intensities in the near wake were positively represented. In the far wake, reasonable agreement of second order statistics was obtained. Several influential factors that can cause disparity between the numerical and experimental results were addressed.

The newly contrived code was then applied to the study of a prototype aerosol sampling device. Solution strategies that can deal with the challenges associated with simulating a real-life geometry while maintaining numerical accuracy were crafted. First, to balance between grid requirements and available computer memory, a 45 degree pie-section was meshed with hexahedral elements which are superior to tetrahedral elements in terms of alleviating the numerical discretization errors. The base grid consisted of approximately 4 million cells, and a refined analogue consisted of $\sim$ 6 million control volumes. Rotational periodic boundary conditions were put in place to mimic the cylindrical periodicity of the flow. In addition to the Lagrangian dynamic sub-grid scale model, we evaluated the operation and results obtained by the algebraic Lilly model. The inflow and outflow conditions shadowed one of the cases studied by direct solution. The total sampling capability of the device amounted to 600 $liters/min$, at a Reynolds number of ≈ 4700. The LES equations were advanced

by a second-order implicit time marching scheme, using the same time step as the direct simulation. The algorithmic details are summarized in Table 2.2. The results focused on assessing the performance and adequacy of each turbulence closure model, and aimed to explain the characteristics of the prominent resolved eddy structures vis-a-vis particle transport mechanics. The main findings and conclusions are outlined in the following section.

5.2.1 Conclusions

- This research demonstrated the feasibility to conduct very accurate large eddy simulation of a fully developed channel flow at $Re_\tau = 180$, with the Lagrangian dynamic turbulence closure model, using FLUENT's widely available commercial code.

- This research improved on the results of a large eddy simulation of a high Reynolds number flow past a square cylinder. The Lagrangian dynamic subgrid scale model testified to its resourcefulness in dealing with complex & unsteady flow behavior.

- Equipped with a robust residual stress model, this research pioneered in its pursuit of investigating the dynamics of coherent structures present in three dimensional virtual impactors.

- The computational expense ensued by the large eddy simulation of the circumferential slit virtual impactor with the Lagrangian dynamic SGS model proved to be within a surplus of 4% relative to the cost of the Lilly model LES, on the same grid.

- The LES first order statistics of jet velocity proved to be identical on the two grid resolutions. Some deviations were detected in the spanwise root mean

square velocity component whereby the fluctuation level differed in the mixing layers of the jet.

- The estimated turbulent kinetic energy of the sub-grid scales did not exceed 2% of the mean kinetic energy of the feeding jet.

- The LES results in the middle plane of the domain suggest a three-dimensional growth mechanism for the jet mixing layers, since the mean velocity profiles consistently exceeded the profiles predicted by the two-dimensional calculation.

- Comparisons among the virtual impaction velocity profiles of the Lagrangian dynamic and Lilly models showed that despite the agreement at the nozzle exit plane, the former model predictions are relatively receded near the probe entrance.

- Comparisons among the dynamic Smagorinski coefficient between the Lagrangian and Lilly model showed that the former predicts higher magnitudes in the areas of flow deflection/ejection, and transition to turbulence.

- The turbulent kinetic energy predictions of the secondary jets were slightly more restrained in the Lagrangian LES, relative to the dynamic Lilly simulation.

- The Lagrangian dynamic model LES exhibited significant regions of high sub-grid turbulent viscosity, compared to the dynamic Lilly simulation.

- The large eddy simulation results allowed us to identify the origin of **five** key coherent structures that dominate the physics of the major flow evolution. The vortical structures are: (i) *extended-throat free boundary layer*, (ii) *leading-edge free boundary layer*, (iii) *circulatory wall-born vortices*, (iv) *wake vortices*, and (v) *rebound vortices*.

- Three dimensional vortex rings and longitudinal vorticity filaments were educed using the Q-criterion.

- The time-mean velocity field of the Lagrangian dynamic model large eddy simulation provided the best ground to conduct particle tracking calculations. Comparison with preliminary experimental data for the aerosol separation efficiency showed fairly good agreement.

5.3 Recommendations

The work presented in this thesis elucidated some of the interesting mechanics of virtual impaction. As with any modeling enterprise there is always the question of precision, which warrants careful examination of the undertaken assumptions and methodologies. Future endeavors that aim to explore and advance the research concepts engaged in this study must focus on the following:

- The two-dimensional direct solutions of the Navier-Stokes equations provided a wealth of information concerning the evolution, interaction, and sustainability of the coherent eddies. For this reason, it is believed that a three-dimensional direct numerical simulation, which must be done on a supercomputer, will help in understanding the true intricate features of the transient coherent structures.

- The study did not pinpoint exactly the onset of transition to turbulence. In fact, a number of calculations with gradual variations in the Reynolds number are needed in order to learn the value of Re at which the free boundary layers become unstable.

- A detailed look at the physics of aerosol particles' interaction must be done in order to ascertain the level of uncertainty endured by neglecting inter-particle collisions. In fact, a numerical study with two-way coupling and models that

simulate breakup and coalescence can shed some insight on the effects of particle loading on the flow. The reader is referred to a fundamental article on this topic [83].

- In order to unambiguously judge the credibility of the large eddy simulation residual stress models, *a posteriori* tests against experimental data in a similar jet configuration must be checked. An assessment of LES results in an "edge tone" flow problem is highly endorsed.

- The LES study of the round slit virtual impactor did not address the influence that the approximate rotational periodic boundary condition has on the characteristics of the flow. Future computations must be done with larger sectors to insure the fidelity of the results.

- According to Pope [84], the scale similarity notion is intractable in transitional and viscous near-wall regions. Hence, since the current LES study can not escape such circumstances, it is perhaps beneficial to quantify the dependence of the dynamic coefficient on the filter Δ.

- With regard to building virtual impactors with cascaded jets, it is constructive to manipulate the shape of the expansion bays so as to limit the propagation of feedback effects.

Appendix A

User Defined Function (UDF) for the Convective Boundary Condition

An outflow boundary condition in the traditional sense is in most cases chosen to be far away from the region of interest in the flow. Indeed, the outflow boundary condition is an artificial way of mimicking or imposing a certain behavior on the flow, that is generally hard to predict. The simplest technique, of course, is to assign a fixed value for the primitive variables being solved, which is known as "Dirichlet". A more suitable alternative, after "Neumann", assumes that the primitive variable, for example velocity, has a zero-diffusion flux in the direction normal to the outflow interface. The latter approach physically reflects a fully-developed state. For certain flows, however, it is perceivable that a fully developed state will not be achieved at a reasonable distance from the "high activity" region of the flow. For unsteady flow phenomena, therefore, more felicitous boundary conditions have been devised. Orlanski [52] first proposed a *non-reflecting* condition for one dimensional wave propagation in hyperbolic equations. The technique has since been successfully used in solutions of the

Navier-Stokes equations in several computational fluid dynamics problems [85, 86]. The fluid velocity at the outflow plane is obtained by solving the following first-order partial differential equation:

$$\frac{\partial U_i}{\partial t} + U_c \frac{\partial U_i}{\partial x} = 0 \tag{A.1}$$

where U_c is a characteristic *convective* velocity at the plane of exit. In the context of the FLUENT simulations, U_c is sampled from the plane-normal face velocities provided by the solver subsequent to the mass balance correction step performed at each time step.

A.1 Validation

The unsteady incompressible laminar wake behind a circular cylinder was chosen as a test case for the newly implemented outflow boundary condition. This problem possesses very interesting flow features especially the alternating wake vortices, and their unsteady propagation away from the surface of the cylinder. The results of a prior numerical investigation using cylindrical coordinates, and well documented in the literature [87] will be used to validate the results of the simulation presented herein. Two calculations were carried out in FLUENT using the same discretization and numerical schemes described in Chapter 2 for the two-dimensional virtual impactor study. The first calculation was performed on a domain with Neumann boundary conditions specified **20** diameters away from the center of the cylinder. The second run, was performed on a shorter domain, with the convective boundary condition applied only **14** diameters away from the cylinder's center. A uniform inflow velocity was assigned 5 diameters upstream of the cylinder. The corresponding Reynolds number based on the cylinder diameter (D) and free stream velocity (U_∞) is 100. The top and bottom domain boundaries were modeled as frictionless walls spanning 10 diameters apart. Figure A.1 shows a comparison of the instantaneous velocity at the same moment

in time from both computations. Qualitatively, it is evident that the characteristic features of the wake are well matched. Thus, the flow dynamics upstream of the outflow boundary condition are undistorted. Quantitatively, the y-component of velocity one diameter away from the cylinder's center is recorded and plotted in Figure A.2. Clearly, the periodic nature of the wake is manifested as a sinusoidal variation in the cross-stream velocity. The period of fluctuations is measured and quantified via the dimensionless Strouhal number defined as:

$$St_h = \frac{D}{T_s U_\infty} = 0.174 \tag{A.2}$$

which is in reasonable agreement with the 0.16 value reported in the original numerical study [87]. The experimental data, referenced therein, contend a range between 0.18-0.20. It should be noted that the present computation excels in the number of gridpoints used $\approx$ 118000, and in the length of the domain. Therefore, it is no surprise that the current St_h value is closer to the experiment.

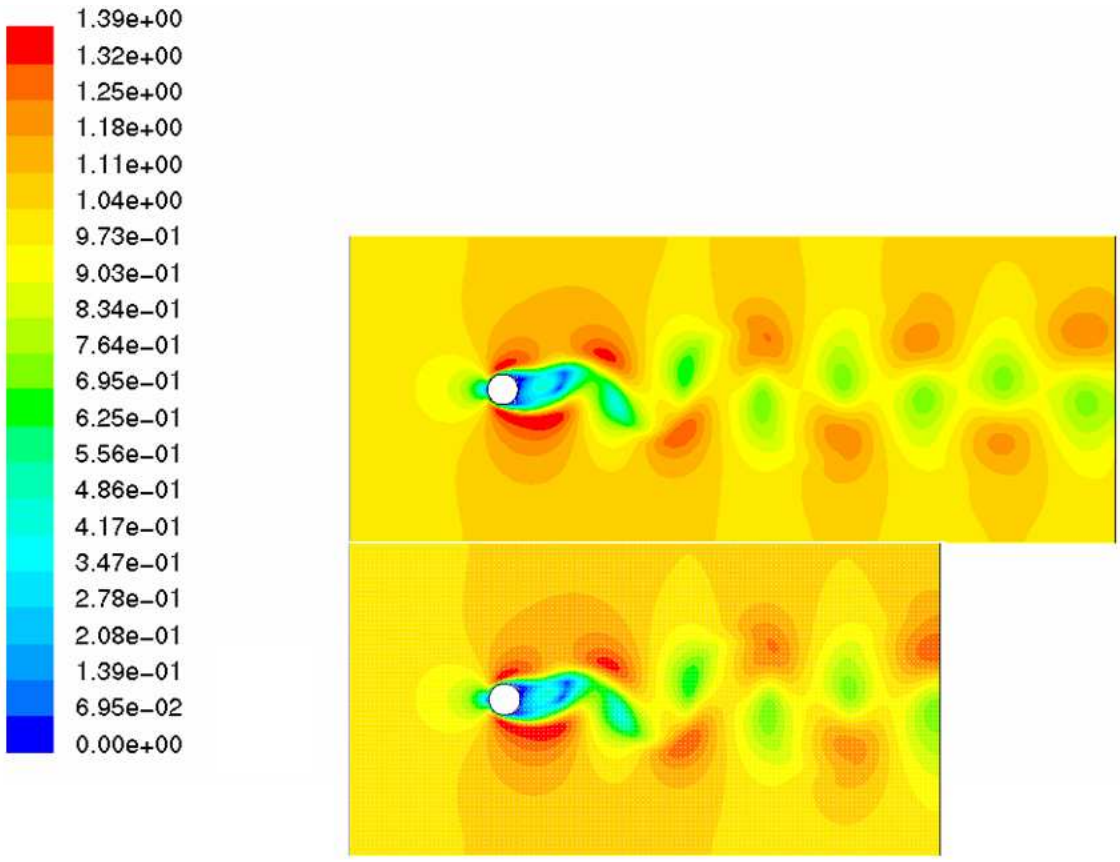

Figure A.1: Unsteady laminar wake - instantaneous velocity contours (m/s)

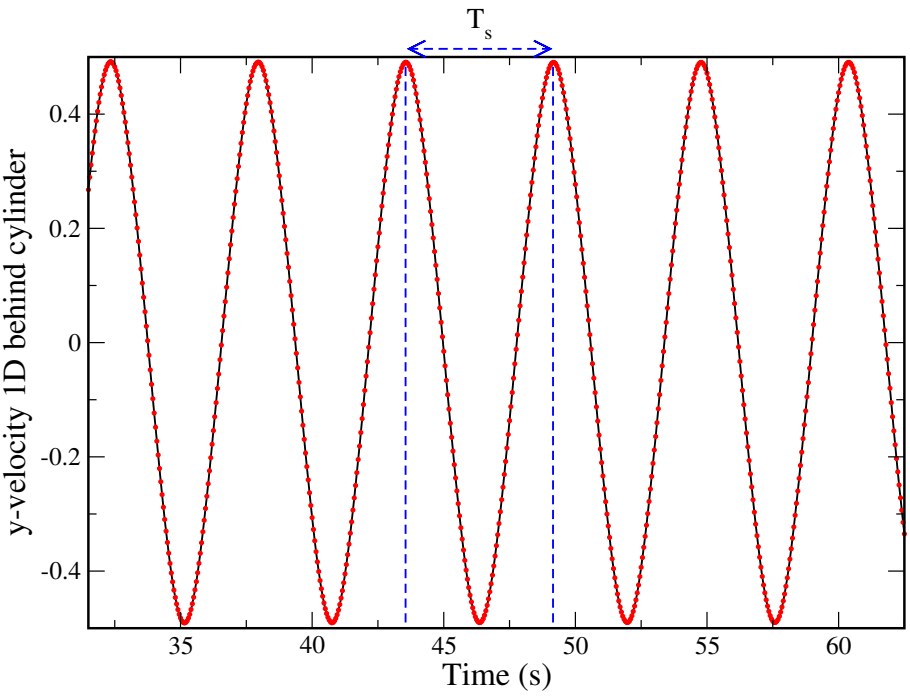

Figure A.2: Recorded y-velocity component in the wake of the cylinder

Bibliography

[1] McFarland, A. R., Ortiz, C. A., and Bertch, Jr. R. W. 1978 Particle Collection Characteristics of a Single-Stage Dichotomous Sampler, *Environmental Science and Technology* **12**, 679-682.

[2] Haglund, J. S., and McFarland, A. R. 2004 A Circumferential Slot Virtual Impactor, *Aerosol Science and Technology* **38**, 664-674.

[3] Haglund, J. S., Chandra, S., and McFarland, A. R. 2002 Evaluation of a High Volume Aerosol Concentrator, *Aerosol Science and Technology* **36**, 690-696.

[4] Goo, J. 2002 Numerical Simulation of Aerosol Concentration at Atmospheric Pressure by a Cascade of Aerodynamic Slit Lenses, *Journal of Aerosol Science* **33**, 1493-1507.

[5] Marple, V. A., and Chien, C. M. 1980 Virtual Impactors, A Theoretical Study, *Environmental Science and Technology* **14**, 976-984.

[6] Chen, B. T., Yeh, H. C., and Cheng, Y. S. 1985 A Novel Virtual Impactor: Calibration and Use, *Journal of Aerosol Science* **16**, 343-354.

[7] Ding, Y., and Koutrakis, P. 2000 Development of a Dichotomous Slit Nozzle Virtual Impactor, *Journal of Aerosol Science* **31**, 1421-1431.

[8] Rader, D. J., and Marple, V. A. 1985 Effect of Ultra-Stokesian Drag and Particle Interception on Impaction Characteristics, *Aerosol Science and Technology* **4**, 141-156.

[9] Asgharian, B., and Godo, M. N. 1997 Transport and Deposition of Spherical Particles and Fibers in an Improved Virtual Impactor, *Aerosol Science and Technology* **27**, 499-506.

[10] Forney, L. J., Ravenhall, D. G., and Lee, S. S. 1982 Experimental and Theoretical Study of a Two-Dimensional Virtual Impactor, *Environmental Science and Technology* **16**, 492-497.

[11] Kim, D. S., Kim, M. C., and Lee, K. W. 2000 Design and Performance Evaluation of Multi-Nozzle Virtual Impactors for Concentrating Particles, *Particle & Particle Systems Characterization* **17**, 244-250.

[12] Hari, S. 2003 Computational Fluid Dynamics Simulations of Dilute Fluid-Particle Flows in Aerosol Concentrators, *PhD Dissertation, Department of Nuclear Engineering, Texas A&M University.*

[13] Charrouf, M. L. 2004 Fluid and Particle Dynamics in an Aerosol Virtual Impactor, *Master's Thesis, Department of Chemical Engineering, University of Maryland.*

[14] Han, R., and Moss, O. R. 1997 Flow Visualization Inside a Water Model Virtual Impactor, *Journal of Aerosol Science* **28**, 1005-1014.

[15] Gotoh, K., Masuda, H. 2000 Improvement of The Classification Performance of a Rectangular Jet Virtual Impactor, *Aerosol Science and Technology* **32**, 221-232.

[16] Sato, H., and Sakao, F. 1964 An Experimental Investigation of The Instability of a Two-dimensional Jet at Low Reynolds Numbers, *Journal of Fluid Mechanics* **20**, 337-352.

[17] Michalke, A., and Freymuth, P. 1966 The Instability and The Formation of Vortices in a Free Boundary Layer, *AGARD. Conf. Proc.* **no. 4**, paper 2, 575-595.

[18] Sato, H. 1960 The Stability and Transition of a Two-dimensional Jet, *Journal of Fluid Mechanics* **7**, 53-80.

[19] Browand, F. K. 1966 An Experimental Investigation of The Instability of an Incompressible Separated Shear Layer, *Journal of Fluid Mechanics* **26**, 281-307.

[20] Crow, S. C., and Champagne, F. H. 1971 Orderly Structure in Jet Turbulence, *Journal of Fluid Mechanics* **48**, 547-591.

[21] Petersen, R. A., and Samet, M. M. 1988 On The Preferred Mode of Jet Instability, *Journal of Fluid Mechanics* **194**, 153-173.

[22] Browand, F. K., and Laufer, J. 1975 The Role of Large Scale Structures in The Initial Development of Circular Jets, *Turbulence in Liquids: Proceedings of the 4th Biennial Symposium on Turbulence in Liquids*, 333-344.

[23] Davies, P. O. A. L., and Yule, A. J. 1975 Coherent Structures in Turbulence, *Journal of Fluid Mechanics* **69**, 513-537.

[24] Rockwell, D., and Naudascher, E. 1979 Self-Sustained Oscillations of Impinging Free Shear Layers, *Annual Review of Fluid Mechanics* **11**, 67-94.

[25] Ho, C. M., and Nosseir, N. S. 1981 Dynamics of an Impinging Jet. Part 1. The Feedback Phenomenon, *Journal of Fluid Mechanics* **105**, 119-142.

[26] Chiriac, V. A., and Ortega, A. 2002 A Numerical Study of The Unsteady Flow and Heat Transfer in a Transitional Confined Slot Jet Impinging on an Isothermal Surface, *International Journal of Heat and Mass Transfer* **45**, 1237-1248.

[27] Akiyama, T., Yamamoto, K., Squires, K. D., and Hishida, K. 2005 Simulation and Measurement of Flow and Heat Transfer in Two Planar Impinging Jets, *International Journal of Heat and Fluid Flow* **26**, 244-255.

[28] Fric, T. F., and Roshko, A. 1994 Vortical Structure in The Wake of a Transverse Jet, *Journal of Fluid Mechanics* **279**, 1-47.

[29] Smith, S. H., and Mungal, M. G. 1998 Mixing, Structure and Scaling of The Jet in Crossflow, *Journal of Fluid Mechanics* **357**, 83-122.

[30] Rivero, A., Ferre, J. A., and Giralt, F. 2001 Organized Motions in a Jet in Crossflow, *Journal of Fluid Mechanics* **444**, 117-149.

[31] Camussi, R., Guj, G., and Stella, A. 2002 Experimental Study of a Jet in Crossflow at Very Low Reynolds Number, *Journal of Fluid Mechanics* **454**, 113-144.

[32] Megerian, S., and Karagozian, A. 2005 Evolution of Shear Layer Instabilities in The Transverse Jet, *43rd AIAA Aerospace Sciences Meeting and Exhibit*, **2005-142**.

[33] Burton, T. M., and Eaton, J. K. 2005 Fully Resolved Simulations of Particle-Turbulence Interaction, *Journal of Fluid Mechanics* **545**, 67-111.

[34] Maxey, M. R., and Riley, J. J. 1983 Equation of Motion for a Small Rigid Sphere in a Nonuniform Flow, *Physics of Fluids* **26**, 883-889.

[35] Elghobashi, S. 1994 On Predicting Particle-Laden Turbulent Flows, *Applied Scientific Research* **52**, 309-329.

[36] McLaughlin, J. B. 1994 Numerical Computation of Particles-Turbulence Interaction, *Intl. J. Multiphase Flow* **20**, Suppl., 211-232.

[37] Stock, D. E. 1996 Particle Dispersion in Flowing Gases, *Journal of Fluids Engineering* **118**, 4-17.

[38] Crowe, C. T., Troutt, T. R., and Chung, J. N. 1996 Numerical Models for Two-Phase Turbulent Flows, *Annual Review of Fluid Mechanics* **28**, 11-43.

[39] MacInnes, J. M., and Bracco, F. V. 1992 Stochastic Particle Dispersion Modeling and the Tracer-Particle Limit, *Physics of Fluids* **4**, 2809-2824.

[40] Wang, Q., and Squires, K. D. 1996 Large Eddy Simulation of Particle-Laden Turbulent Channel Flow, *Physics of Fluids* **8**, 1207-1223.

[41] Uijttewaal, W. S. J., and Oliemans, R. V. A. 1996 Particle Dispersion and Deposition in Direct Numerical and Large Eddy Simulations of Vertical Pipe Flows, *Physics of Fluids* **8**, 2590-2604.

[42] Armenio, V., Piomelli, U., and Fiorotto, V. 1999 Effect of The Subgrid Scales on Particle Motion, *Physics of Fluids* **11**, 3030-3042.

[43] Derksen, J. J. 2003 Numerical Simulation of Solids Suspension in a Stirred Tank, *AIChE Journal* **49**, 2700-2714.

[44] Bernard, P. S., Potts, M., and Krispin, J. 2003 Studies of Turbulent Mixing Using the Vorcat Implementation of the 3D Vortex Method, *33rd AIAA Fluid Dynamics Conference and Exhibit*, **2003-3599**.

[45] Bernard, P. S., and Wallace, J. M. 2002 Turbulent Flow Analysis, Measurement, and Prediction, *John Wiley & Sons*, Hoboken, New Jersey.

[46] Panton, R. L. 1996 Incompressible Flow, *John Wiley & Sons*, New York.

[47] Crowe, C. T., Sommerfeld, M., and Tsuji, Y. 1998 Multiphase Flows with Droplets and Particles, CRC Press.

[48] McLaughlin, J. B. 1989 Aerosol Particle Deposition in Numerically Simulated Channel Flow, *Physics of Fluids A* **1**, 1211-1224.

[49] Brandon, D. J., and Aggarwal, S. K. 2001 A Numerical Investigation of Particle Deposition on a Square Cylinder Placed in a Channel Flow, *Aerosol Science and Technology* **34**, 340-352.

[50] Clift, R., Grace, J. R., and Weber, M. E. 1978 Bubbles, Drops, and Particles, *Academic Press*, New York.

[51] Hinds, W. C. 1982 Aerosol Technology: Properties, Behavior, and Measurement of Airborne Particles, *John Wiley & Sons*.

[52] Orlanski, I. 1976 A Simple Boundary Condition for Unbounded Hyperbolic Flows, *Journal of Computational Physics* **21**, 251-269.

[53] FLUENT^{TM} 6.2 User's Guide. 2005 Fluent Inc., Lebanon, New Hampshire.

[54] Ferziger, J. H., and Peric, M. 1999 Computational Methods for Fluid Dynamics, *Springer; 2nd Edition*.

[55] Kontomaris, K., Hanratty, T. J., and McLaughlin, J. B. 1992 An Algorithm for Tracking Fluid Particles in a Spectral Simulation of Turbulent Channel Flow, *Journal of Computational Physics* **103**, 231-242.

[56] Shepard, D. 1968 A Two-dimensional Interpolation Function for Irregularly Spaced Data, *Proceedings of the 23rd ACM National Conference*, 517-524.

[57] Kincaid, D., and Cheney, W. 1991 Numerical Analysis: Mathematics of Scientific Computing, Brooks/Cole Publishing Company, Pacific Grove, California.

[58] Rajaratnam, N. 1976 Turbulent Jets, *Elsevier Scientific Pub. Co.*, Amsterdam.

[59] Haglund, J. S. 2003 Two Linear Slot Nozzle Virtual Impactors For Concentration of Bioaerosols, *PhD Dissertation, Department of Mechanical Engineering, Texas A&M University.*

[60] Drazin, P. G. 2002 Introduction to Hydrodynamic Stability, *Cambridge University Press*, Cambridge, United Kingdom.

[61] Bendat, J. S., and Piersol, A. G. 1980 Engineering Applications of Correlation and Spectral Analysis, *John Wiley & Sons.*

[62] Wallace J. M., Eckelmann, H., and Brodkey R. S. 1972 The Wall Region in Turbulent Shear Flow, *Journal of Fluid Mechanics* **54**, 39-48.

[63] Sagaut, P. 2001 Large Eddy Simulation for Incompressible Flows: An Introduction, *Spriger-Verlag*, Berlin.

[64] Piomelli, U., Yunfang, Y., and Adrian, R. J. 1996 Subgrid-Scale Energy Transfer and Near-Wall Turbulence Structure, *Physics of Fluids* **8**, 215-224.

[65] Smagorinski, J. 1963 General Circulation Experiments With The Primitive Equations. I. The Basic Experiment, *Monthly Weather Review* **91**, 99-164.

[66] Pope, S. B. 2000 Turbulent Flows, *Cambridge University Press*, Cambridge, United Kingdom.

[67] Germano, M., Piomelli, U., Moin, P., and Cabot, W. H. 1991 A Dynamic Subgrid-Scale Eddy Viscosity Model, *Physics of Fluids A* **3**, 1760-1765.

[68] Lilly, D. K. 1992 A Proposed Modification of The Germano Subgrid-Scale Closure Method, *Physics of Fluids A* **4**, 633-635.

[69] Piomelli, U. 1993 High Reynolds Number Calculations Using The Dynamic Subgrid-Scale Stress Model, *Physics of Fluids A* **5**, 1484-1490.

[70] Kaltenbach, H. J., and Choi, H. 1995 Large-Eddy Simulation of Flow Around an Airfoil on a Structured Mesh, *Annual Research Briefs*, 51, Center for Turbulence Research, Stanford University.

[71] Meneveau, C., Lund, T. S., and Cabot, W. H. 1996 A Lagrangian Dynamic Subgrid-Scale Model of Turbulence, *Journal of Fluid Mechanics* **319**, 353-385.

[72] Kim, J., Moin, P., and Moser, R. 1987 Turbulence Statistics in Fully Developed Channel Flow at Low Reynolds Number, *Journal of Fluid Mechanics* **177**, 133-166.

[73] Moser, R. D., Kim, J., and Mansour, N. N. 1999 Direct Numerical Simulation of Turbulent Channel Flow up to $Re_\tau = 590$, *Physics of Fluids* **11**, 943-945.

[74] Radhakrishnan, Senthil. Graduate Student, Department of Mechanical Engineering, University of Maryland, *Personal Communication.*

[75] Rodi, W., Ferziger, J., Breuer, M., and Pourquie, M. 1997 Status of Large-Eddy Simulations: Results of a Workshop, *Journal of Fluids Engineering* **119**, 248-262.

[76] Sohankar, A., Davidson, L., and Norberg, C. 2000 Large Eddy Simulation of Flow Past a Square Cylinder: Comparison of Different Subgrid Scale Models, *Journal of Fluids Engineering* **122**, 39-47.

[77] Lyn, D. A., and Rodi, W. 1994 The Flapping Shear Layer Formed by Flow Separation From The Forward Corner of a Square Cylinder, *Journal of Fluid Mechanics* **267**, 353-376.

[78] Lyn, D. A., Einav, S., Rodi, W., and Park, J.-H. 1995 A Laser-Doppler Velocimetry Study of Ensemble-Averaged Characteristics of The Turbulent Near Wake of a Square Cylinder, *Journal of Fluid Mechanics* **304**, 285-319.

[79] Piomelli, U., Zang, T. H., Speziale, C. G., and Hussaini, M. Y. 1990 On the Large-Eddy Simulation of Transitional Wall-Bounded Flows, *Physics of Fluids A* **2**, 257-265.

[80] Dubief, Y., and Delcayre, F. 2000 On Coherent-Vortex Identification in Turbulence, *Journal of Turbulence* **1**.

[81] Dr. Arun Ranade, *personal communication.*

[82] Model 3321 Aerodynamic Particle Sizer Spectrometer, *Instruction Manual*, P/N 1930092, Revision E, January 2004, **TSI**.

[83] Vinkovic, I., Aguirre, C., Simoens, S., and Gorokhovski, M. 2006 Large Eddy Simulation of Droplet Dispersion for Inhomogeneous Turbulent Wall Flow, *International Journal of Multiphase Flow* **32**, 344-364.

[84] Pope, S. B. 2004 Ten Questions Concerning the Large Eddy Simulation of Turbulent Flows, *New Journal of Physics* **6**.

[85] Ol'shanskii, M. A., and Staroverov, V. M. 2000 On Simulation of Outflow Boundary Conditions in Finite Difference Calculations for Incompressible Fluid, *Int. J. Numer. Meth. Fluids* **33**, 499-534.

[86] Balaras, E. 2004 Modeling Complex Boundaries Using an External Force Field on Fixed Cartesian Grids in Large-Eddy Simulations, *Computers & Fluids* **33**, 375-404.

[87] Braza, M., Chassaing, P., and Ha Minh, M. 1986 Numerical Study and Physical Analysis of The Pressure and Velocity Fields in the Near Wake of a Circular Cylinder, *Journal of Fluid Mechanics* **165**, 79-130.